

Systematic development of force fields to describe gas adsorption in nanoporous materials

Quinten Mortier

Supervisors: Prof. dr. ir. Toon Verstraelen, Prof. dr. ir. Veronique Van Speybroeck
Counsellors: Ir. Steven Vandenbrande, Ir. Louis Vanduyfhuys

Master's dissertation submitted in order to obtain the academic degree of
Master of Science in Engineering Physics

Vakgroep Fysica en Sterrenkunde
Chair: Prof. dr. Dirk Ryckbosch

Department of Applied Physics
Chair: Prof. dr. ir. Christophe Leys

Faculty of Engineering and Architecture
Academic year 2016-2017





Center for
Molecular Modeling

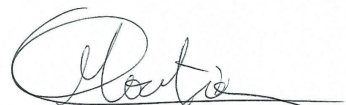
This work has been performed at the Center for Molecular Modeling.

Preface

Copyright Agreement

The author gives permission to make this master dissertation available for consultation and to copy parts of this master dissertation for personal use.

In the case of any other use, the copyright terms have to be respected, in particular with regard to the obligation to state expressly the source when quoting results from this master dissertation.



Quinten Mortier
June 1, 2017

Systematic development of force fields to describe gas adsorption in nanoporous materials

by Quinten MORTIER

Supervisors: Prof. dr. ir. Toon VERSTRAELEN, Prof. dr. ir. Veronique VAN SPEYBROECK
Counsellors: ir. Steven VANDENBRANDE, ir. Louis VANDUYFHUYS

Master's dissertation submitted in order to obtain the academic degree of
Master of Science in Engineering Physics

Vakgroep Fysica en Sterrenkunde

Chair: Prof. dr. Dirk Ryckbosch

Department of Applied Physics

Chair: Prof. dr. ir. Christophe Leys

Faculty of Engineering and Architecture

Academic year 2016-2017

Abstract

In this work, a force field methodology is devised to describe gas adsorption in nanoporous materials, solely based on *ab initio* data. For this purpose, the Monomer Electron Density Force Field (MEDFF) is first applied to N₂ and CO₂ fluids. Subsequently, the model is extended to describe the adsorption of these gases in MIL-53(Al) and ZIF-8. Comparing simulated adsorption isotherms to generic force fields and the experiment, the proposed methodology is validated. It was found that even though the MEDFF is capable to reproduce interaction energies accurately, modeling adsorption on a *ab initio* basis is extremely challenging.

Keywords

Nanoporous materials, metal-organic frameworks, force fields, adsorption

Systematic development of force fields to describe gas adsorption in nanoporous materials

Quinten Mortier

Supervisor(s): Toon Verstraelen, Veronique Van Speybroeck
Counsellor(s): Steven Vandenbrande, Louis Vanduyfhuys

Abstract—In this work, a force field methodology is devised to describe gas adsorption in nanoporous materials, solely based on *ab initio* data. For this purpose, the Monomer Electron Density Force Field (MEDFF) is first applied to N₂ and CO₂ fluids. Subsequently, the model is extended to describe the adsorption of these gases in MIL-53(Al) and ZIF-8. Comparing simulated adsorption isotherms to generic force fields and the experiment, the proposed methodology is validated. It was found that even though the MEDFF is capable to reproduce interaction energies accurately, modeling adsorption on a *ab initio* basis is extremely challenging.

Keywords—nanoporous materials, metal-organic frameworks, force fields, adsorption

I. INTRODUCTION

Metal-organic frameworks (MOFs) form a relatively new class of nanoporous materials that recently gained more attention due to their remarkable gas adsorption properties. The ability to efficiently store gases can serve many purposes in modern-day society with relevant applications being carbon capture and sequestration as well as hydrogen storage. Gas adsorption has therefore been studied on an experimental basis for a large number of metal-organic frameworks. [1][2] However, the broad variety in both molecular building blocks and methods to combine them, allows an almost unlimited number of MOFs to be synthesized. Experimental characterization of all these materials is hence an extremely time-consuming task. Computational simulations provide an alternative to screen relevant materials more efficiently. [3][4][5] To simulate adsorption in a nanoporous host however, a highly accurate physical model is required. While fully-quantum-mechanical methods feature this level of accuracy, their computational cost is too high. Therefore cheaper, though less accurate, models like force fields should be applied.

Force fields are analytical approximations of the quantum-mechanical potential energy surface. They typically consist of a covalent part, describing interactions related to chemical bonds, and a non-covalent part for long-range interactions. In adsorption simulations, frameworks and adsorbate molecules are often kept rigid, as adsorption is in the first place dominated by host-guest interactions between the framework and adsorbate molecules and mutual guest-guest interactions between the adsorbates. Covalent interactions, causing framework flexibility are therefore neglected. Also in this work, only non-covalent interactions will be considered. This approximation is especially far-reaching for flexible

frameworks like MIL-53(Al) where the gas uptake is strongly influenced by phase transitions, also known as breathing behavior. However, modeling these effects is beyond the scope of this work.

While many force fields, encompassing non-covalent terms, have already been proposed in literature, only recently models, specifically intended for adsorption simulations, have been developed. Refitting generic force field parameters for instance, Calero et al. [6] found force fields that accurately reproduce experimental adsorption isotherms. However, these methods are based on experimental data and since this work aims to provide a methodology that is also applicable to hypothetical materials, an *ab initio* derivation of force field parameters is preferred. Therefore, the Monomer Electron Density Force Field [7] (MEDFF) is used. This is a pairwise-additive, non-covalent force field, parametrized by *ab initio* data only. It features physically inspired contributions for electrostatics, exchange-repulsion, induction and dispersion, based on the Symmetry-Adapted Perturbation Theory [8] (SAPT) decomposition of interaction energies.

In this work, the MEDFF, originally developed for dispersion-dominated interactions, will be extended to fluids like N₂ and CO₂ where dispersion is less dominant. Subsequently, the force field will be applied to describe the adsorption of N₂ and CO₂ in MIL-53(Al) and ZIF-8. For this purpose, specific parameter sets are derived for the host-guest interactions in section IV via adsorption energies and a cluster model approach. The derived force fields will eventually be applied in adsorption simulations, assessing the validity of the proposed methodology.

II. MONOMER ELECTRON DENSITY FORCE FIELD

A. Methodology and Force Field Expression

The Monomer Electron Density Force Field approximates non-covalent interaction energies by the following analytical expression:

$$\begin{aligned} E_{MEDFF} &= \sum_{\text{dimers}} E_{int} \\ &= \sum_{\text{dimers}} E_{elst} + E_{exch-rep} + E_{ind} + E_{disp} \end{aligned} \quad (1)$$

The summation runs over all dimers consisting of interacting molecules, thus expressing that the MEDFF is pairwise-

Q. Mortier is with the Center for Molecular Modeling, Ghent University (UGent), Gent, Belgium. E-mail: Quinten.Mortier@UGent.be .

additive. For each dimer, four energy contributions can be discerned and all these contributions are based on two ingredients. On the one hand an analytical model for the electron density of the interacting monomers is required. On the other hand, three so-called interaction parameters must be determined. For the former, the Minimal Basis Iterative Stockholder [9] (MBIS) charge partitioning scheme is used. Herein, the *ab initio* molecular electron density of a monomer is partitioned into atomic contributions by means of an auxiliary model electron density. A slight simplification of this model electron density approximates the *ab initio* monomer electron density by core charges, located at atomic nuclei and surrounded by Slater-type valence shells. The simplified model density, $\tilde{\rho}^e(\mathbf{r})$, is then used to determine the MEDFF contributions. Indeed, the electrostatic contribution, for instance, is determined by the Coulomb integral between the charge densities of the interacting monomers. These charge densities, $\tilde{\rho}(\mathbf{r})$, are approximated by the model electron densities and the charges on the atomic nuclei. As a result, the electrostatic contribution to the interaction energy is:

$$E_{elst} = \int d\mathbf{r}_1 \int d\mathbf{r}_2 \frac{\tilde{\rho}_1(\mathbf{r}_1)\tilde{\rho}_2(\mathbf{r}_2)}{|\mathbf{r}_1 - \mathbf{r}_2|} \quad (2)$$

In contrast to the other force field contributions, electrostatics contains no interaction parameter and is thus completely determined by the MBIS model electron densities. Exchange-repulsion and induction on the other hand, are both modeled proportional to the overlap between the electron densities of the two interacting monomers. The proportionality constants are the first two interaction parameters, $U_{exch-rep}$ and U_{ind} :

$$\begin{aligned} E_{exch-rep} &= U_{exch-rep} \int d\mathbf{r} \tilde{\rho}_1^e(\mathbf{r}) \tilde{\rho}_2^e(\mathbf{r}) \\ E_{ind} &= U_{ind} \int d\mathbf{r} \tilde{\rho}_1^e(\mathbf{r}) \tilde{\rho}_2^e(\mathbf{r}) \end{aligned} \quad (3)$$

An important remark is that since both exchange-repulsion and induction are proportional to the overlap, only the sum of the corresponding interaction parameters has an influence on force field evaluations. Finally, for dispersion the following expression applies:

$$\begin{aligned} E_{disp} &= \sum_{A=1}^{N_{atoms}} \sum_{B=1}^{N_{atoms}} E_{disp}^{AB} \\ E_{disp}^{AB} &= -f_6(x_{AB}) \frac{C_{AB}^6}{R_{AB}^6} - U_{s8} f_8(x_{AB}) \frac{C_{AB}^8}{R_{AB}^8} \end{aligned} \quad (4)$$

The dispersion contribution thus consists of a superposition of atomic interactions between atom A in monomer 1 and atom B in monomer 2. By inserting the MBIS model electron densities in Eq. (2) and (3), it was found that this also applies for the other force field contributions. Furthermore, f_6 and f_8 are damping functions and C_{AB}^6 and C_{AB}^8 are constants. These are specified in more detail in the work of Vandebrande et al. [7]. U_{s8} is a third interaction parameter.

B. Fitting Procedure

While MBIS parameters for the model densities can be determined straightforwardly once an *ab initio* monomer electron density is provided, the determination of interaction parameters is more involved. Initially, SAPT2+(3)/aug-cc-pVTZ[8][10] and CCSD(T)/CBS [11] interaction energies have

to be calculated for a large set of dimer configurations, generating reference data for dimer interaction energies. For the CBS limit, the settings used in the paper of Hobza et al. were applied. [12] Force field contributions containing an interaction parameter are then separately matched to their corresponding SAPT contribution by means of an ordinary least-squares fit. Since interaction energies in the CCSD(T)/CBS level of theory are more accurate, a restrained fit is subsequently performed, matching the complete force field interaction energies to the CCSD(T) data. In this way, the three interaction parameters are refined simultaneously. For this purpose, the following cost function was used:

$$\begin{aligned} L = \frac{1}{2} \sum_{n=1}^{N_d} \frac{(E_n^{FF}[\mathbf{U}] - E_n^{ref})^2}{N_d} \\ + \frac{1}{2\sigma_{pr}^2} \sum_{\alpha=1}^3 \left(\frac{U_{\alpha} - U_{\alpha}^{SAPT}}{U_{\alpha}^{SAPT}} \right)^2 \end{aligned} \quad (5)$$

The first sum runs over all dimer configurations for which *ab initio* interaction energies were determined and includes the mean squared deviation between these *ab initio* energies, E_n^{ref} , and their corresponding force field predictions, $E_n^{FF}[\mathbf{U}]$. U_{α}^{SAPT} , on the other hand, are the interaction parameters resulting from the fit to SAPT data. The second term thus suppresses changes in interaction parameters. In this way, the physical validity of the separate force field contributions, instigated by the SAPT fit, is safeguarded. The σ_{pr} parameter determines how strong the restraint is.

III. GUEST-GUEST INTERACTIONS

A. Force Field Construction

For the dispersion-dominated complexes the MEDFF was found to reproduce *ab initio* interaction energies accurately with system-independent interaction parameters. [7] We now show that the method can also be applied successfully to other fluids if case-specific interaction parameters are fitted via Eq. (5). In this work, this was done for N₂ and CO₂. First, MBIS parameters were determined based on B3LYP/aug-cc-pVTZ [13][14] and CCSD(aug-cc-pVTZ molecular electron densities. Subsequently, interaction parameters were derived by the fitting procedure. To determine an optimal value for σ_{pr} , the root-mean-squared deviation w.r.t. to CCSD(T) energies, RMSD_{CCSD(T)}, as well as the relative RMSD of the interaction parameters w.r.t. their SAPT values, RMSD_U, are determined as a function of σ_{pr} . These curves have a typical profile, displayed for N₂ in Figure 1. However, the σ_{pr} value where RMSD_{CCSD(T)} starts to decrease and RMSD_U starts to increase, was found to be system-dependent. Therefore, the deviation percentage (DP) is introduced, expressing by means of a percentage how much the RMSD of the interaction energies differs from the CCSD(T) limit. The definition of this concept is also illustrated in Figure 1. One notices that DP=0% yields a pure CCSD(T) fit while for DP=100% a pure SAPT fit is obtained. Figure 1 also shows that a significant reduction in RMSD_{CCSD(T)} is obtained by the fit to CCSD(T) reference data, thus making the force field more accurate. However, in doing this, interaction parameters can differ more than 40% from their SAPT limit values, jeopardizing their physical validity. Similar results were found for CO₂. Ideal values for σ_{pr} and the DP are therefore located in between both limits. As a rule of thumb,

RMSD_U was chosen to be maximally 15%. A deviation percentage of 20% was hence considered optimal for both N_2 and CO_2 . For the corresponding parameter sets, the validity of the force fields was checked by comparing *ab initio* dimer interaction energies and their corresponding force field approximations. While for N_2 the different SAPT energy contributions as well as the CCSD(T) energies are reproduced relatively well, this is not the case for CO_2 . Especially the electrostatics contribution is modeled inaccurately.

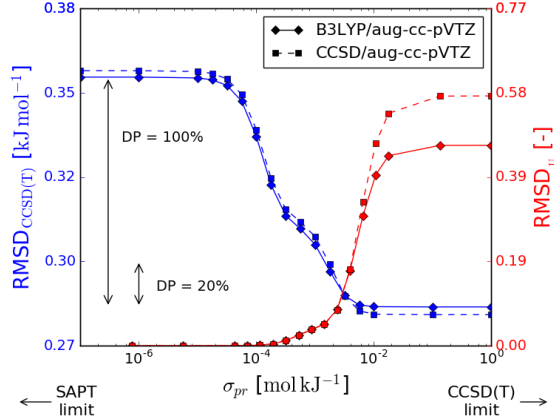


Figure 1: The influence of the σ_{pr} parameter on $\text{RMSD}_{\text{CCSD}(\text{T})}$ and RMSD_U for the MEDFF of N_2 . The definition of the deviation percentage concept is also illustrated.

B. Charge Correction

The electrostatic contribution to the MEDFF contains no interaction parameter and is thus solely determined by the MBIS model densities. An inaccurate reproduction of SAPT electrostatic interaction energies is hence caused by the fact that the model for the monomer electron densities is insufficiently accurate. Especially the inability to fully capture the penetration effect as well as the inability to reproduce molecular multipoles, results in deviations. Indeed, the delocalized valence shells incorporate the penetration effect to some extent but cannot reproduce it entirely. On the other hand, the electrostatic interaction energy between two charge distribution is determined to a large extent by the multipole moments of these charge distributions. To correctly model the electrostatic interaction, a good reproduction of the multipole moments of the monomer electron densities is hence indispensable.

In this work, a method was devised to reproduce the most important (lowest order) multipole moments more accurately. To do this, *ab initio* calculated molecular multipoles of CO_2 were compared to those predicted by the model electron densities. The MBIS scheme always reproduces the molecular charge by construction. For higher-order multipoles however, this is not the case. Indeed, while the molecular charge and dipole were reproduced by the model electron density, the molecular quadrupole moment was not. To solve this, Hadad et al. [15] proposed to correct atomic charges by fitting the multipole moments to their *ab initio* counterparts. However, this approach determines local quantities, the atomic charges, by fitting global quantities, molecular multipoles, typically leading to sloppy fits when an increased number atoms is involved. Therefore, a local variant of the multipole correction method was developed. By means of the MBIS scheme, monomer electron densities were decomposed in atomic contributions. Subsequently, multipoles were calculated for

each of these atomic electron densities, yielding atomic multipoles. Next, all atoms are considered separately and for each atom, distances between this central atom and all the others are calculated. By means of a cut-off condition, only the nearest atoms are withheld and for these atoms charge corrections are determined by a least-squares fit, matching *ab initio* atomic dipole and quadrupole moments of the central atom to those generated by the considered charges. Repeating this procedure with every atom as central atom and summing all the atomic corrections, results in locally determined charge corrections for all atoms. These include the effects of higher order atomic multipoles implicitly and thus manage to reproduce molecular multipoles better as well.

For CO_2 , it was found that especially atomic dipoles give rise to the difference between the modeled and the *ab initio* molecular quadrupole moments. Indeed, atomic dipoles are not included in the model densities because the atomic contributions are spherically symmetric. Applying the multipole correction scheme to the charges in CO_2 , the reproduction of the electrostatics contribution was improved greatly. Also the overall force field performance improved because other contributions do not have to correct erroneous electrostatics anymore. As a result, a DP of 0% was used for the final MEDFF of CO_2 and as was the case for N_2 , exchange-repulsion and dispersion were modeled the most accurately. It was also found that B3LYP/aug-cc-pVTZ electron densities perform better than CCSD/aug-cc-pVTZ densities.

C. Validation

The MEDFFs for the N_2 and CO_2 fluids were validated externally by comparison with second virial coefficients and vapor-liquid coexistence curves (VLCCs). For the second virial coefficients, a satisfactory reproduction was found using the optimal parameter sets. However, it should be noted that simulated curves are highly susceptible to changes in the interaction parameters. Indeed, Figure 2 shows that the second virial coefficient of CO_2 is reproduced to a good degree by the MEDFF with DP=0% and corrected charges. However, deviations rapidly increase if the DP is altered. Figure 2 also confirms the importance of the charge corrections. Indeed, for uncorrected charges interaction energies are too attractive resulting in an underestimation of the second virial coefficient (*i.e.* B_2 is modeled more negative than predicted by the experiment). For the reference interaction parameters derived by Vandenbrande et al. [7] on the other hand, interactions are too repulsive.

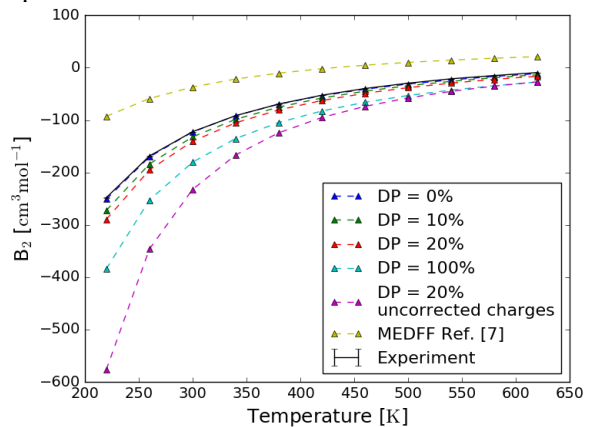


Figure 2: Simulations for the second virial coefficients of CO_2 (using MEDFFs with various parameter sets) are compared to the experiment. [16]

While the reproduction of second virial coefficients is satisfactory for both N_2 and CO_2 , VLCCs are only reproduced to a good degree for N_2 . Figure 3 shows that for CO_2 , the density of the liquid phase is overestimated, indicating that force field interactions in the CO_2 fluid are too attractive. However, as this was not observed for the second virial coefficient, this originates from many-body effects, neglected by the pairwise-additive force field model. E.g. three-body dispersion terms are typically repulsive. Neglecting them thus makes the force field too attractive.

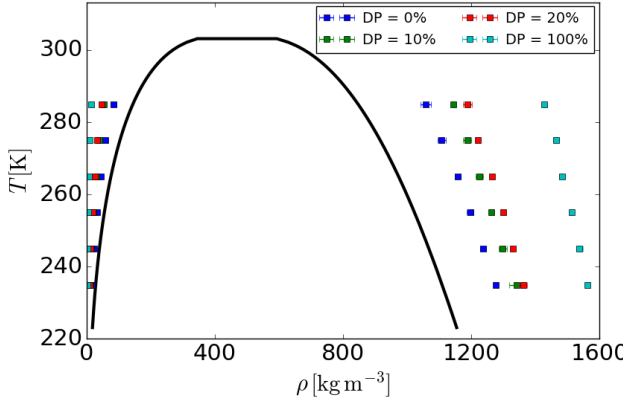


Figure 3: Simulations for the vapor-liquid coexistence curve CO_2 (using MEDFFs with various parameter sets) are compared to the experiment [17] (black curve).

While the MEDFF cannot reproduce VLCCs systematically, other force fields were found in literature that can succeed in this goal. Indeed, in the TraPPE force field [18] for instance, Lennard-Jones potentials are parametrized to reproduce VLCCs. As a result, these force fields are built by effective pair potentials, incorporating many-body effects implicitly, rather than by true pair potentials like in the MEDFF. However, these force fields typically fail to reproduce second virial coefficients accurately. [18] Indeed, second virial coefficients depend on dimer interaction energies and are therefore reproduced better by true pair potentials than by effective pair potentials. Constructing a pairwise-additive force field model that systematically reproduces both second virial coefficients (and thus dimer interaction energies) and VLCCs (and thus many-body effects), is therefore a Sisyphean task.

IV. HOST-GUEST INTERACTIONS

A. Cluster Model

By fitting case-specific interaction parameters, MEDFFs could immediately be derived for the adsorbate gases N_2 and CO_2 , providing a model for the guest-guest interactions during adsorption in a nanoporous host. For the host-guest interactions on the other hand, the method cannot be applied immediately because SAPT and CCSD(T) interaction energies cannot be determined for combinations of adsorbate molecules and their surrounding frameworks. Indeed, while the force field expression and the MBIS scheme can easily be extended to periodic structures, there is no periodic implementation of SAPT and CCSD(T) algorithms. Also, the incredible computational cost such codes would demand, precludes application of these methods. Therefore, smaller parts of the framework, particularly important for the interaction with adsorbates, are considered. Host-guest interaction parameters are then determined by applying the typical MEDFF fitting

procedure (Eq. (5)) to dimers consisting of these so-called clusters and adsorbate molecules. MBIS parameters on the other hand were determined by partitioning B3LYP/aug-cc-pVTZ electron densities for the guest molecules and PBE-D3BJ [19][20] electron densities for the framework.

In ZIF-8, zinc atoms are screened efficiently due to the tetrahedral surround of methyl-imidazole (IZ) linkers. As a result, adsorbates mainly interact with the methyl-imidazole (IZ) linkers. In MIL-53(Al) on the other hand, it was found that besides the BDC linkers, also the bridging oxides play an important role in the adsorption process [21]. However, metal-oxide linkers are typically too large for SAPT and CCSD(T) dimer calculations and therefore also only linkers were considered for MIL-53(Al). This is a far-reaching, tough necessary, approximation to keep *ab initio* calculations computationally tractable. Both the IZ and BDC linkers were terminated by hydrogen atoms yielding the neutral, closed-shell clusters, displayed in Figure 4.

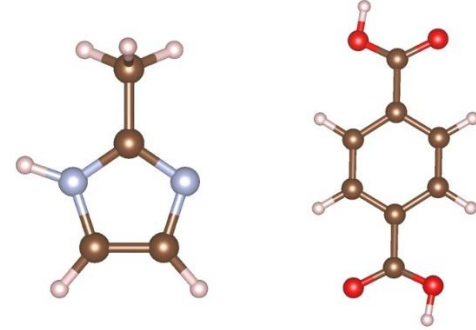


Figure 4: Protonated IZ (left) and BDC (right) linkers used in the cluster model.

A reference data set containing SAPT and CCSD(T) interaction energies was constructed for relevant dimer configurations. Host-guest interaction parameters were subsequently derived by applying Eq. (5). As was the case for N_2 and CO_2 dimers, exchange-repulsion and dispersion are modeled particularly good, while for the electrostatic and induction contribution larger deviations were observed. Therefore, the charge correction scheme was also applied to the linkers. However, the influence of the corrections was rather limited indicating that especially the penetration effect causes deviations.

B. Adsorption Energies

The cluster model approach allows to determine highly accurate interaction energies for the linker-adsorbate dimers. However, effects from other framework constituents (e.g. the bridging OH groups in MIL-53(Al)) as well as the periodic repetition of the considered linkers are not captured by the cluster method. Therefore, adsorption energies in the periodic structure were considered. These are the differences between the energy of a framework with one adsorbate molecule in each unit cell and the energies of the empty framework and the guest molecules separately. Adsorption energies can be determined by *ab initio* dispersion-corrected DFT methods (here the PBE-MBDHI level of theory [15][22][23][24][25] was used). Instead of SAPT and CCSD(T) reference data, these *ab initio* adsorption energies can then be used to fit host-guest interaction parameters. For this fitting procedure, the same cost function as in Eq. (5) was utilized. However, the dimer interaction energies are replaced by adsorption energies and the

reference interaction parameters are now given by the host-guest interaction parameters determined by the cluster model approach. For all framework-guest combinations a significant reduction in the RMSD between *ab initio* and force field adsorption energies was obtained without changing the interaction parameters too much.

V. ADSORPTION ISOTHERMS

In the previous sections, multiple parameter sets were derived for MEDFFs describing both guest-guest and host-guest interactions. By means of Monte Carlo simulations in the grand-canonical ensemble (GCMC simulations), these force fields are used to calculate adsorption isotherms for the adsorption of N₂ and CO₂ in ZIF-8 and MIL-53(Al). Five force field models were applied: four variants of the MEDFF and the generic DREIDING-TraPPE force field [18][26]. The various MEDFF models all use the same set of MBIS parameters and are thus discerned by their interaction parameters:

- MEDFF-RR: In the MEDFF-RR (RR from Reference-Reference) both host-guest and guest-guest interactions utilize the reference interaction parameters, determined for the dispersion-dominated complexes in the S66x8 dataset [5].
- MEDFF-RF: While host-guest interactions are still modeled by the reference interaction parameters, fitted parameters (determined in section III) are used for the guest-guest interaction. Therefore, this model is called MEDFF-RF (RF from Reference-Fit).
- MEDFF-FF: Both host-guest and guest-guest interaction parameters originate from fits to SAPT and CCSD(T) interaction energies in the MEDFF-FF (FF from Fit-Fit) model.
- MEDFF-Refit: Host-guest interaction parameters are refitted by means of DFT-D adsorption energies while guest-guest interaction parameters are still modeled by fitted parameters.

The generic force field on the other hand, models host-guest interactions by means of the DREIDING force field while for guest-guest interactions the TraPPE force field is used. In the DREIDING model, charges need to be attributed to the interacting atoms. The MBIS charges, used for the MEDFFs, were utilized again. In Figure 5, an example of the resulting adsorption isotherms is displayed for the adsorption of CO₂ in ZIF-8 at 298 K.

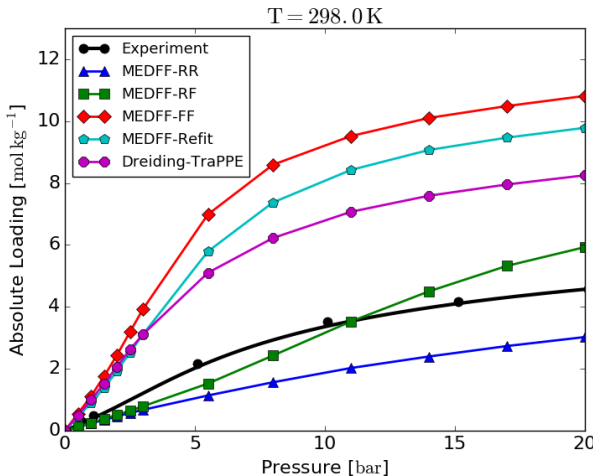


Figure 5: Simulated and experimental [2] adsorption isotherms for the adsorption of CO₂ in ZIF-8 at 298 K.

For all adsorption isotherms, MEDFF-RR and MEDFF-RF predict an equal uptake at lower pressures. Indeed, in this pressure range, adsorption is dominated by host-guest interactions and since these are modeled identically by both force fields the uptake is equal. Another observed trend is that the MEDFF-FF overestimates the adsorption more than other MEDFF models. Systematic reproduction of experimental adsorption isotherms could not be achieved with the MEDFF. Also the generic force field was not able to reproduce experimental data. In an attempt to explain this, adsorption energies predicted by the various models were compared to *ab initio* data. Indeed, if and where molecules are adsorbed at low pressures is determined completely by these energies. For an *ab initio* derived force field to correctly model adsorption, it is thus necessary to accurately reproduce adsorption energies as well.

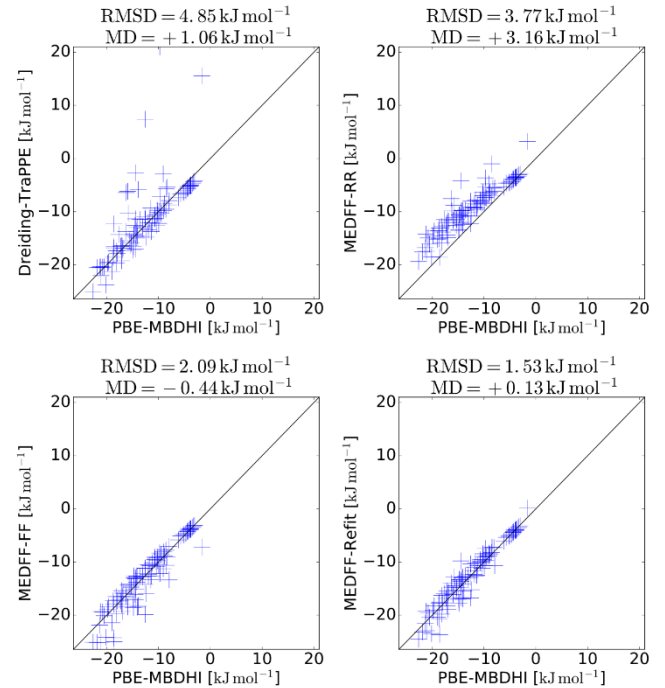


Figure 6: Comparison between the reproduction of *ab initio* adsorption energies by the various force field models for the adsorption of CO₂ in ZIF-8.

In Figure 6 adsorption energies are compared for the adsorption of CO₂ in ZIF-8. The MEDFF-RF model was not included because MEDFF-RR and MEDFF-RF have an identical parameter set for host-guest interactions and thus yield the same adsorption energies. Some trends can be explained immediately based on these adsorption energies. E.g. the underestimation of the uptake of CO₂ in ZIF-8 by MEDFF-RR and MEDFF-RF is due to the fact almost all adsorption energies are modeled too repulsive by these models. MEDFF-FF and MEDFF-Refit on the other hand, reproduce adsorption energies relatively well but adsorption isotherms are overestimated greatly. Satisfactory reproduction of adsorption energies (in terms of a low RMSD) is thus no guarantee for satisfactory reproduction of adsorption isotherms. A first explanation for this is the imperfect nature of the samples used in experimental setups. Surface effects, lattice imperfections and impurities all play an important role, typically reducing the uptake. Also the influence of the most favorable adsorption sites should not be underestimated. Indeed, adsorption sites with the lowest adsorption energy are filled first, thus having the largest influence on the adsorption isotherm, especially at

lower pressures. If the most favorable adsorption sites are overbound, this could hence result in a significant overestimation of the uptake. Force fields should hence be extremely accurate (especially for the most favorable adsorption sites) to reproduce experimental adsorption isotherms. An important remark in this context is that even the *ab initio* adsorption energies may not be accurate enough. Indeed, while DFT methods are applicable to large systems, an important sacrifice lies in the relative lack of accuracy when compared to e.g. Coupled-Cluster methods. Significant differences are also observed between the various dispersion correction schemes found in the literature. Reaching the required level of accuracy by a force field is hence extremely challenging.

VI. CONCLUSIONS

In this work, the MEDFF methodology was successfully applied to fluids where interactions are not dominated by dispersion. While the model was able to reproduce dimer interaction energies, the lack of many-body interactions was found to be problematic. In a way, *ab initio* force fields like the MEDFF can therefore be considered as complementary to effective pair potentials. The force field was also extended to describe gas adsorption in nanoporous materials. Via cluster models and adsorption energies, the model was tuned to be more representative in these applications. However, systematic reproduction of experimental adsorption isotherms was not achieved. It was found though, that the level of accuracy, required to reach this goal, is almost unattainable by force fields. This also puts previously performed reparameterizations of force fields in perspective. Indeed, while adapted parameter sets may be capable to reproduce experimental adsorption isotherms exactly, these are rather lucky shots than models that accurately capture the details of adsorption process.

ACKNOWLEDGEMENTS

This work was performed at the Center for Molecular Modeling (CMM), under supervision of ir. Steven Vandenbrande, dr. ir. Louis Vanduyfhuys, prof. dr. ir. Toon Verstraelen and prof. dr. ir. Veronique Van Speybroeck. I would like to thank them for their support and guidance throughout the realization of this thesis. Computational resources and services were provided by Ghent University (Stevin Supercomputer Infrastructure).

REFERENCES

- [1] P. Mishra, H. P. Uppara, B. Mandal, and S. Gumma, *Adsorption and Separation of Carbon Dioxide using MIL-53(Al) Metal-Organic Framework*, Industrial & Engineering Chemistry Research, 53(51):19747-19753, 2014.
- [2] Z. Zhang, S. Xian, Q. Xia, H. Wang, Z. Li, and J. Li., *Enhancement of CO₂ Adsorption and CO₂/N₂ Selectivity on ZIF-8 via Postsynthetic Modification*, American Institute of Chemical Engineers Journal, 59(6):2195-2206, 2013.
- [3] C. E. Wilmer, M. Leaf, C. Y. Lee, O. K. Farha, B. G. Hauser, J. T. Hupp, and R. Q. Snurr, *Large-scale screening of hypothetical metal-organic frameworks*, Nature Chemistry, 4:83-89, 2012.
- [4] A. N. Dickey, A. O. Yazaydin, R. R. Willis, and R. Q. Snurr, *Screening CO₂/N₂ Selectivity in Metal-Organic Frameworks using Monte Carlo Simulations and Ideal Adsorbed Solution Theory*, The Canadian Journal of Chemical Engineering, 90(4):825-832, 2012.
- [5] Y. G. Chung, J. Camp, M. Haranczyk, B. J. Sikora, W. Bury, V. Krungleviciute, T. Yildirim, O. K. Farha, D. S. Sholl, and R. Q. Snurr, *Computation-Ready, Experimental Metal-Organic Frameworks: A Tool to Enable High-Throughput Screening of Nanoporous Crystals*, Chemistry of Materials, 26(21):6185-6192, 2014.
- [6] A. Garcia-Sanchez, C. O. Ania, J. B. Parra, D. Dubbeldam, T. J. H. Vlugt, R. Krishna, and S. Calero, *Transferable Force Field for Carbon Dioxide Adsorption in Zeolites*. The Journal of Physical Chemistry C, 113(20):8814-8820, 2009.
- [7] S. Vandenbrande, M. Waroquier, V. Van Speybroeck, and T. Verstraelen, *The Monomer Electron Density Force Field (MEDFF): A Physically Inspired Model for Non-Covalent Interactions*, Journal of Chemical Theory and Computation (JCTC), 13(1):161-179, 2017.
- [8] B. Jeziorski, R. Moszynski, and K. Szalewicz, *Perturbation Theory Approach to Intermolecular Potential Energy Surfaces of van der Waals Complexes*, Chemical Reviews, 94(7):1887-1930, 1994.
- [9] T. Verstraelen, S. Vandenbrande, F. Heidar-Zadeh, L. Vanduyfhuys, V. Van Speybroeck, M. Waroquier, and P. W. Ayers, *Minimal Basis Iterative Stockholder: Atoms in Molecules for Force-Field Development*, Journal of Chemical Theory and Computation, 12:3894-3912, 2016.
- [10] R. A. Kendall, T. H. Dunning, and R. J. Harrison, *Electron affinities of the first-row atoms revisited. Systematic basis sets and wave functions*, J. Chem. Phys., 96:6796-6806, 1992.
- [11] J. Čížek, *On the Correlation Problem in Atomic and Molecular Systems. Calculation of Wavefunction Components in Ursell-Type Expansion Using Quantum-Field Theoretical Methods*, The Journal of Chemical Physics 45:4256, 1966.
- [12] J. Řezáč, K. E. Riley, and Pavel Hobza, *S66: A Well-balanced Database of Benchmark Interaction Energies Relevant to Biomolecular Structures*, J. Chem. Theory Comput., 7(8):2427-2438, 2011.
- [13] A. D. Becke, *Density-functional thermochemistry. III. The role of exact exchange*, J. Chem. Phys., 98:5648-5652, 1993.
- [14] C. Lee, W. Yang, and R. G. Parr, *Development of the Colle-Salvetti correlation-energy formula into a functional of the electron density*, Phys. Rev. B, 37:785, 1988.
- [15] R. Hadad and R. Baer, *Minimally-corrected Partial Atomic Charges for Non-Covalent Electrostatic Interactions*, Molecular Physics, December 2016.
- [16] H. Eslami, F. Mozaari, and A. Boushehri, *Calculation of the Second Virial Coefficient of Nonspherical Molecules: Revisited*, International Journal of Thermal Sciences, 40(11):999-1010, 2001.
- [17] R. Span and W. Wagner, *A New Equation of State for Carbon Dioxide Covering the Fluid Region from the Triple-Point Temperature to 1100 K at Pressures up to 800 MPa*, Journal of Physical and Chemical Reference Data, 25(6):1509-1596, 1996.
- [18] M. G. Martin and J. I. Siepmann, *Transferable Potentials for Phase Equilibria. I. United-Atom Description of n-Alkanes*, The Journal of Physical Chemistry B, 102(14):2569-2577, 1998.
- [19] J. P. Perdew, K. Burke, and M. Ernzerhof, *Generalized Gradient Approximation Made Simple*, Phys. Rev. Lett., 77:3865-3868, 1996.
- [20] S. Grimme, S. Ehrlich, and L. Goerigk, *Effect of the damping function in dispersion corrected density functional theory*, J. Comput. Chem., 32(7):1456-1465, 2011.
- [21] M. Mihaylov, K. Chakarova, S. Andonova, N. Drenchev, E. Ivanova, A. Sabetghadam, B. Seoane, J. Gascon, F. Kapteijn, and K. Hadjiivanov, *Adsorption Forms of CO₂ on MIL-53(Al) and NH₂-MIL-53(Al) As Revealed by FTIR Spectroscopy*, J. Phys. Chem. C, 120 (41):23584-23595, 2016.
- [22] A. Tkatchenko, R. A. DiStasio, R. Car, and M. Scheffler, *Accurate and Efficient Method for Many-Body van der Waals Interactions*, Phys. Rev. Lett., 108(23):236402-236406, 2012.
- [23] A. Ambrosetti, A. M. Reilly, R. A. DiStasio, and A. Tkatchenko, *Long-Range Correlation Energy Calculated from Coupled Atomic Response Functions*, The Journal of Chemical Physics, 140(18):18A508, 2014.
- [24] R. A. DiStasio, V. V. Gobre, and A. Tkatchenko, *Many-Body van der Waals Interactions in Molecules and Condensed Matter*, Journal of Physics: Condensed Matter, 26(21):213202, 2014.
- [25] P. Bultinck, C. Van Alsenoy, P. W. Ayers, and R. Carbo-Dorca, *Critical Analysis and Extension of the Hirshfeld Atoms in Molecules*, The Journal of Chemical Physics, 126(14):144111, 2007.
- [26] S. L. Mayo, B. D. Olafson, and W. A. Goddard, *DREIDING: a Generic Force Field for Molecular Simulations*, The Journal of Physical Chemistry, 94(26):8897-8909, 1990.

Table of Contents

Preface	iii
Copyright Agreement	iv
Overview	v
Extended Abstract	vi
Table of Contents	xii
List of Abbreviations	xiv
1 Introduction	1
1.1 Nanoporous Materials	1
1.2 Force Fields	2
1.3 Adsorption in MIL-53(Al) and ZIF-8	5
1.3.1 MIL-53(Al)	5
1.3.2 ZIF-8	6
1.4 Outline and Goal of this Thesis	7
2 The Monomer Electron Density Force Field	8
2.1 Methodology	8
2.1.1 Minimal Basis Iterative Stockholder	9
2.1.2 Force Field Contributions	10
2.1.3 Interaction Parameters	12
3 Guest-Guest Interactions	14
3.1 N ₂	14
3.1.1 Force Field Construction	14
3.1.2 Validation	18
3.2 CO ₂	23
3.2.1 Force Field Construction	23
3.2.2 Charge Rescaling	26
3.2.3 Validation	33
3.2.3.1 Internal Validation	33
3.2.3.2 External Validation	36

4 Host-Guest Interactions	39
4.1 ZIF-8	39
4.1.1 Cluster Model	39
4.1.2 Monomer Electron Density Force Field for IZ-N ₂	42
4.1.3 Monomer Electron Density Force Field for IZ-CO ₂	44
4.1.4 Adsorption Energies	45
4.2 MIL-53(Al)	49
4.2.1 Cluster Model	49
4.2.2 Monomer Electron Density Force Field for BDC-N ₂	51
4.2.3 Monomer Electron Density Force Field for BDC-CO ₂	52
4.2.4 Adsorption Energies	53
5 Adsorption Isotherms	59
5.1 ZIF-8	60
5.1.1 N ₂	60
5.1.2 CO ₂	64
5.2 MIL-53(Al)	67
5.2.1 N ₂	68
5.2.2 CO ₂	71
6 Conclusion and Outlook	78
A MBIS Parameters for IZ and BDC Clusters	82
B MEDFF Performance for Clusters	84
C Supplementary Adsorption Isotherms	89
Bibliography	93

List of Abbreviations

MOF	Metal-Organic Framework
COF	Covalent Organic Framework
BDC	Benzene dicarboxylic Acid
ZIF	Zeolitic Imidazolate Framework
MIL	Materials of Institute Lavoisier
DFT	Density Functional Theory
DoF	Degrees of Freedom
MD	Molecular Dynamics
MC	Monte Carlo
PES	Potential Energy Surface
UFF	Universal Force Field
GROMOS	Groningen Molecular Simulation
OPLS	Optimized Potentials for Liquid Simulations
AMBER	Assisted Model Building with Energy Refinement
TraPPE	Transferable Potentials for Phase Equilibria
MM3	Molecular Mechanics 3
SIBFA	Sum of Interactions Between Fragments Ab initio computed
EFP	Effective Fragment Potential
SAPT	Symmetry Adapted Perturbation Theory
QMDF	Quantum-Mechanically Derived Force Field
lp	large pore
np	narrow pore
MEDFF	Monomer Electron Density Force Field
MBIS	Minimal Basis Iterative Stockholder
CCSD(T)	Coupled-Cluster with Single, Double and perturbative Triple excitations
B3LYP	Becke-3 and Lee-Yang-Parr density functional
LoT	Level of Theory
DM	(Hobza) Distance Multiplier
VLCC	Vapour Liquid Coexistence Curve
RMSD	Root Mean Squared Deviation
DP	Deviation Percentage

Chapter 1

Introduction

The second industrial revolution marked the beginning of an era where fossil fuels became human's primary energy supply due to its versatile use in applications. In recent years, however, it was established that the resulting emission of gases like CO₂ damages the environment dangerously with global warming as a striking example of technology's disruptive impact on planet Earth. In order to halt these devastating processes, other energy stocks should be tapped. Even though this transition to renewable energy sources has started, fossil fuels remain an important energy source to this day. Preventing the associated harmful substances to enter the atmosphere while simultaneously researching innovative ways to replace fossil fuels, therefore are currently two of the most challenging objectives for our society. Modern day applications in this domain include *i.a.* research regarding hydrogen powered cars, carbon sequestration etc. In this master's dissertation an important category of candidate materials for these purposes, the nanoporous materials, are studied, focussing on their possible application in the described fields.

1.1 Nanoporous Materials

Nanoporous materials are solid, typically powder-like, substances consisting of a periodic atomic framework just like a conventional crystalline solid. However, in nanoporous materials, the atoms form a skeletal structure containing substantial voids, called pores. The dimensions of these pores generally range from 1 to 100 nm, thus explaining the term nanoporous. Classification of nanoporous materials typically proceeds via two characteristics: pore size and chemical composition. Depending on the pore size, one distinguishes micropores with pore sizes up to 2 nm, mesopores ranging from 2 to 50 nm and macropores for pores with typical dimensions above 50 nm. Concerning chemical composition, one encounters important groups like zeolites, Metal-Organic Frameworks (MOFs) and Covalent Organic Frameworks (COFs). Zeolites^{1,2} (from the Greek $\zeta\epsilon\omega$ (zeo, to boil) and $\lambda\iota\thetao\varsigma$ (lithos, stone)) are inorganic, aluminosilicate minerals while Metal-Organic Frameworks^{3,4} consist of inorganic, metal-oxide nodes connected by organic ligands, called linkers (e.g. benzenedicarboxylic acid (BDC)). The plurality of these building blocks allows a wide variety of MOFs to be synthesized. The same applies to COFs^{5,6} where all building blocks are organic and strong covalent bonds give rise to rigid frameworks with exceptional properties (low densities and high surface areas⁷). An important subgroup of the MOFs are the Zeolitic Imidazolate Frameworks (ZIF),⁸ where tetrahedral Si(Al) and the bridging oxygen

are replaced by transition metal ions and imidazolate linkers. Due to the pores present in all of these material classes, certain guest molecules will be adsorbed while other substances cannot enter the framework.^{9–14} In this work mainly the adsorption of CO₂ and N₂ in the MOFs ZIF-8⁸ and MIL-53(Al)¹⁵ (Figure 1.1) will be investigated.

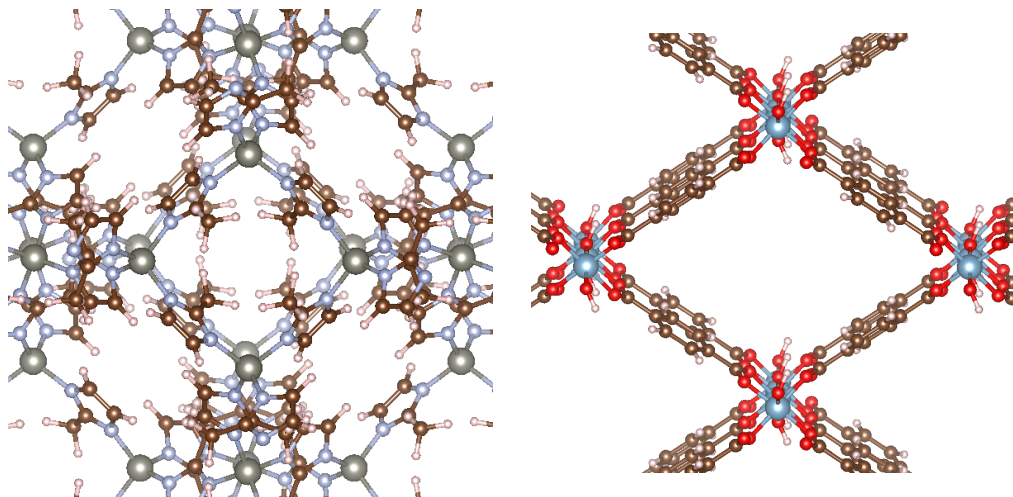


Figure 1.1: Molecular structure of the nanoporous materials ZIF-8 (left) and MIL-53(Al) (right).

1.2 Force Fields

The large amount of molecular building blocks available for the construction of nanoporous materials allows an almost unlimited number of combinations to be synthesized. Since experimental testing of all these materials is extremely time-consuming, computational simulations can be a valuable tool in the discovery of suited candidates for particular applications.^{16–18} However, reliable predictions demand a highly accurate description of the materials under consideration. Unfortunately the most precise quantum-mechanical methods, like Coupled-Cluster, also are computationally the most expensive, restricting their use to small systems with a limited number of atoms. Typical unit cells of nanoporous materials, on the other hand, can contain more than hundred atoms. One should thus revert to more manageable methods like Density Functional Theory (DFT). While this technique is able to handle the large amount of degrees of freedom (DoF), its use in molecular simulations is limited. Indeed, in these simulations one or more DFT calculations have to be performed each iteration. Since adsorption simulations typically require millions of iterations, even DFT methods thus become computationally too demanding.

An interesting alternative for fully quantum-mechanical calculations is given by force fields. Herein, the quantum-mechanical details of the system, represented by the electronic degrees of freedom, are replaced by an analytical expression for the classical potential energy, depending only on the nuclear coordinates. This is a significant approximation but the reduction in complexity makes larger systems and longer time scales accessible for simulation techniques like Molecular Dynamics (MD) and Monte Carlo (MC). Force field contributions can be divided in two groups: covalent terms, related to chemical bonds, and non-covalent contributions, describ-

ing long range interactions (e.g. electrostatic interactions). The force field contributions typically contain unknown parameters. Fitting the force field to experimental reference data or *ab initio* calculations allows the determination of these parameters. Both the force field expression and the fitting procedure thus determine the performance of the force field. Many criteria are used to evaluate this performance. In this work the reproduction of the quantum-mechanical potential energy surface (PES) is determinative. Especially the correspondence near the minima of the potential energy surface is important due to the Boltzmann distribution, stating that the probability of a system to visit a certain energy level exponentially decays for increasing energies. However, in accurate models the overall shape of the PES is reproduced as well.

The adsorption of guest molecules in a nanoporous material is mainly determined by the mutual interactions between guest molecules and the interactions between the guest molecules and the nanoporous host. Therefore, frameworks and adsorbate molecules are often kept rigid if one is only interested in the adsorption properties of a nanoporous material. Since covalent force field terms, responsible for flexible behaviour are neglected, the considered interactions are fully non-covalent. Later covalent terms can be added, e.g. to account for framework breathing.

Literature offers a vast amount of force fields. Some of them are specifically designed for a certain system, while others are generally applicable. In the latter group of so-called generic force fields, the parameters are usually chosen to reproduce experimental data for a large set of reference systems (e.g. equilibrium bond lengths and angles corresponding to experimental values). An example of a popular generic force field is the Universal Force Field¹⁹ (UFF). In this force field, general rules are devised for the estimation of force field parameters, based only on the elements, their hybridization and connectivity. Another example is the DREIDING²⁰ force field. Less generally applicable are the GROMOS,²¹ OPLS²² and AMBER²³ force field. Although these were designed for a specific group of materials (GROMOS for alkanes and biological compounds, OPLS for organic liquids and AMBER for biomolecules), they gained popularity outside these fields and are therefore classified as generic force fields. Some of them were even extended in order to give better results in general applications. E.g. the AMBER force field was extended to a wider group of (pharmaceutical) molecules composed of H, C, N, O, S, P and halogens²⁴ while the OPLS force field was enriched with parameter sets for specific functional groups and biomolecules. An important aspect of force fields in this context is transferability. This signifies that the same set of parameters can be applied for different systems. Transferable force fields are therefore also applicable in large groups of materials. An example is the TraPPE²⁵ class of force fields, where for covalent interactions *ab initio* or experimental data are used to determine force field parameters, while for non-covalent interactions empirical data concerning phase equilibria are utilised.

The main drawback of generic force fields is their insufficient level of accuracy for certain applications, e.g. in order to model porphyrins with generic force fields one needs an adapted parameter set.^{26,27} For MOFs generic force fields give relatively good results (e.g. geometries can be predicted relatively accurately) but improvements are possible. Therefore a new generation of force fields was developed, able to capture the detailed structure of nanoporous materials. Interesting

examples are the UFF4MOF,²⁸ a reparametrisation of the UFF force field specifically for application in MOFs and the MOF-FF,²⁹ based on the generic MM3³⁰ force field but with alterations for both the fitting procedure and the force field contributions. Also, the QuickFF³¹ force field, successfully applied to *i.a.* MIL-53(Al)^{31,32} and MOF-5^{31,33} should be mentioned in this context. Not only are these force fields specifically designed for a certain group of materials, they also use *ab initio* data next to empirical results. This allows application to materials where experimental data are sparse and makes a more systematic approach possible.

While the force fields in the previous paragraph are capable of modeling MOF properties to a good degree, they can be improved in view of the reproduction of adsorption characteristics. Some force fields are specifically designed for these purposes, mainly focussing on the reproduction of adsorption isotherms.^{34,35} The trend towards *ab initio* derived force fields is also observed in this field. E.g. Maurin et al.,³⁶ Fang et al.³⁷ as well as Fisher et al.³⁸ employ periodic DFT calculations followed by charge partitioning to obtain the charges present in non-covalent Coulomb terms while using experimental reference data for the Lennard-Jones parameters. An important feature of this approach is the decomposition of the interaction energies in an electrostatic contribution and a contribution originating from other effects. This energy decomposition approach became even more apparent in the SIBFA³⁹ force field, the EFP method⁴⁰ and the work of Schmidt et al.⁴¹ Herein, the Symmetry Adapted Perturbation Theory^{42,43} (SAPT) decomposition of the interaction energy between two monomers is calculated by means of perturbative *ab initio* calculations. The resulting energy contributions for electrostatics, exchange-repulsion, dispersion and induction are then separately fit to a corresponding force field term. The physical interpretation of the force field contributions is an important advantage since it gives insight in the interaction processes under consideration.

Two problems that were addressed more recently are the sloppiness of fitting procedures when a large number of parameters is present⁴⁴ and the fact that many-body terms have a significant influence on interaction energies (especially in condensed phases).^{41,45–47} Most force fields neglect higher-order terms because they increase the computational cost of molecular simulations drastically. The fitting problem was tackled to some extent in the Quantum-Mechanically Derived Force Field⁴⁸ (QMDFF) where the total number of non-covalent interaction parameters is limited to 28 (in addition to the charge partitioning parameters). The Monomer Electron Density Force Field⁴⁹ (MEDFF) used in this work, not only features physical contributions, but also contains only three interaction parameters. This results in a simple but powerful model, yielding accurate results for dispersion-dominated complexes. However, many-body terms are still neglected in the MEDFF to keep molecular simulations computationally tractable. Another important aspect of the MEDFF is that, just like e.g. QuickFF it is rather a methodology than a force field. It does not consist of a large parameter set determining the complete force field but offers a way to determine the parameters with *ab initio* calculations and a specific fitting procedure. We also mention that the covalent terms in the QuickFF force field can be added to the non-covalent terms in the MEDFF, resulting in a force field capable to describe a myriad of molecular environments.

1.3 Adsorption in MIL-53(Al) and ZIF-8

1.3.1 MIL-53(Al)

The first material for which the adsorption behaviour is studied, is MIL-53(Al). This is a MOF consisting of aluminum oxides bound together by BDC linkers. The main reason behind the choice for MIL-53(Al) is the remarkable stability of the MIL-53 family of MOFs. MIL-53(Al) retains its integrity upon heating to temperatures of 723 K.⁵⁰ Above this temperature structural BDC linkers are thermally removed, resulting in the collapse of the framework.⁵¹ Moreover the material maintains this stability in a humid environment.⁵² Combining these features with the fact that the material is able to selectively adsorb CO₂ makes MIL-53(Al) a prominent candidate for carbon sequestration. Another interesting property of MIL-53(Al), is its ability to undergo structural transformations when temperature⁵³ or pressure⁵⁴⁻⁵⁶ is changed or upon exposure to certain adsorbate molecules like CO₂ and H₂O.^{50,57} When no adsorbates are present, two stable structures are observed: the large pore (lp) structure with a pore volume of 1430 Å³ and the narrow pore (np) structure with a pore size of 800 Å³.⁵⁴ Both are depicted in Figure 1.2. However, when e.g. CO₂ is adsorbed, the narrow pore structure has a pore volume of approximately 1050 Å³.

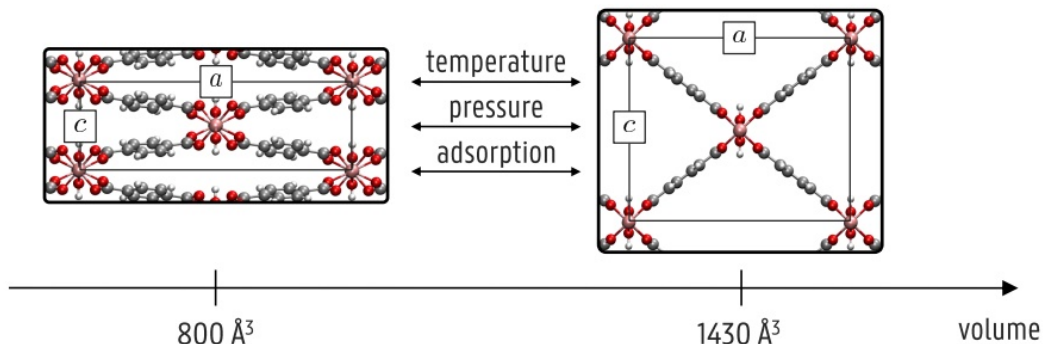


Figure 1.2: Comparison of the stable structures for MIL-53(Al). Figure taken from reference.⁵⁴

Mandal et al. studied the adsorption behaviour of MIL-53(Al) for different adsorbate gases on an experimental basis.⁵⁰ Their most important results, regarding this work, include accurate adsorption isotherms of CO₂ and N₂ for different temperatures. The adsorption isotherms for CO₂ and N₂ are displayed in Figure 1.3. Temperatures range from 294 K to 350 K. For the two lowest temperatures a Type VI adsorption isotherm is observed for CO₂, while higher temperatures yield a Type I isotherm, meaning that at lower temperatures an inflection is present while for higher temperatures no inflection points are observed.⁵⁸ The specific profile of the adsorption isotherms is explained by the breathing behaviour of MIL-53(Al). For low pressures, below 0.8 bar, the material is in the lp phase allowing a high uptake of CO₂ molecules. However, the CO₂ molecules are observed to form hydrogen-like bonds between the oxygen atoms of the carboxylate and bridging hydroxyl groups, pulling the structure together and yielding a np structure.⁵⁷ At approximately 5 bar, a second structural transformation from np to lp is observed. This

due to the high stresses resulting from the large number of adsorbed CO₂ molecules. At 314 K the material shows a similar behaviour but with higher transition pressures. For the highest temperatures, no transitions are observed.

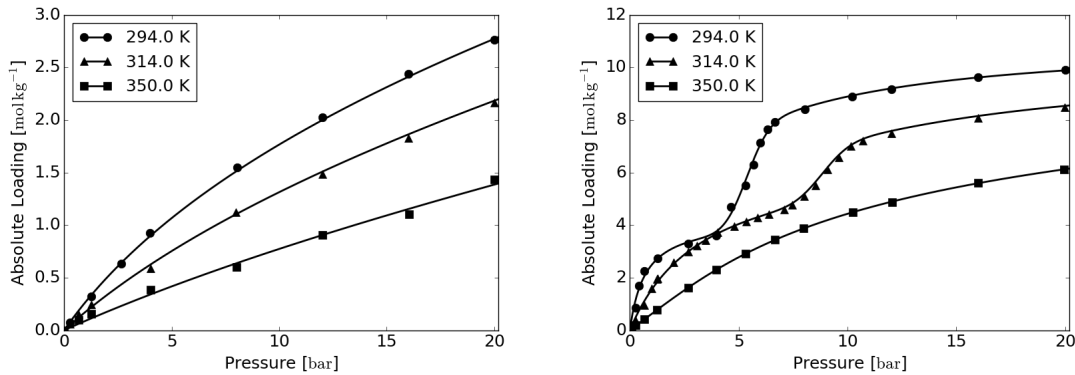


Figure 1.3: Adsorption isotherms for the adsorption of N₂ (left) and CO₂ (right) in MIL-53(Al).

In the case of N₂ no structural transformations are present because the dinitrogen molecules are unable to form the previously described hydrogen bonds. As a result, the structure remains lp for all pressures. The same goes for other important atmospheric gases like CO and CH₄. The loading of these gasses in MIL-53(Al) is also smaller than for CO₂.

1.3.2 ZIF-8

ZIF-8 is a zeolitic imidazolate framework built up by Zn atoms, tetrahedrally surrounded with methyl-imidazole linkers. It contains large pores with diameter 11.6 Å, connected by small molecular six-rings with diameter 3.4 Å.⁵⁹ Because of the narrow molecular gates, only very small molecules can diffuse efficiently through the material and fill up the pores. Even molecules like N₂ and CO₂ are impeded leading to a smaller uptake of these molecules. The CO₂ selectivity is also smaller than in MIL-53(Al). This can be observed from the experimental adsorption isotherms determined by Zhang et al. (Figure 1.4).⁶⁰ Another important difference compared to MIL-53(Al) is the lack of a structural transition in ZIF-8, yielding a Type I adsorption isotherm for both N₂ and CO₂. Also for other molecules like CO and CH₄, no breathing is observed at these temperatures. However, recent studies show that structural transitions do exist but only under specific conditions. E.g. a structural transition of ZIF-8 under N₂ adsorption is observed at cryogenic temperatures of 77 K.⁵⁹ This transition, also referred to as gate-opening, consists of a reorientation of the imidazole linkers, increasing the size of the six-ring windows as well as the pore size, thus increasing the accessibility of the pores and the loading. Diamond anvil cell experiments at elevated pressure show similar transition behaviour.⁶¹ Very recently Tanaka et al. even found that by downsizing the grain size of the ZIF-8 mono-crystals, it is possible to tune the transitional behaviour due to the increased impact of surface barriers.⁶²

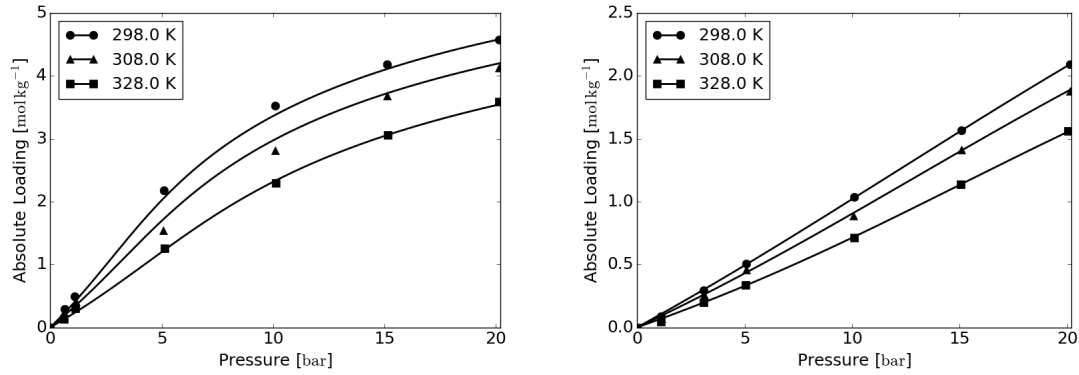


Figure 1.4: Adsorption isotherms for the adsorption of N_2 (left) and CO_2 (right) in ZIF-8.

1.4 Outline and Goal of this Thesis

This thesis aims to achieve two goals. On the one hand the MEDFF methodology, originally developed for dispersion-dominated complexes, will be applied to fluids like N_2 and CO_2 where dispersion is less dominant. Therefore, a concise review of the Monomer Electron Density Force Field is given in **Chapter 2**. The important Minimal Basis Iterative Stockholder (MBIS)⁶³ charge partitioning scheme and notable aspects in the construction of the MEDFF will be highlighted. In **Chapter 3** these concepts will be applied to the N_2 and CO_2 gases. Validity of the results will be checked thoroughly and a first important correction to the MEDFF will be implemented.

The second goal of this thesis is to extend the MEDFF methodology to describe gas adsorption in nanoporous materials. For this purpose both guest-guest and host-guest interactions are modeled by the MEDFF. While for the adsorbate gases, the parameters determined in Chapter 3, can be used again, MEDFF models for the host-guest interactions are yet to be determined. Therefore, **Chapter 4** the force field methodology will be applied to dimers, each consisting of a guest molecules and a fragment of the nanoporous material. Indeed, since high-precision SAPT and Coupled-Cluster calculations are not applicable for the complete framework, a fragmented approach provides an interesting alternative to derive force field parameters. Furthermore, adsorption energies are calculated by dispersion-corrected DFT methods, allowing to derive force field parameters via an adapted fitting procedure. The force field performance as well as the corrections proposed in Chapter 3 will be evaluated extensively. Adsorption properties of the considered MOFs are simulated by means of the constructed MEDFFs in **Chapter 5**. The resulting adsorption isotherms will be compared to both the experiment and simulations with other force fields. Finally, **Chapter 6** offers a conclusion of the performed work, describing the shortcomings of the proposed models as well.

Chapter 2

The Monomer Electron Density Force Field

Although *ab initio* quantum-mechanical calculations yield the most precise molecular information, their use in simulations is limited by their high computational cost. Classical force fields represent an alternative since they reproduce the subtleties of the quantum-mechanical reality to a good degree, while keeping calculations computationally tractable. In this work the Monomer Electron Density Force Field⁴⁹ will be used as starting point. As mentioned before, this is a pairwise additive, non-covalent force field with two important features. On the one hand, the number of parameters determining the interactions is limited, thus reducing typically ill-conditioned fits. On the other hand each contribution to the potential energy is physically inspired, giving some insight in the physics behind the interaction of the molecules. In this chapter the methodology behind the force field will be reviewed, followed by some remarks. Subsequent chapters will apply and correct the force field where necessary, enabling it to describe gas adsorption in MOFs.

2.1 Methodology

The different contributions to the MEDFF are based on the SAPT (Symmetry Adapted Perturbation Theory)^{42,43} decomposition of the interaction energy between two monomers. This decomposition divides the interaction energy in four contributions: electrostatics, exchange-repulsion, dispersion and induction. The same four contributions will be present in each pairwise term of the force field, thus yielding:

$$E_{\text{MEDFF}} = \sum_{\text{dimers}} E_{\text{inter}} \quad (2.1)$$
$$E_{\text{inter}} = E_{\text{elst}} + E_{\text{exch-rep}} + E_{\text{disp}} + E_{\text{ind}}$$

All parameters of these contributions are determined by *ab initio* calculations performed on the equilibrium structure of the monomers on the one hand and on a group of dimer configurations on the other hand. The monomer calculations result in a high quality ground state monomer electron density. This electron density is afterwards subjected to charge partitioning by means of the MBIS scheme.⁶³ The resulting atomic parameters completely determine the electrostatic

contribution to the interaction energy while for the other three terms an additional interaction parameter is introduced. These three parameters are determined by fitting the force field to *ab initio* SAPT interaction energies for the selected dimers. The interaction parameters are thereafter refined by means of *ab initio* CCSD(T) (Coupled-Cluster) calculations for the same dimers.

2.1.1 Minimal Basis Iterative Stockholder

The Minimal Basis Iterative Stockholder (MBIS) scheme⁶³ is based on the assumption that electron densities in atoms and molecules resemble superpositions of spherical Slater functions, making it possible to approximate the total electron density by the following model electron density:

$$\tilde{\rho}^e(\mathbf{r}) = \sum_{A=1}^{N_{\text{atoms}}} \sum_{i=1}^{m_A} \tilde{\rho}_{A_i}^e(\mathbf{r}) = \sum_{A=1}^{N_{\text{atoms}}} \sum_{i=1}^{m_A} \frac{N_{A_i}}{\sigma_{A_i}^3 8\pi} \exp\left(-\frac{|\mathbf{r} - \mathbf{R}_A|}{\sigma_{A_i}}\right) \quad (2.2)$$

Herein the first summation runs over all atoms in the molecule (thus decomposing the molecular density in atomic contributions) while the second runs over the atomic shells of each atom. N_{A_i} is the number of electrons in shell i of atom A , while σ_{A_i} is the width of this shell. The shells are centered around \mathbf{R}_A , the position of the corresponding atomic nucleus, and normalised in such way that the density integrates to the sum of all N_{A_i} . The parameters present in this model density are determined by minimizing the Kullback-Leibler divergence describing the difference in information entropy between the real, *ab initio* density $\rho^e(\mathbf{r})$ and the model density $\tilde{\rho}^e(\mathbf{r})$. This minimization procedure then yields:

$$\begin{aligned} N_{A_i} &= \int \rho^e(\mathbf{r}) \frac{\tilde{\rho}_{A_i}^e(\mathbf{r})}{\tilde{\rho}^e(\mathbf{r})} d\mathbf{r} \\ \sigma_{A_i} &= \frac{1}{3N_{A_i}} \int \rho^e(\mathbf{r}) \frac{\tilde{\rho}_{A_i}^e(\mathbf{r})}{\tilde{\rho}^e(\mathbf{r})} |\mathbf{r} - \mathbf{R}_A| d\mathbf{r} \end{aligned} \quad (2.3)$$

By means of a self-consistent algorithm the parameters can thus be solved for, once a high quality monomer electron density is determined by means of *ab initio* calculations. Not only does the MBIS procedure offer an analytical approximation for the electron density, it also provides a scheme to partition the *ab initio* density $\rho^e(\mathbf{r})$ in atomic contributions $\rho_A^e(\mathbf{r})$:

$$\rho_A^e(\mathbf{r}) = \rho^e(\mathbf{r}) \sum_{i=1}^{m_A} \frac{\tilde{\rho}_{A_i}^e(\mathbf{r})}{\tilde{\rho}^e(\mathbf{r})} = \rho^e(\mathbf{r}) \frac{\tilde{\rho}_A^e(\mathbf{r})}{\tilde{\rho}^e(\mathbf{r})} = \rho^e(\mathbf{r}) w_A(\mathbf{r}) \quad (2.4)$$

Herein, $w_A(\mathbf{r})$ is the weight function of atom A. By construction, the weight functions sum to 1 for all \mathbf{r} . In the MEDFF, a slight simplification of the MBIS model densities is applied. The populations of all but the valence shell of each atom are summed together to one electron core charge. This charge is then added to the charge of the nucleus yielding a net core charge, centered on the nucleus of each atom. For the valence shells however, the electron density remains smeared out in space. Introducing the core charge of atom A, q_{A_c} as:

$$q_{A_c} = Z_A - \sum_{i=1}^{m_A-1} N_{A_i} \quad (2.5)$$

the MBIS model for the charge density, present in the MEDFF, can be summarised as:

$$\begin{aligned}\rho(\mathbf{r}) &\approx \tilde{\rho}(\mathbf{r}) = \tilde{\rho}_v(\mathbf{r}) + \tilde{\rho}_c(\mathbf{r}) \\ \tilde{\rho}_v(\mathbf{r}) &= - \sum_{A=1}^{N_{\text{atoms}}} \frac{N_{A_v}}{\sigma_{A_v}^3 8\pi} \exp\left(-\frac{|\mathbf{r} - \mathbf{R}_A|}{\sigma_{A_v}}\right) \\ \tilde{\rho}_c(\mathbf{r}) &= \sum_{A=1}^{N_{\text{atoms}}} q_{A_c} \delta(\mathbf{r} - \mathbf{R}_A)\end{aligned}\quad (2.6)$$

Here $\rho(\mathbf{r})$ is the molecular charge density, $\tilde{\rho}(\mathbf{r})$ its MBIS approximation consisting of a delocalized valence charge density $\tilde{\rho}_v(\mathbf{r})$ and a point charge at each nucleus $\tilde{\rho}_c(\mathbf{r})$.

2.1.2 Force Field Contributions

Each pairwise term of the force field counts four contributions (Eq. 2.1). We now discuss these contributions separately, focussing on a simple overview of the force field. For more mathematical detail, one should consult the work of Vandenbrande et al.⁴⁹

Electrostatics

The electrostatics contribution is determined by the Coulomb integral between the frozen monomer charge densities. This means that electron clouds are not deformed due to interaction between the monomers. The frozen charge densities are approximated by their MBIS model (Eq. 2.6) and the electrostatic contribution to the interaction energy is thus:

$$\begin{aligned}E_{\text{elst}} &= \int d\mathbf{r}_1 \int d\mathbf{r}_2 \frac{\tilde{\rho}_v^1(\mathbf{r}_1) \tilde{\rho}_v^2(\mathbf{r}_2)}{|\mathbf{r}_1 - \mathbf{r}_2|} \\ &= \sum_{A=1}^{N_{\text{atoms}}^1} \sum_{B=1}^{N_{\text{atoms}}^2} \frac{q_{A_c} q_{B_c}}{|\mathbf{R}_A - \mathbf{R}_B|} + \sum_{A=1}^{N_{\text{atoms}}^1} q_{A_c} \int d\mathbf{r}_2 \frac{\tilde{\rho}_v^2(\mathbf{r}_2)}{|\mathbf{r}_2 - \mathbf{R}_A|} \\ &\quad + \sum_{B=1}^{N_{\text{atoms}}^2} q_{B_c} \int d\mathbf{r}_1 \frac{\tilde{\rho}_v^1(\mathbf{r}_1)}{|\mathbf{r}_1 - \mathbf{R}_B|} + \int d\mathbf{r}_1 \int d\mathbf{r}_2 \frac{\tilde{\rho}_v^1(\mathbf{r}_1) \tilde{\rho}_v^2(\mathbf{r}_2)}{|\mathbf{r}_1 - \mathbf{r}_2|}\end{aligned}\quad (2.7)$$

where the superscripts indicate the different monomers. Plugging in Eq. 2.6 for the model densities, one can rewrite this as a sum of interatomic terms.

$$\begin{aligned}E_{\text{elst}} &= \sum_{A=1}^{N_{\text{atoms}}^1} \sum_{B=1}^{N_{\text{atoms}}^2} E_{\text{elst}}^{AB} \\ E_{\text{elst}}^{AB} &= \frac{q_{A_c} q_{B_c}}{R_{AB}} - \frac{q_{A_c} N_{B_v}}{R_{AB}} [1 - g(\sigma_{B_v}, R_{AB})] - \frac{q_{B_c} N_{A_v}}{R_{AB}} [1 - g(\sigma_{A_v}, R_{AB})] \\ &\quad + \frac{N_{A_v} N_{B_v}}{R_{AB}} [1 - f(\sigma_{A_v}, \sigma_{B_v}, R_{AB}) - f(\sigma_{B_v}, \sigma_{A_v}, R_{AB})] \\ g(\sigma, r) &= \left(1 + \frac{r}{2\sigma}\right) \exp\left(-\frac{r}{\sigma}\right) \\ f(\sigma_i, \sigma_j, r) &= \frac{\sigma_i^4}{(\sigma_i^2 - \sigma_j^2)^2} \left[1 + \frac{r}{2\sigma_i} - \frac{2\sigma_j^2}{\sigma_i^2 - \sigma_j^2}\right] \exp\left(-\frac{r}{\sigma_i}\right)\end{aligned}\quad (2.8)$$

In contrast to the other force field contributions, electrostatics is not provided with an interaction parameter and is thus completely determined by the MBIS parameters.

Exchange-Repulsion

The Pauli exclusion principle demands the complete wavefunction of a dimer to be antisymmetric. This yields a higher energy expectation value for the antisymmetrized dimer wavefunction than for a simple product state of the two monomer wavefunctions. This repulsive energy is observed to be approximately proportional to the overlap between the frozen monomer electron densities.⁶⁴ Introducing a first interaction parameter $U_{\text{exch}-\text{rep}}$ as a proportionality constant, one can thus write that:

$$\begin{aligned} E_{\text{exch}-\text{rep}} &\approx U_{\text{exch}-\text{rep}} S_{12} \\ &\approx U_{\text{exch}-\text{rep}} \int \tilde{\rho}_v^1(\mathbf{r}) \tilde{\rho}_v^2(\mathbf{r}) d\mathbf{r} \end{aligned} \quad (2.9)$$

Inserting the MBIS approximation for the electron densities then yields:

$$\begin{aligned} E_{\text{exch}-\text{rep}} &= \sum_{A=1}^{N_{\text{atoms}}^1} \sum_{B=1}^{N_{\text{atoms}}^2} E_{\text{exch}-\text{rep}}^{AB} \\ E_{\text{exch}-\text{rep}}^{AB} &= U_{\text{exch}-\text{rep}} S^{AB} \\ S^{AB} &= \frac{N_{A_v} N_{B_v}}{8\pi R_{AB}} [h(\sigma_{A_v}, \sigma_{B_v}, R_{AB}) + h(\sigma_{B_v}, \sigma_{A_v}, R_{AB})] \\ h(\sigma_i, \sigma_j, r) &= \left[\frac{4\sigma_i^2 \sigma_j^2}{(\sigma_j^2 - \sigma_i^2)^3} + \frac{\sigma_i}{(\sigma_j^2 - \sigma_i^2)^2} r \right] \exp\left(-\frac{r}{\sigma_i}\right) \end{aligned} \quad (2.10)$$

Dispersion

Dispersion forces arise from attractive electrostatic interactions between fluctuations in the monomer electron densities. The second-order SAPT decomposition of the interaction energy between two monomers shows a typical negative-power dependency on the intermolecular distance for the dispersion contribution:⁴³

$$E_{\text{disp}} = -\frac{C_6}{R^6} - \frac{C_8}{R^8} - \frac{C_{10}}{R^{10}} - \dots \quad (2.11)$$

Again resorting to a sum of interatomic interaction terms, the dispersion contribution to the force field written as:

$$\begin{aligned} E_{\text{disp}} &= \sum_{A=1}^{N_{\text{atoms}}^1} \sum_{B=1}^{N_{\text{atoms}}^2} E_{\text{disp}}^{AB} \\ E_{\text{disp}}^{AB} &= -f_6(x_{AB}) \frac{C_{AB}^6}{R_{AB}^6} - U_{s8} f_8(x_{AB}) \frac{C_{AB}^8}{R_{AB}^8} \\ f_n(x) &= 1 - \left(\sum_{k=1}^n \frac{x^k}{k!} \right) \exp(-x) \end{aligned} \quad (2.12)$$

Herein, the first two typical power terms are multiplied by Tang-Toennies damping functions.⁶⁵ These account for the dispersion behaviour at low distances and have as argument the interatomic distance divided by the average of the corresponding Slater widths:

$$x_{AB} = \frac{R_{AB}}{\frac{\sigma_{A_v} + \sigma_{B_v}}{2}} \quad (2.13)$$

U_{s8} represents a second interaction parameter, determining the strength of the higher order term. For the C_{AB}^6 -coefficients, the Tkatchenko-Scheffler⁶⁶ method is applied, adjusting free atom reference values for C_{AB}^6 based on the MBIS charge partitioning. For the C_{AB}^8 coefficients on the other hand, the Starkschall recursion relation⁶⁷ is used:

$$C_{AB}^8 = \frac{3}{2} C_{AB}^6 \left(\frac{\langle r_A^4 \rangle}{\langle r_A^2 \rangle} + \frac{\langle r_B^4 \rangle}{\langle r_B^2 \rangle} \right) \quad (2.14)$$

For the expectation values, free atom electron densities are utilized.

Induction

Bringing two molecules together leads to deformation of the electron clouds. This polarisation effect results in an energy stabilisation (compared to frozen monomer densities), called induction. Polarizable force fields attempt to capture this effect by, for instance, introducing an inducible charge or dipole for each atom. However, this complicates the force field considerably and introduces a lot of new parameters which is unwanted. Therefore a more simple model for the induction interaction only makes use of one interaction parameter U_{ind} . In this model, proposed by Stone and Misquitta,⁴⁵ the induction energy is simply proportional to the overlap:

$$E_{\text{ind}} = U_{\text{ind}} S_{12} \quad (2.15)$$

Calculation of S_{12} by introducing the MBIS charge model was already performed for the exchange interaction (Eq. 2.10).

2.1.3 Interaction Parameters

The three interaction parameters are the only unknowns left to be determined. A least squares fit, matching the different force field contributions to their corresponding *ab initio* SAPT values, accomplishes this task. As reported in the work of Vandenbrande et al.⁴⁹ and references therein, SAPT2+(3) (*i.e.* symmetry-adapted perturbation theory with exact perturbations up to the second order and approximative third-order perturbations) is the most accurate SAPT implementation with a clear distinction between electrostatics, exchange-repulsion, induction and dispersion. Therefore, SAPT2+(3) interaction energies are used to fit interaction parameters. The fact that SAPT2+(3) performs better than SAPT2+3 also illustrates that the perturbative SAPT series are not yet completely converged. Also, higher order terms are not interpreted straightforwardly and are difficult to classify into distinct SAPT energy contributions. Therefore, the force field parameters, as determined by SAPT, are refined by fitting interaction energies to even more accurate CCSD(T)⁶⁸ data. Since the physical interpretation of the different contributions should be safeguarded, the fit is restrained to reduce the change in the interaction parameters. Tykhonov regularisation is applied, yielding the following cost function:

$$\chi^2 = \frac{1}{2} \sum_{n=1}^{N_d} \frac{(E_{FF}^n[\mathbf{U}] - E_{ref}^n)^2}{N_d} + \frac{1}{2\sigma_{pr}^2} \sum_{\alpha=1}^3 \left(\frac{U_\alpha - U_\alpha^{SAPT}}{U_\alpha^{SAPT}} \right)^2 \quad (2.16)$$

The first sum runs over all of the N_d data points for the dimers while the second runs over all interaction parameters U_α in the vector \mathbf{U} . The parameter σ_{pr} determines the strength of the regularisation. $\sigma_{pr} = 0 \text{ mol kJ}^{-1}$ implies strong regularisation and in this case the interaction parameters are simply equal to their SAPT values U_α^{SAPT} . $\sigma_{pr} = \infty \text{ mol kJ}^{-1}$ on the other hand implies weak regularisation resulting in a pure CCSD(T) fit of the force field. A good value for the regularisation parameter is located between these two extremes and was ascertained to be 0.1 mol kJ^{-1} by studying the estimated prediction error for dispersion dominated complexes in the S66x8 database of dimers.⁴⁹ In this work however, the optimal value for the σ_{pr} parameter will be determined on a case-specific basis.

Chapter 3

Guest-Guest Interactions

The Monomer Electron Density Force Field (MEDFF) was originally developed to describe interactions in dispersion-dominated complexes. In this chapter, however, the methodology will be applied to N₂ and CO₂ fluids where dispersion is less dominant. First, an overview of the force field construction process is given after which the results are validated both internally and externally. For CO₂ an important correction to the force field, based on multipole expansions, is studied as well. In the following chapters, the resulting force fields will be applied to describe guest-guest interactions in adsorption simulations.

3.1 N₂

3.1.1 Force Field Construction

The first step in the construction of a MEDFF for a fluid is the computation of the electron density for the monomers in the fluid, followed by an MBIS partitioning of this density. In this work, the densities were determined in the B3LYP^{69,70}/aug-cc-pVTZ⁷¹ and CCSD⁶⁸/aug-cc-pVTZ level of theory via the Gaussian⁷² program and MBIS partitioning was performed by Horton.⁷³ For the N₂ monomers an experimental bond length of 1.098 Å⁷⁴ was kept fixed. The resulting charges and valence shell widths are displayed in Table 3.1. Based on symmetry, one expects both atoms to have equally large and opposite core and valence charges, resulting in zero atomic charges. This is confirmed in Table 3.1 (small differences occur due to numerical errors but are of the order of 0.001 a.u.). The B3LYP/aug-cc-pVTZ and CCSD/aug-cc-pVTZ LoT also result in the same set of charges and widths. However, the radial expectation values used in Eq. (2.14) are not identical. As a result, force field contributions will differ in both levels of theory.

Atom	B3LYP/aug-cc-pVTZ				CCSD/aug-cc-pVTZ			
	q _c	q _v	σ _v	q _{tot}	q _c	q _v	σ _v	q _{tot}
N	5.37	-5.37	0.43	0.00	5.37	-5.37	0.43	0.00
N	5.37	-5.37	0.43	0.00	5.37	-5.37	0.43	0.00

Table 3.1: MBIS parameters (in a.u.) for the MEDFF of N₂ in the B3LYP/aug-cc-pVTZ and CCSD/aug-cc-pVTZ level of theory.

Next, SAPT and CCSD(T) interaction energies are calculated for a set of dimer configurations using the Psi4⁷⁵ program. For the SAPT calculations the aug-cc-pVTZ basis set was used again. CCSD(T) interaction energies, on the other hand, were determined in the complete basis set (CBS) limit wherefore the scheme used in the paper of Hobza et al.⁷⁶ was applied. Since the force field should mainly reproduce the interaction energy close to its minima (these are physically the most important energies), the data points have to be chosen around the minima of the PES. For N₂, literature^{77,78} indicates five energetically important configurations (each carrying certain symmetry elements). The definition of these L, T, H, X and Z configurations is illustrated in Figure 3.1. In the used axis system, the geometrical center of both molecules lies on the z-axis. The relative orientation is then completely determined by three angles (θ_1, θ_2, Φ) as displayed below.

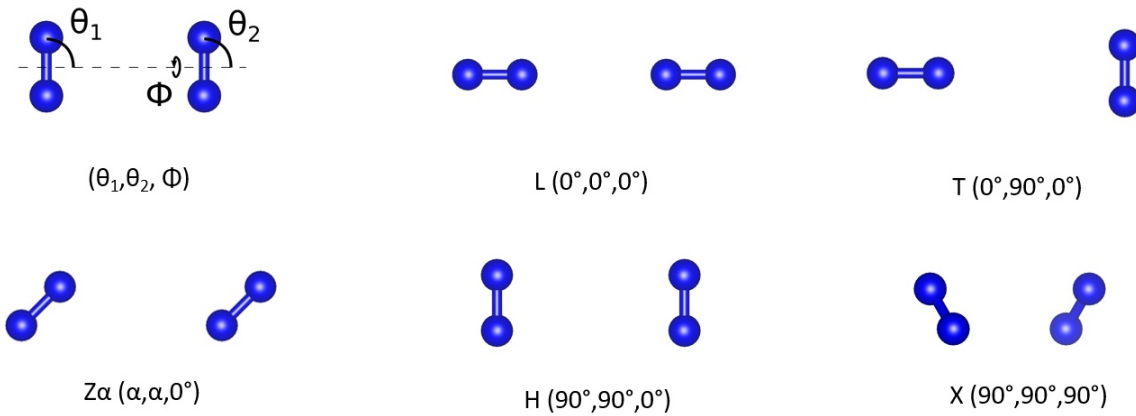


Figure 3.1: Dimer configurations for which *ab initio* calculations are performed. The configurations are determined by the three angles (θ_1, θ_2, Φ).

It was found that the T and Z45 ($\alpha = 45^\circ$) configurations are the most stable for typical intermolecular separations of about 4.7 Å with very small mutual energy differences depending on the used LoT (Level of Theory). The L configuration on the other hand is unstable and its energy is so high that it is excluded from the data set. For the other configurations single point calculations are performed around the equilibrium separation by scaling this separation with the Hobza distance multiplier (DM):⁷⁹

$$\text{DM} = 100 \frac{R_{AB,\text{min}}}{R_{AB,\text{min}}^{\text{eq}}} \quad (3.1)$$

Here, $R_{AB,\text{min}}$ is the minimal interatomic distance for atoms belonging to different monomers, while $R_{AB,\text{min}}^{\text{eq}}$ is equal to this value in the configurational minimum. Using this measure for the intermolecular separation makes sure that all dissociation profiles have a similar shape (e.g. minimum at DM=100). The complete dataset is then built up by ten separations (DMs between 90 and 200) for the T, Z45, H and X configurations, resulting in 40 data points for both SAPT and CCSD(T) calculations. Figure 3.2 shows the corresponding dissociation curves.

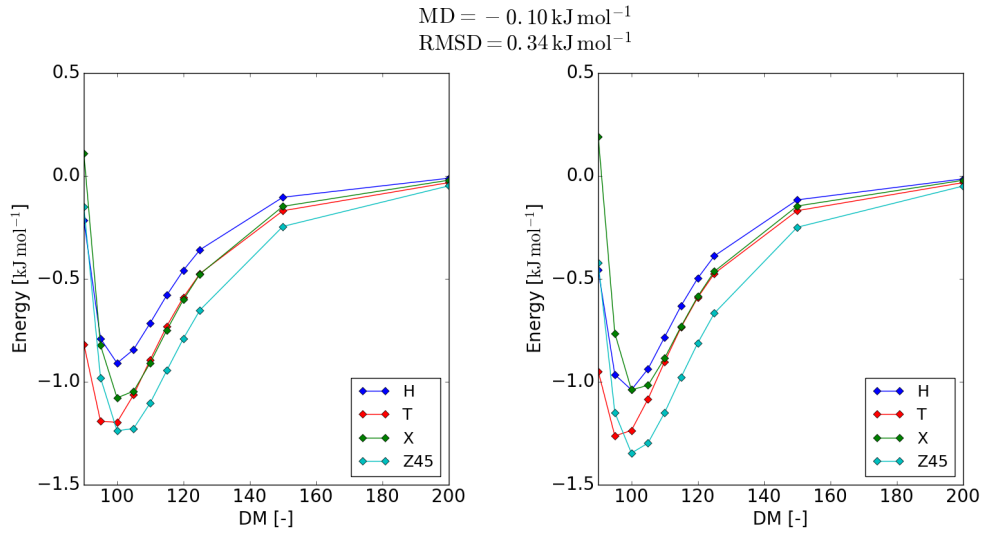


Figure 3.2: Ab initio calculated dissociation profiles for different configurations of the N₂ dimer in the CCSD(T)/aug-cc-pVTZ (left) and SAPT/aug-cc-pVTZ (right) level of theory.

The construction of the force field is finalized by fitting the force field to the *ab initio* reference data. First, a separate fit of the force field contributions to the corresponding SAPT energies is performed after which a constrained fit of the whole force field to CCSD(T) data yields the final interaction parameters. An important parameter is σ_{pr} (Eq. (2.16)), whose influence is evaluated in Figure 3.3. The red curves show that for low values of σ_{pr} , *i.e.* in the SAPT limit, the relative root-mean-squared deviation between the final parameters and their SAPT values, RMSD_U, decays to zero while the RMSD of the force field compared to *ab initio* CCSD(T) results, RMSD_{CCSD(T)}, saturates to a maximum. For high values of σ_{pr} on the other hand, the final interaction parameters differ about 45% from their SAPT values (using B3LYP/aug-cc-pVTZ densities) while the RMSD_{CCSD(T)} drops down to a minimum. For CCSD densities, the variations are even more distinct.

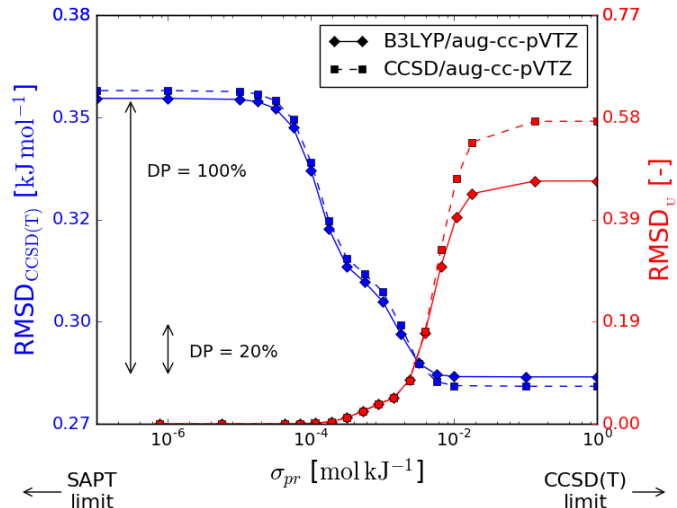


Figure 3.3: Influence of the regularisation strength on RMSD_{CCSD(T)} and RMSD_U.

An ideal value for the σ_{pr} parameter is located between the SAPT and CCSD(T) limit. Indeed, pure SAPT interaction parameters result in a relatively inaccurate reproduction of *ab initio* energies (an RMSD of 0.34 kJ mol⁻¹ compared to CCSD(T) data was found for N₂ in Figure 3.2) while pure CCSD(T) interaction parameters partially lose their physical interpretation. Even though RMSD_{CCSD(T)} and RMSD_U typically have shapes similar to those displayed in Figure 3.3, the region where the transition occurs is system-dependent. Therefore, the deviation percentage (DP) was introduced, indicating by means of a percentage how much the RMSD_{CCSD(T)} deviates from its CCSD(T) limit for a certain σ_{pr} value. It is defined as:

$$DP(\sigma_{pr}) = 100 \frac{\text{RMSD}_{\text{CCSD(T)}}(\sigma_{pr}) - \text{RMSD}_{\text{CCSD(T)}}(\sigma_{pr} = \infty)}{\text{RMSD}_{\text{CCSD(T)}}(\sigma_{pr} = 0) - \text{RMSD}_{\text{CCSD(T)}}(\sigma_{pr} = \infty)} \quad (3.2)$$

Rather than σ_{pr} , the deviation percentage allows to specify interaction parameter sets in a system-independent way. The definition of this concept was also illustrated in Figure 3.3 for N₂. Interaction parameters were determined for DP values of 10% and 20% because in these cases the RMSD_U is still limited while the CCSD(T) precision is relatively high. The interaction parameters in the SAPT and CCSD(T) limit were calculated as well and results are displayed in Table 3.2.

DP	B3LYP/aug-cc-pVTZ				CCSD/aug-cc-pVTZ			
	σ_{pr}	$U_{\text{exch-rep}}$	U_{ind}	U_{s8}	σ_{pr}	$U_{\text{exch-rep}}$	U_{ind}	U_{s8}
0%	∞	7.785	-0.469	0.228	∞	7.640	-0.475	0.016
10%	2.505	8.585	-0.471	0.615	2.925	8.483	-0.468	0.431
20%	1.480	8.999	-0.469	0.818	1.847	8.879	-0.467	0.627
100%	0.000	8.794	-0.470	1.071	0.000	8.747	-0.467	0.919

Table 3.2: Regularisation parameters (in mmol kJ⁻¹) and corresponding interaction parameters (in a.u.) for the MEDFF of N₂.

Figure 3.4 illustrates how the interaction parameters change when σ_{pr} is altered. Because both exchange-repulsion and induction are proportional to the overlap between two monomers, changing $U_{\text{exch-rep}}$ or U_{ind} by the same amount has exactly the same influence on the force field. However, relative changes in interaction parameters are suppressed by the second term in the fitting cost function (Eq. (2.16)). Therefore both curves will have a similar shape but $U_{\text{exch-rep}}$, whose magnitude is larger, is allowed to change more than U_{ind} in absolute value. As Figure 3.3 already showed, interaction parameters differ significantly from the SAPT values in the CCSD(T) limit. This is especially the case for the dispersion parameter U_{s8} , which becomes almost zero for high σ_{pr} values, compromising its physical validity. Combining the three graphs in Figure 3.4, one concludes that by increasing the deviation percentage (and thus decreasing σ_{pr}), the force field first experiences two opposing influences because both U_{s8} and the sum of $U_{\text{exch-rep}}$ and U_{ind} increase. The former makes the force field more attractive while the latter renders it more repulsive. However, once σ_{pr} becomes smaller than 0.001 mol kJ⁻¹, U_{s8} stays approximately the same and the sum of $U_{\text{exch-rep}}$ and U_{ind} decreases. The force field thus becomes more attractive in the SAPT limit. This is consistent with SAPT interaction energies being more attractive than CCSD(T), as expressed by the negative MD in Figure 3.2.

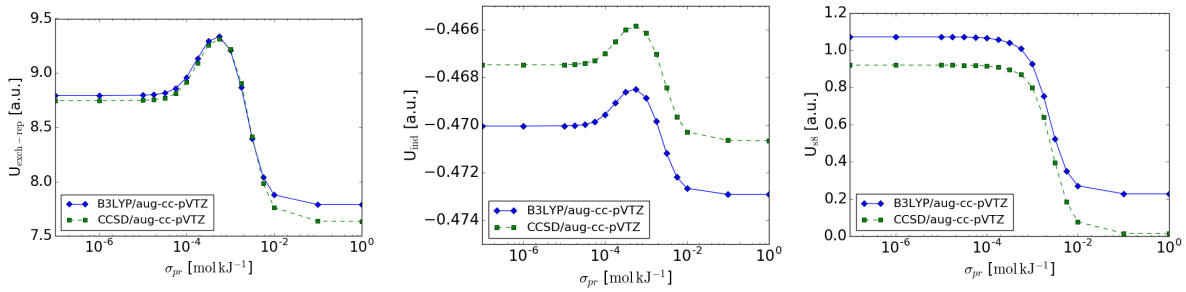


Figure 3.4: Influence of the regularisation strength on the interaction parameters in both levels of theory for the monomer densities.

3.1.2 Validation

The constructed force field is validated in two ways: internally and externally. The internal validation itself consists of two parts. On the one hand interaction parameters are compared to reference values for the dispersion dominated complexes in the S66x8 database,⁷⁶ since it was found that the parameters for this set are system-independent to some extent.⁴⁹ However, correspondence to the reference parameters is not a stringent condition for force field validity. On the other hand, the reproduction of *ab initio* calculated interaction energies (Figure 3.2) is checked. External validation proceeds via comparison with experimental second virial coefficients and vapor-liquid coexistence curves (VLCCs).

Internal Validation

In Table 3.3, the interaction parameters for N₂ in the limiting cases DP = 0% and DP = 100% are compared to the reference values for the dispersion dominated complexes in the S66x8 database. SAPT calculations show that N₂ is a dispersion dominated complex by the definition of Hobza et al.⁷⁶ Indeed, for the equilibrium configuration in the CCSD(T) LoT (*i.e.* the Z45 configuration for DM=100) the dispersion/electrostatics ratio is equal to 2.99, which is higher than 1.7. Interaction parameters should hence be comparable to the reference values. For the exchange repulsion, relatively good correspondence is observed while for the induction and dispersion parameters substantial deviations are observed. One concludes that N₂ behaves differently than most dispersion dominated complexes. A possible explanation is the fact that dispersion is not extremely dominant in N₂ complexes. Indeed, in CH₄ complexes for instance, the dispersion/electrostatics ratio is 7.64, more than 2.5 times as high as in N₂ complexes.

DP	B3LYP/aug-cc-pVTZ			CCSD/aug-cc-pVTZ			Reference		
	$U_{\text{exch-rep}}$	U_{ind}	U_{s8}	$U_{\text{exch-rep}}$	U_{ind}	U_{s8}	$U_{\text{exch-rep}}$	U_{ind}	U_{s8}
0%	7.79	-0.47	0.23	7.64	-0.48	0.02	8.27	-0.86	0.48
100%	8.79	-0.47	1.07	8.75	-0.47	0.92	8.13	-0.87	0.57

Table 3.3: Comparison between the interaction parameters (in a.u.) of the MEDFF for N₂ and the corresponding reference values for the S66x8 database.

More important for the validity of the force field is the reproduction of *ab initio* calculated dissociation profiles by the force field. As Figure 3.5 shows the correspondence is not particularly outstanding for the MEDFF of N₂ with DP = 20%. The H and X configurations are overbound while T and Z45 configurations are underbound. In molecular simulations for N₂, thermodynamic quantities like virial coefficients and fluid densities are determined by phase space averages and therefore these relatively small microscopic errors could cancel each other out. However, a poor reproduction of microscopic details could cause problems in adsorption simulations, e.g. the inability of the force field to detect preferential adsorption sites.

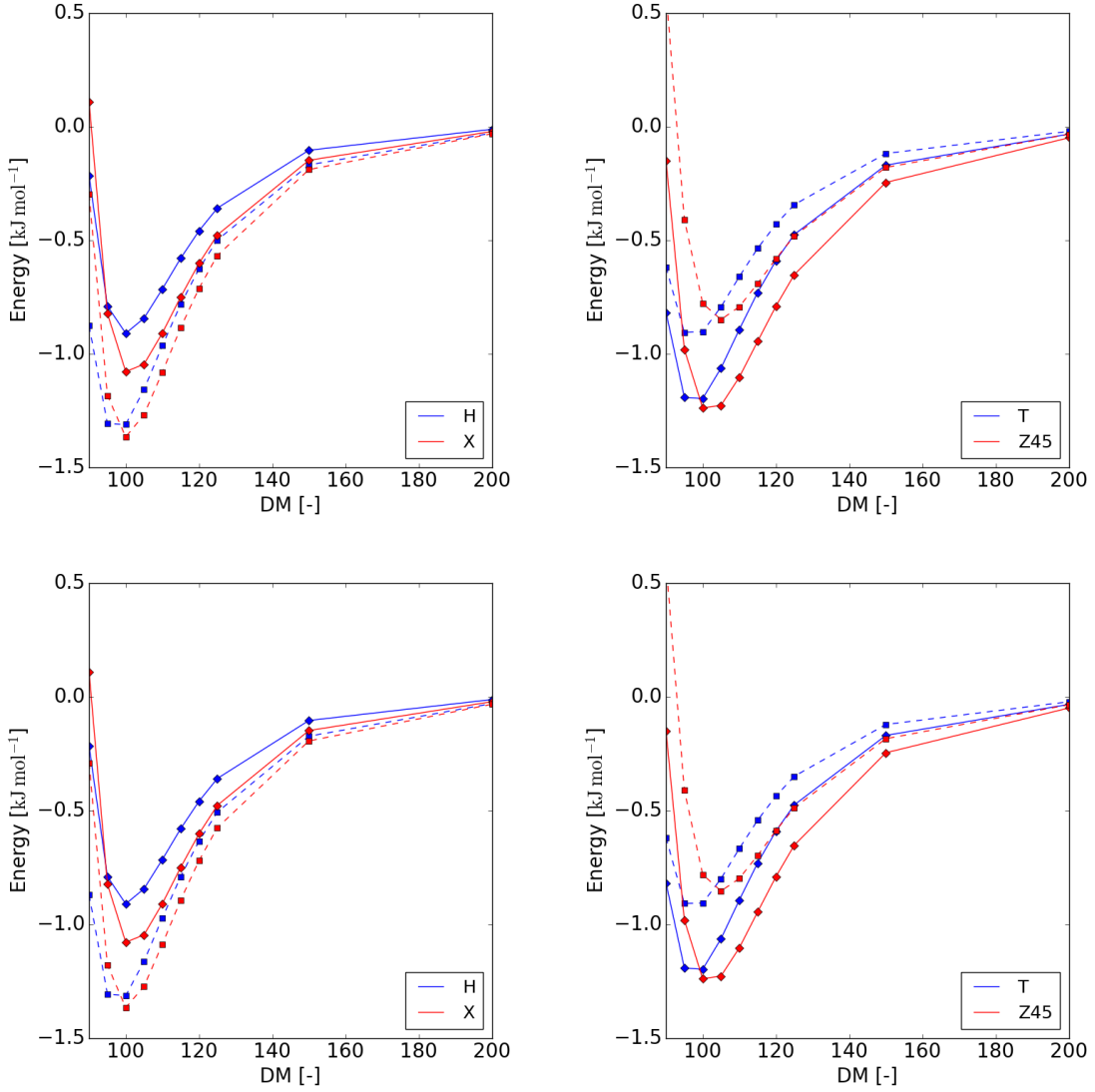


Figure 3.5: Comparison between *ab initio* calculated CCSD(T)/aug-cc-pVTZ dissociation profiles for N₂ (\diamond , full line) and the MEDFF approximation hereof (\square , dashed line) with DP = 20% and B3LYP/aug-cc-pVTZ (top) or CCSD/aug-cc-pVTZ (bottom) monomer densities.

In Figure 3.6 the reproduction of the different SAPT contributions is evaluated. Comparing the RMSDs with the typical magnitudes of the energy contributions, exchange is reproduced the best, followed by dispersion and induction. The highest relative deviations are found for the

electrostatics contribution. Since this contribution contains no interaction parameters, deviations are due to an insufficiently accurate model for the electron densities. More specifically, an inaccurate reproduction of multipole moments on the one hand and the penetration effect on the other hand, could explain the observed deviations. For CO₂, this problem will be studied in more detail.

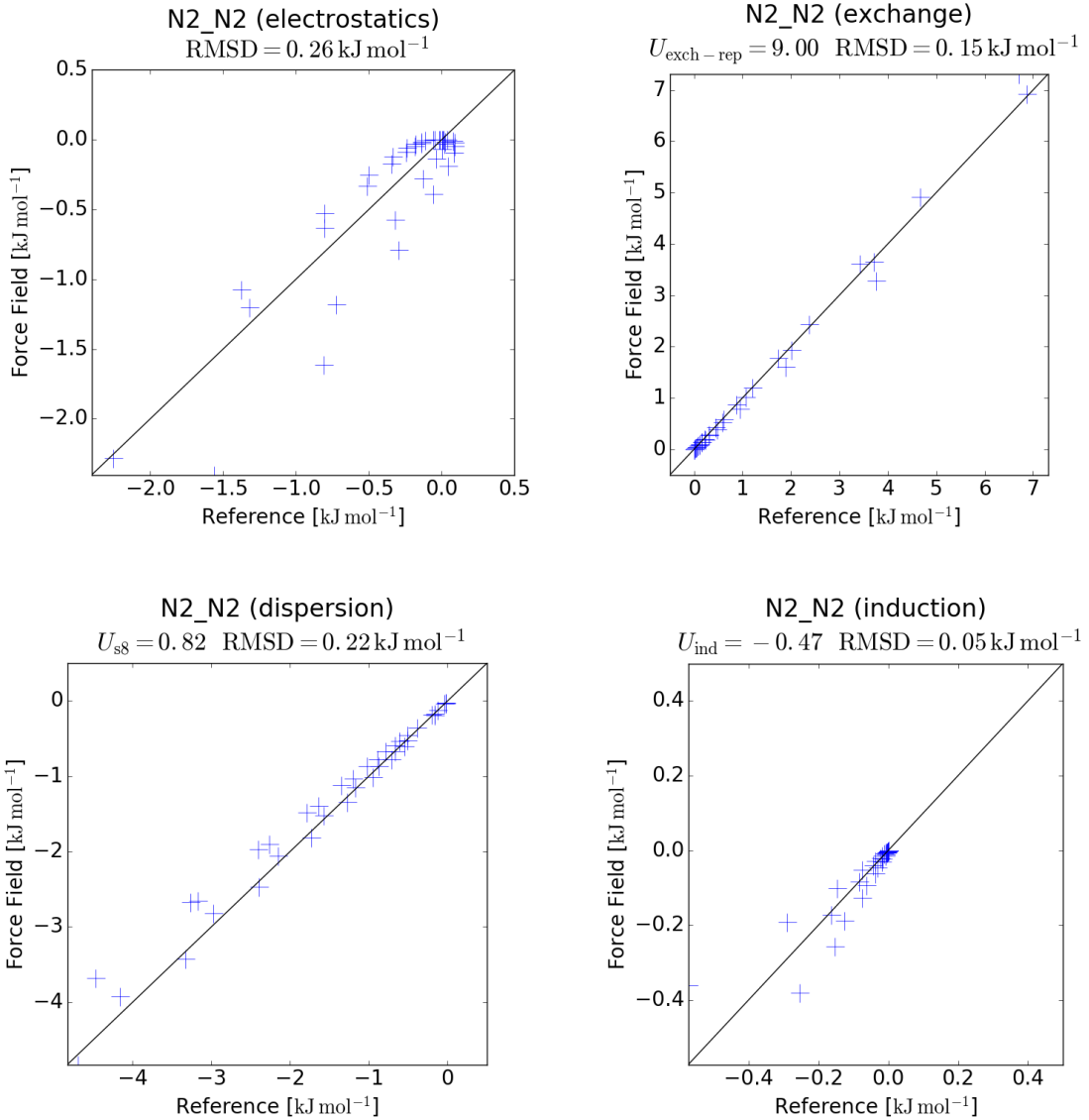


Figure 3.6: Comparison between *ab initio* calculated SAPT interaction energy contributions for N₂ and the MEDFF approximation hereof. DP = 20% and B3LYP/aug-cc-pVTZ monomer densities were utilised.

Finally, Figure 3.7 compares the overall force field performance of the MEDFF for the different levels of theory used to calculate the monomer densities. As Figure 3.5 already indicated, both force fields behave almost exactly the same. Figure 3.7 also confirms that about half the data points are overbound while the other half is underbound.

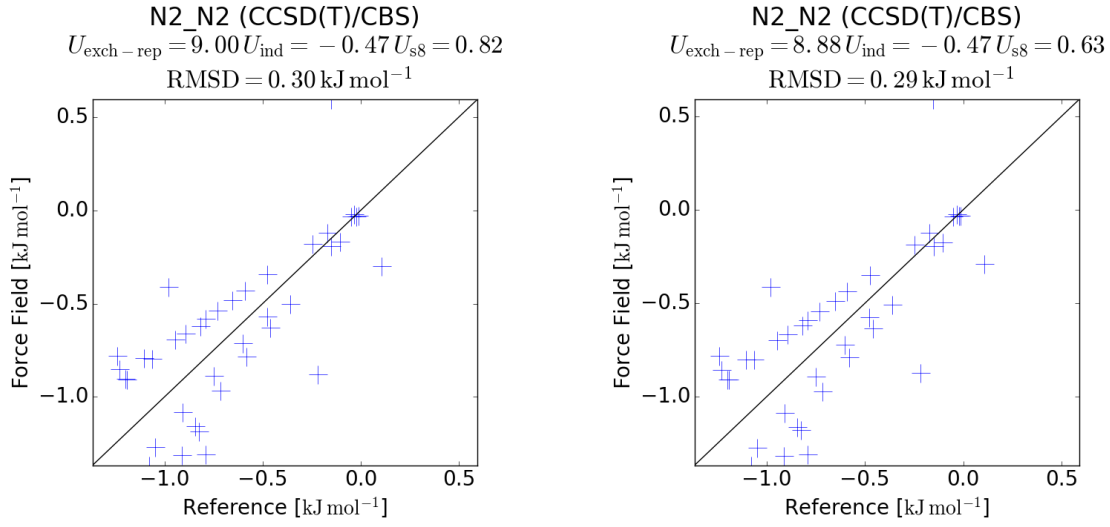


Figure 3.7: Comparison between the performance of the MEDFFs with DP = 20% with B3LYP/aug-cc-pVTZ (left) and CCSD/aug-cc-pVTZ (right) monomer densities.

External Validation

In this paragraph, simulations based on the derived force fields will be compared to experimental results for N₂ fluids. First the second virial coefficient of N₂, $B_2(T)$, will be studied. This quantity appears in the virial expansion for a non-ideal fluid:

$$P = \frac{Nk_B T}{V} \left[1 + \frac{N}{V} B_2(T) + \left(\frac{N}{V} \right)^2 B_3(T) + \dots \right] \quad (3.3)$$

In this formula, P is the pressure, N the number of fluid molecules, k_B the Boltzmann constant, T the temperature and V the volume. Withholding only the first term in this expression yields the ideal gas law, while higher order terms account for the interactions between molecules. $B_2(T)$ thus represents a first order correction, approximating the non-ideality of the fluid. Second virial coefficients are especially interesting because they can be related directly to dimer interaction energies (*i.e.* no many-body effects (with body referring to monomer) are taken into account). When the monomers are rigid, it follows that:⁸⁰

$$B_2(T) = 2\pi \int [1 - \langle \exp(-\beta E_{\text{inter}}(r)) \rangle] r^2 dr \quad (3.4)$$

Herein, E_{inter} is the dimer interaction energy, r the intermolecular separation and $\beta = \frac{1}{k_B T}$. $\langle \dots \rangle$ represents the average over all possible orientations of the two monomers. In Figure 3.8 simulated values for the second virial coefficient are compared to experimental data.⁸¹ The radial integral in Eq. (3.4) was calculated numerically by the trapezoidal rule and for the orientational average 10 000 randomly selected dimer configurations were considered.

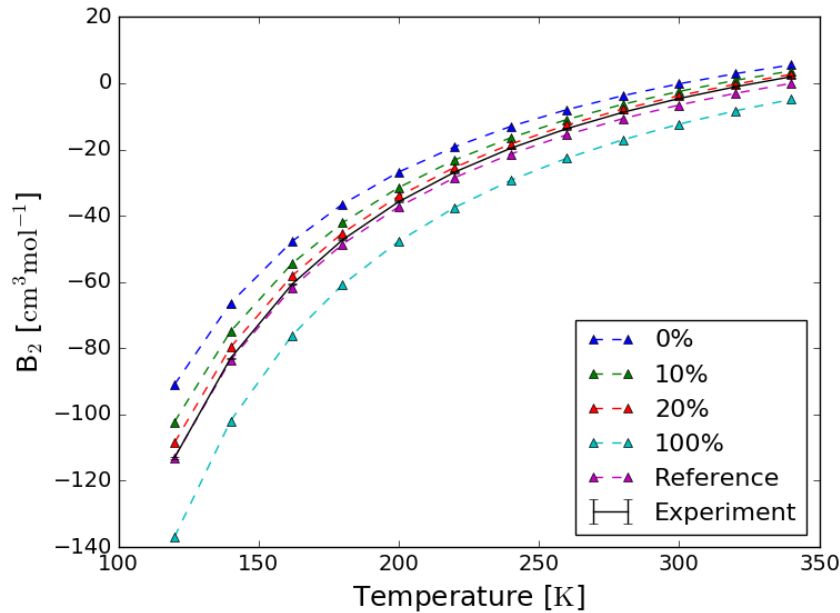


Figure 3.8: Simulations for the second virial coefficient of N₂ (using MEDFFs with several parameter sets) are compared to experimental values.⁸¹

Figure 3.8 shows that relatively small changes in interaction parameters (e.g. DP = 10% instead of DP = 0%) can result in a substantial change in the second virial coefficient. The best results for $B_2(T)$ were found for DP = 20%. For lower values, the simulated curve is situated above the experimental profile implying that the molecules are underbound. Indeed, inspecting (Eq. 3.4), underestimations of E_{inter} give rise to second virial coefficients that are too high. For DP = 100% on the other hand, N₂ complexes are overbound. Indeed, as was established in Figure 3.2, purely SAPT interaction energies tend to overbind N₂ dimers. The reference interaction parameters for the S66x8 database also perform remarkably well.

As a second part of the external validation, vapor-liquid coexistence curves were considered. These display the density of gas and liquid phases in thermodynamic equilibrium at a certain temperature. Vapor-liquid equilibria are especially important because adsorbate gases can condense upon adsorption in a nanoporous host. In order to correctly model this behaviour, an accurate reproduction of VLCCs is hence indispensable. Therefore, VLCCs were calculated by Monte Carlo simulations in the Gibbs ensemble via the RASPA program.⁸² In these simulations, the considered system consists of two subsystems exchanging molecules, volume and energy, thus equilibrating chemical potential, pressure and temperature. For the complete system, volume, particle number and temperature remain fixed. When equilibrium is reached, the reservoir containing the most molecules corresponds to the liquid phase while the other corresponds to the gas phase. By calculating the densities of both these phases, one constructs the VLCC. Figure 3.9 compares the simulated VLCCs for N₂ to experimental values.⁸³

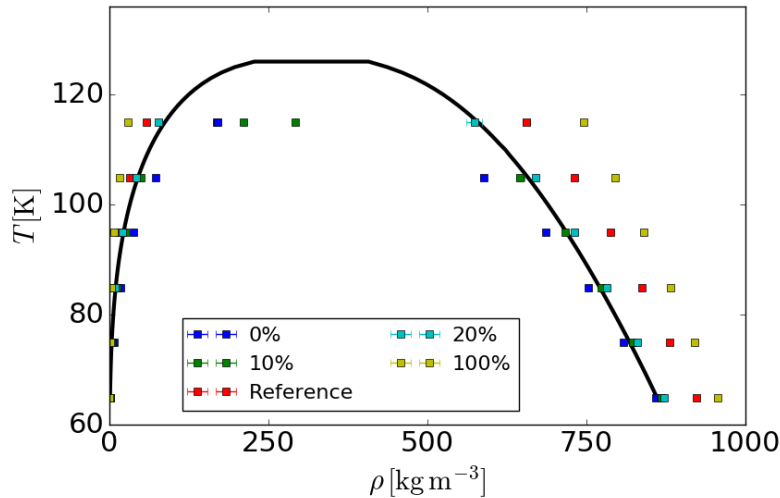


Figure 3.9: Simulations for the vapour-liquid coexistence curve of N₂ (using MEDFFs with several parameter sets) are compared to experimental values⁸³ (black curve).

Determination of the VLCC close to the critical point is both empirically and computationally a demanding task. This explains why the black curve, containing experimental values, is flattened near the top and why simulations were only executed up to 115 K. Closer to the critical point simulations tend to break down. For DPs 0% and 10%, breakdown already occurs at 115 K implying that for these DPs the critical point is located at a lower temperature than for the other MEDFF models. The best results are obtained for DP = 20%. Densities of gas and liquid phases are reproduced and this for temperatures up to 115 K. For higher deviation percentages, the force field becomes too attractive leading to an overestimation of the density in the liquid phase and an underestimation for the gas phase density. Indeed, the phase with the highest density will attract even more molecules due to the overestimation of the interaction energy. Even though the reference parameters performed relatively well for virial coefficient simulations, the reproduction of VLCCs with this parameter set is unsatisfactory.

3.2 CO₂

3.2.1 Force Field Construction

For CO₂ the same procedure is followed as for N₂. The MBIS partitioning results for CO₂ are displayed in Table 3.4. A charge transfer from the carbon atom to both oxygen atoms of about half the electron charge is observed. This charge transfer is slightly stronger in the CCSD/aug-cc-pVTZ LoT. One concludes that the bonds in this molecule are highly polar while the molecule itself is non-polar. In the calculations, the CO₂ monomer was kept linear with experimental C-O bond lengths of 1.162 Å.⁸⁴ Due to numerical integration, small differences between the charge parameters for both O atoms are found but these are of the order of 0.001 a.u.

Atom	B3LYP/aug-cc-pVTZ				CCSD/aug-cc-pVTZ			
	q _c	q _v	σ _v	q _{tot}	q _c	q _v	σ _v	q _{tot}
C	4.34	-3.37	0.45	0.97	4.34	-3.33	0.46	1.00
O	6.38	-6.87	0.39	-0.48	6.38	-6.89	0.39	-0.50
O	6.38	-6.87	0.39	-0.48	6.38	-6.89	0.39	-0.50

Table 3.4: MBIS parameters (in a.u.) for the MEDFF of CO₂ in the B3LYP/aug-cc-pVTZ and CCSD/aug-cc-pVTZ level of theory.

Since CO₂ is a linear molecule, just like N₂, the same dimer configurations are important for the scanning of the PES. However, literature now dictates that the T and Z60 are the most stable configurations.⁸⁵ The L configuration on the other hand remains unstable and is not taken into account. For the intermolecular distance, the same DMs as before were used to build up the set of data points. Figure 3.10 shows the dissociation profiles for the considered configurations. The H configuration is non-bonding and will therefore be excluded from the dataset. Indeed, a simple electrostatics reasoning shows that the equal charges in both O and C atoms will repel each other, thus making the H configuration unfavorable. A similar reasoning applies to the L configuration. As was the case for N₂, SAPT energies are more attractive. An important difference on the other hand, is that CO₂ dimers are more strongly bound than N₂ dimers.

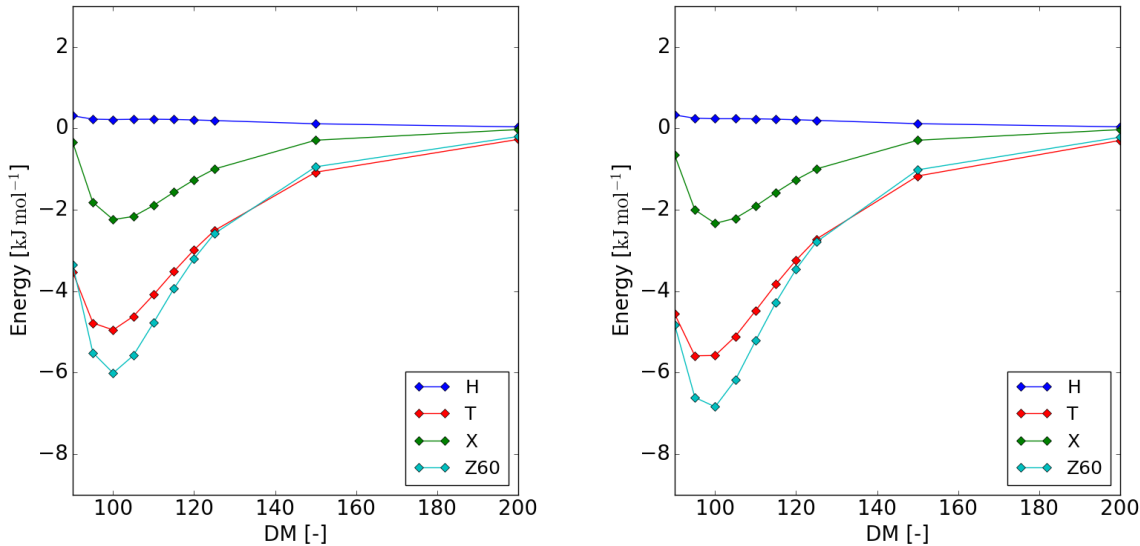


Figure 3.10: Ab initio calculated dissociation profiles for different configurations of the CO₂ dimer in the CCSD(T)/aug-cc-pVTZ (left) and SAPT/aug-cc-pVTZ (right) level of theory.

The next step in the force field construction consists of a σ_{pr} scan of the RMSD_{CCSD(T)} and RMSD_U errors. These are displayed in Figure 3.11. Both curves have a similar shape as was the case for N₂ but now RMSDs are typically larger for CCSD/aug-cc-pVTZ monomer densities. Therefore B3LYP/aug-cc-pVTZ densities are preferred for the construction of MEDFFs for CO₂.

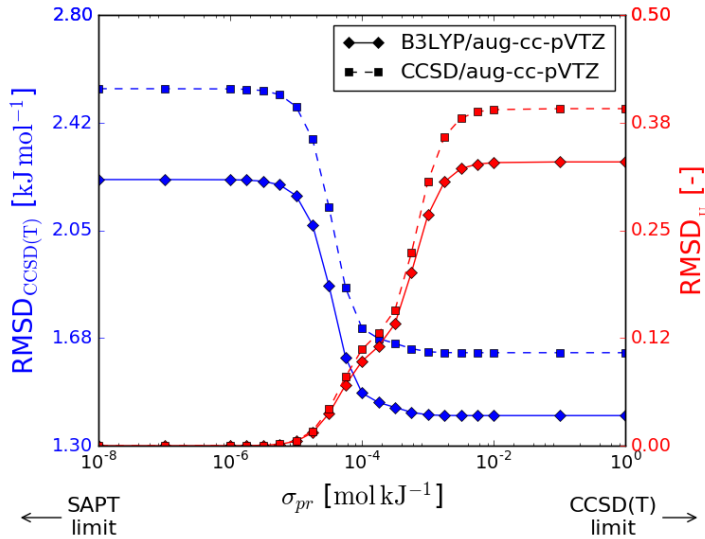


Figure 3.11: Influence of the regularisation strength on RMSD_{CCSD(T)} and RMSD_U.

Because RMSD_U can reach values up to 40%, σ_{pr} should be low enough for the interaction parameters to retain their physical significance. Therefore the same values as for N₂ were chosen and the corresponding interaction parameters are displayed in Table 3.5.

DP	B3LYP/aug-cc-pVTZ				CCSD/aug-cc-pVTZ			
	σ_{pr}	$U_{\text{exch-rep}}$	U_{ind}	U_{s8}	σ_{pr}	$U_{\text{exch-rep}}$	U_{ind}	U_{s8}
0%	∞	9.452	-0.895	2.317	∞	9.497	-0.856	2.258
10%	9.869	8.115	-0.913	1.549	9.794	8.049	-0.886	1.409
20%	6.975	7.926	-0.917	1.548	6.936	7.840	-0.890	1.409
100%	0.000	6.970	-0.934	1.604	0.000	6.781	-0.909	1.462

Table 3.5: Regularisation parameters (in 10^{-5} mol kJ⁻¹) and corresponding interaction parameters (in a.u.) for the MEDFF of CO₂.

In Figure 3.11 the influence of σ_{pr} on the interaction parameters is evaluated. As was the case for N₂, $U_{\text{exch-rep}}$ and U_{ind} behave alike, but now the SAPT limit values are lower than the CCSD(T) limit values. For U_{s8} an inverted profile was found as well. This implies that for increasing DPs the force field will initially experience two opposing influences (both U_{s8} and the sum of $U_{\text{exch-rep}}$ and U_{ind} decrease, the former making the force field more repulsive while the latter has the opposite effect). Once σ_{pr} is smaller than 10^{-4} mol kJ⁻¹, U_{s8} starts to increase, rendering the force field slightly more repulsive. However, the force field is expected to be more attractive in the SAPT limit than in the CCSD(T) limit because SAPT energies are typically more attractive than CCSD(T) energies. Indeed, an MD was found between the MEDFFs in the SAPT and CCSD(T) limit, confirming that the force field becomes more attractive when the DP is increased.

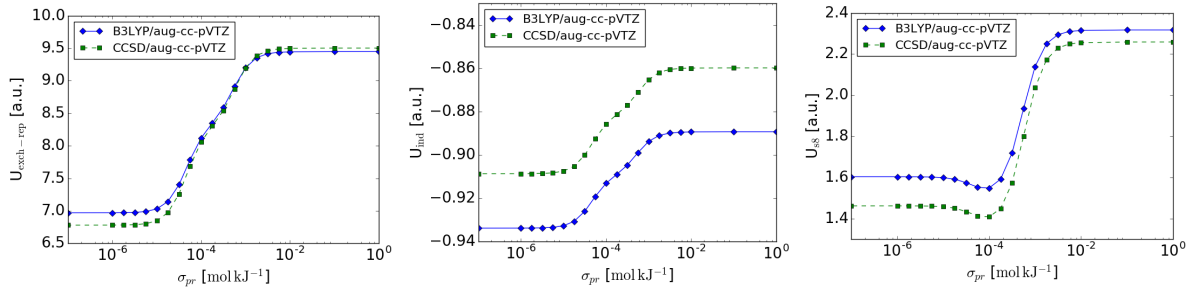


Figure 3.12: Influence of the regularisation strength on the interaction parameters in both levels of theory for the monomer densities.

3.2.2 Charge Rescaling

Figure 3.13 compares *ab initio* CCSD(T) and force field dissociation profiles for the MEDFFs with DP = 20%. The interaction energies for T and Z60 configurations are overestimated gravely while the X configuration is underbound. As Figure 3.11 already showed, the CCSD/aug-cc-pVTZ LoT performs worse than B3LYP/aug-cc-pVTZ. Relative errors are also larger than for N₂ and therefore the quality of the force field is expected to be questionable.

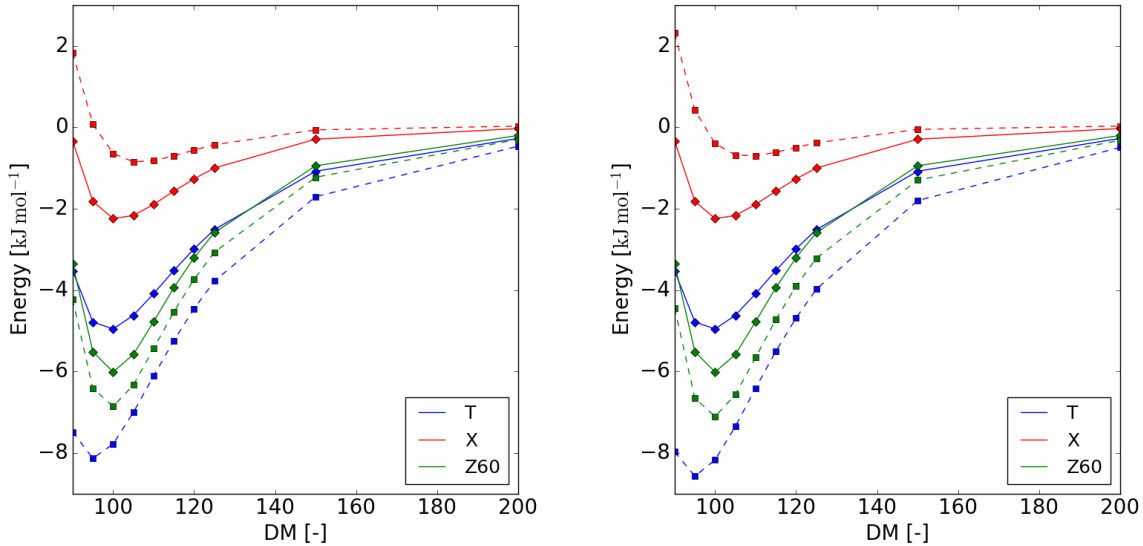


Figure 3.13: Comparison between *ab initio* calculated CCSD(T)/aug-cc-pVTZ dissociation profiles for CO₂ (\diamond , full line) and the MEDFF approximation hereof (\square , dashed line) with DP = 20% and B3LYP/aug-cc-pVTZ (left) or CCSD/aug-cc-pVTZ (right) monomer densities.

In Figure 3.14 the different MEDFF contributions (for DP = 20% and B3LYP/aug-cc-pVTZ densities) are compared to *ab initio* SAPT data. The discrepancies in the force field clearly originate from the electrostatics contribution. Not only is the RMSD the highest of all contributions, but even more important is the fact that the slope of the data points is not parallel to the bisector, indicating severe problems. As was mentioned in the second chapter, the force field approximation for the electrostatics contribution contains no interaction parameter and is

thus solely determined by the MBIS model density. The quality of this model is thus verified immediately by comparing *ab initio* and force field electrostatics. Since this correspondence is not satisfying, one concludes that the approximations of the MBIS scheme are the cause for the disappointing force field performance.

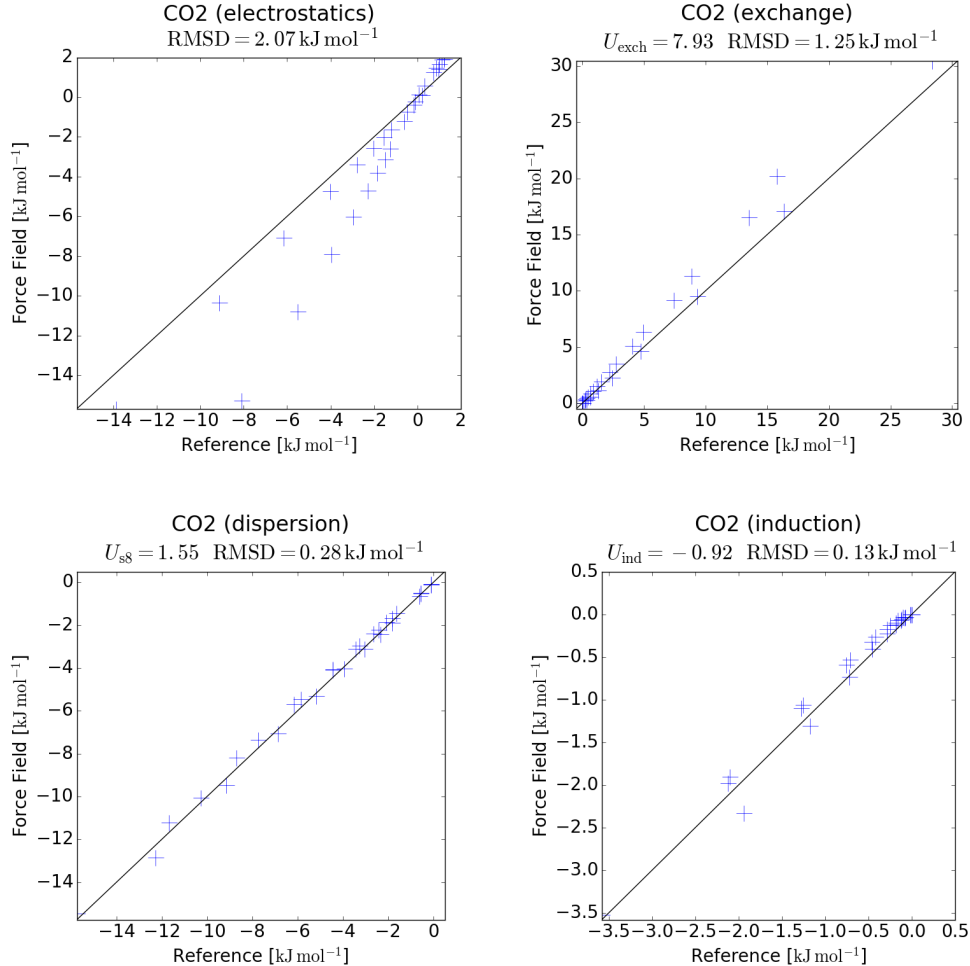


Figure 3.14: Comparison between *ab initio* calculated SAPT interaction energy contributions for CO₂ and the MEDFF approximation hereof. DP = 20% and B3LYP/aug-cc-pVTZ monomer densities were utilised.

The origin of the electrostatics problem can be understood from the highly polar C-O bonds in CO₂. Indeed, inspecting Figure 3.15, one observes that the *ab initio* electron density $\rho^e(\mathbf{r})$ differs to a certain extent from the MBIS model density $\tilde{\rho}^e(\mathbf{r})$ given by Eq. (2.2). Especially in the regions between C and O atoms, *i.e.* in the regions where the (relatively large) charge transfer occurs, the electron density is modeled inaccurately. Since only the model density is present in the force field, the effect of the charge transfer is thus underestimated. While the more correct *ab initio* electron density $\rho^e(\mathbf{r})$ is not applicable in a force field context (simple analytical expressions are necessary for computationally feasible simulations), it can tell which details are missing in $\tilde{\rho}^e(\mathbf{r})$. In the following, e superindices will be omitted because only electron densities are considered. the e superindex will be omitted in the following.

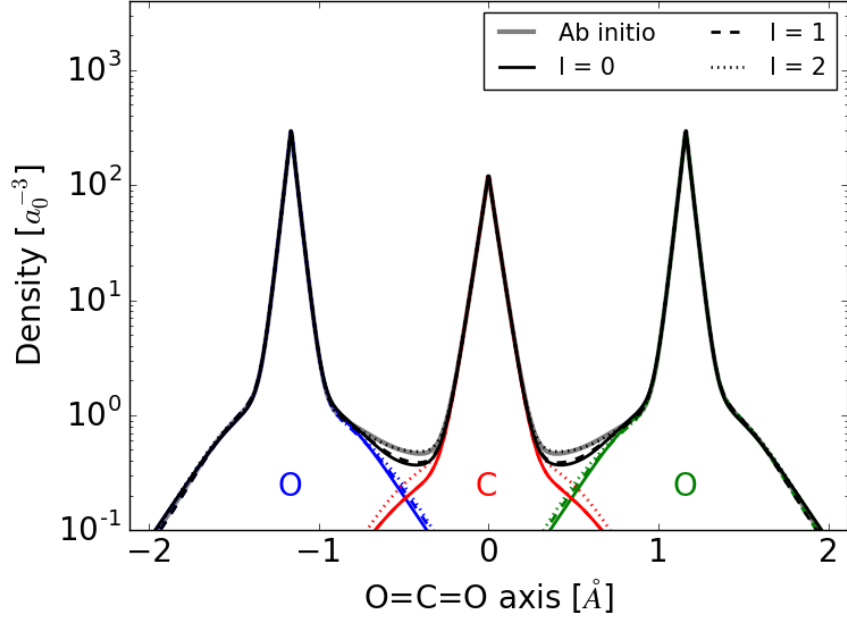


Figure 3.15: Comparison between the *ab initio* electron density, lower-order spherical approximations hereof and the MBIS model electron density along the axis of CO₂. The different atomic contributions are indicated as well.

In the following, the Atomic electron densities (Eq. 2.4) can be decomposed in spherical harmonics. If the axis directions are kept fixed and reference frames are solely discerned by their origin, one finds that:

$$\rho_A^A(\mathbf{r}) = \sum_{l=0}^{\infty} \sum_{m=-l}^l \rho_{A_{lm}}^A(r) Y_{lm}^A(\Omega) \quad (3.5)$$

where the superscripts denote the origin for \mathbf{r} (and thus the reference frame) and $Y_{lm}^A(\Omega)$ is the spherical harmonic with quantum numbers l and m . Herein, the spherically symmetric, lowest order ($l = 0$) contribution resembles the MBIS atomic model density of atom A, $\tilde{\rho}_A^A(\mathbf{r})$, to a good degree:

$$\rho_{A_{00}}^A(r) \approx \tilde{\rho}_A^A(\mathbf{r}) = \sum_{i=1}^{m_A} \frac{N_{A_i}}{\sigma_{A_i}^3 8\pi} \exp\left(-\frac{r}{\sigma_{A_i}}\right) \quad (3.6)$$

The electrostatics problem for CO₂ hence originates from the higher order terms. The influence of these terms on the electron density is also depicted in Figure 3.15. Corrections up to $l = 2$ are required to reproduce the *ab initio* electron density properly. Useful tools in this process are the atomic multipoles, the electrostatic multipoles calculated for the atomic densities $\rho_A^A(\mathbf{r})$. In their spherical form, they are defined as:

$$Q_{A_{lm}}^A = \sqrt{\frac{4\pi}{2l+1}} \int_0^\infty \rho_{A_{lm}}^A(r) r^{l+2} dr \quad (3.7)$$

By introducing the completeness relation for spherical harmonics the multipoles can be related

directly to their cartesian counterparts. E.g. the atomic spherical dipole moments ($l = 1$) are related to the atomic Cartesian dipole moment as follows:

$$\begin{aligned} Q_{A_1-1}^A &= \frac{1}{\sqrt{2}} \left(p_{A_x}^A - ip_{A_y}^A \right) \\ Q_{A_{10}}^A &= p_{A_z}^A \\ Q_{A_{11}}^A &= -\frac{1}{\sqrt{2}} \left(p_{A_x}^A + ip_{A_y}^A \right) \end{aligned} \quad (3.8)$$

In terms of atomic multipoles, including corrections up to $l = 2$ implies that atomic dipoles and quadrupoles should be included in the force field model in order to obtain a satisfactory reproduction of the electrostatic interaction energy.

A straightforward solution for the absence of higher order atomic multipoles in the force field is by simply introducing them to the model. This can be done by means of new variables, e.g. explicitly introducing atomic dipoles (which can be used to make the force field polarizable as well) or by introducing extra atom sites in the molecule (e.g. splitting up the O atoms into two or more separate atom sites) in order to simulate the atomic dipoles. However, both these solutions increase the number of DoFs strongly, thus slowing down force field evaluation in molecular simulations. Therefore an approach similar to the one proposed by Hadad et al.⁸⁶ is followed. The atomic multipoles all contribute to the molecular multipoles. Since higher order atomic multipoles are missing in the original force field, the molecular multipoles are different from their *ab initio* values. E.g. the molecular quadrupole moment is built up by an atomic charge, dipole and quadrupole contribution. In the force field only the charge contribution is present. A possible way to correct for the atomic dipole and quadrupole contributions is therefore to rescale the atomic charges to reproduce the molecular quadrupole moment.

In order to determine the influence of atomic multipoles on their molecular counterparts, it is important to know how multipoles transform when the reference frame is translated to a new origin. By inspecting Figure 3.16, one finds that:

$$\begin{aligned} \rho_A^{B'}(\mathbf{r}') &= \rho_A^B(\mathbf{r}) \\ \text{with } \mathbf{r}' &= \mathbf{r} - \mathbf{BB}' \end{aligned} \quad (3.9)$$

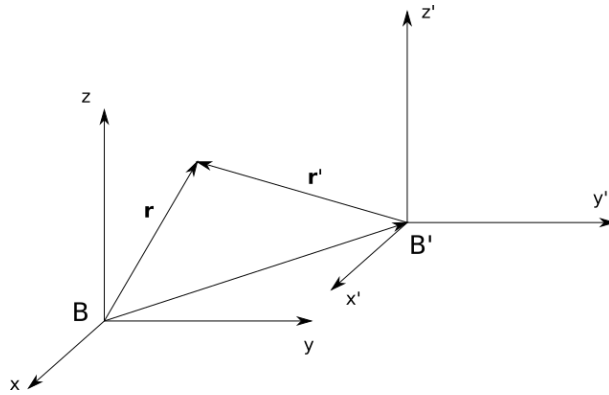


Figure 3.16: Clarifying figure concerning the influence of a translation of the origin.

The influence of a translation of the origin on the lowest Cartesian multipoles of a charge distribution can hence be calculated as follows:

$$\begin{aligned}
 q^B &= \int \rho^B(\mathbf{r}) d\mathbf{r} = \int \rho^{B'}(\mathbf{r}') d\mathbf{r}' = q^{B'} \\
 \mathbf{p}^B &= \int \rho^B(\mathbf{r}) \mathbf{r} d\mathbf{r} = \int \rho^{B'}(\mathbf{r}') (\mathbf{r}' + \mathbf{BB}') d\mathbf{r}' = \mathbf{p}^{B'} + q^{B'} \mathbf{BB}' \\
 \mathbf{Q}^B &= \int \rho^B(\mathbf{r}) \left[\mathbf{r} \otimes \mathbf{r} - \frac{r^2}{3} \mathbf{I} \right] d\mathbf{r} \\
 &= \int \rho^{B'}(\mathbf{r}') \left[(\mathbf{r}' + \mathbf{BB}') \otimes (\mathbf{r}' + \mathbf{BB}') - \frac{1}{3} (\mathbf{r}' + \mathbf{BB}') \cdot (\mathbf{r}' + \mathbf{BB}') \mathbf{I} \right] d\mathbf{r}' \\
 &= \mathbf{Q}^{B'} + \mathbf{BB}' \otimes \mathbf{p}^{B'} + \mathbf{p}^{B'} \otimes \mathbf{BB}' - \frac{2}{3} (\mathbf{BB}' \cdot \mathbf{p}^{B'}) \mathbf{I} \\
 &\quad + \left(\mathbf{BB}' \otimes \mathbf{BB}' - \frac{1}{3} (\mathbf{BB}' \cdot \mathbf{BB}') \mathbf{I} \right) q^{B'}
 \end{aligned} \tag{3.10}$$

Charges are clearly the same in each reference frame (and we thus may omit the superscript index) while for dipole and quadrupole moments transformation laws apply. These transformation properties allow us to calculate the molecular multipoles (in the reference frame of Figure 3.17) from the atomic multipoles.

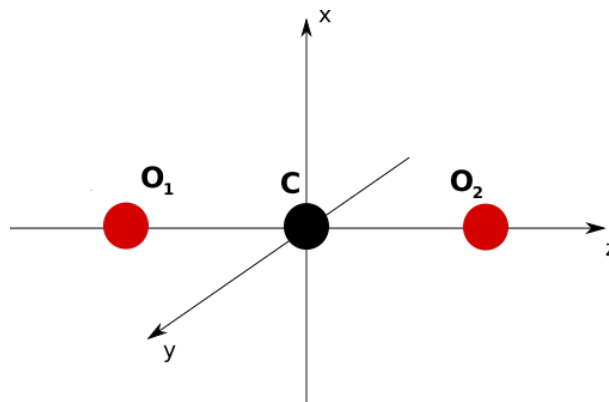


Figure 3.17: Reference frame used in the multipole analysis of CO₂.

Indeed, for the total charge we find:

$$q = \int \rho^C(\mathbf{r}) d\mathbf{r} = \int [\rho_C^C(\mathbf{r}) + \rho_{O_1}^C(\mathbf{r}) + \rho_{O_2}^C(\mathbf{r})] d\mathbf{r} = q_C + q_{O_1} + q_{O_2} = 0 \quad (3.11)$$

For the molecular dipole, the correct transformation laws should be applied:

$$\begin{aligned} \mathbf{p}^C &= \int [\rho_C^C(\mathbf{r}) + \rho_{O_1}^C(\mathbf{r}) + \rho_{O_2}^C(\mathbf{r})] \mathbf{r} d\mathbf{r} \\ &= \mathbf{p}_C^C + \mathbf{p}_{O_1}^{O_1} + q_{O_1} \mathbf{CO}_1 + \mathbf{p}_{O_2}^{O_2} + q_{O_2} \mathbf{CO}_2 = 0 \end{aligned} \quad (3.12)$$

For the molecular quadrupole moment, one calculates that:

$$\begin{aligned} \mathbf{Q}^C &= \int [\rho_C^C(\mathbf{r}) + \rho_{O_1}^C(\mathbf{r}) + \rho_{O_2}^C(\mathbf{r})] \left[\mathbf{r} \otimes \mathbf{r} - \frac{r^2}{3} \mathbf{I} \right] d\mathbf{r} = \mathbf{Q}_C^C + \mathbf{Q}_{O_1}^C + \mathbf{Q}_{O_2}^C \\ \mathbf{Q}_{O_1}^C &= \mathbf{Q}_{O_1}^{O_1} + \mathbf{CO}_1 \otimes \mathbf{p}_{O_1}^{O_1} + \mathbf{p}_{O_1}^{O_1} \otimes \mathbf{CO}_1 - \frac{2}{3} (\mathbf{CO}_1 \cdot \mathbf{p}_{O_1}^{O_1}) \mathbf{I} \\ &\quad + \left(\mathbf{CO}_1 \otimes \mathbf{CO}_1 - \frac{1}{3} (\mathbf{CO}_1 \cdot \mathbf{CO}_1) \mathbf{I} \right) q_{O_1} \\ \mathbf{Q}_{O_2}^C &= \mathbf{Q}_{O_2}^{O_2} + \mathbf{CO}_2 \otimes \mathbf{p}_{O_2}^{O_2} + \mathbf{p}_{O_2}^{O_2} \otimes \mathbf{CO}_2 - \frac{2}{3} (\mathbf{CO}_2 \cdot \mathbf{p}_{O_2}^{O_2}) \mathbf{I} \\ &\quad + \left(\mathbf{CO}_2 \otimes \mathbf{CO}_2 - \frac{1}{3} (\mathbf{CO}_2 \cdot \mathbf{CO}_2) \mathbf{I} \right) q_{O_2} \end{aligned} \quad (3.13)$$

An interesting feature of this analysis is that it is also possible to decompose the molecular multipoles into different atomic multipole contributions, e.g. the molecular dipole moment can be decomposed in a contribution from atomic charges $q_{O_1} \mathbf{CO}_1 + q_{O_2} \mathbf{CO}_2$ and a contribution from atomic dipoles $\mathbf{p}_C^C + \mathbf{p}_{O_1}^{O_1} + \mathbf{p}_{O_2}^{O_2}$. For the molecular quadrupole moment an atomic charge, atomic dipole and an atomic quadrupole contribution are present:

$$\begin{aligned} \mathbf{Q}_{\text{charge}}^C &= \sum_{X=O_1, O_2, C} q_X \left(\mathbf{CX} \otimes \mathbf{CX} - \frac{1}{3} \mathbf{CX}^2 \mathbf{I} \right) \\ \mathbf{Q}_{\text{dipole}}^C &= \sum_{X=O_1, O_2, C} \left(\mathbf{CX} \otimes \mathbf{p}_X^X + \mathbf{p}_X^X \otimes \mathbf{CX} - \frac{2}{3} \mathbf{CX} \cdot \mathbf{p}_X^X \mathbf{I} \right) \\ \mathbf{Q}_{\text{quadrupole}}^C &= \sum_{X=O_1, O_2, C} \mathbf{Q}_X^X \end{aligned} \quad (3.14)$$

The quadrupole moment tensor is traceless and symmetric, normally having five independent components. Due to the symmetry in CO₂ however, the tensor is diagonal with equal xx and yy components. Therefore, the quadrupole moment tensor is completely determined by only one component for CO₂, the zz component. Hence, the size of each of the atomic multipole contributions to this component is a measure for the importance of these atomic multipoles in the electrostatic interaction. Table 3.6 shows the atomic multipole contributions to Q_{zz}^C for both levels of theory for which CO₂ monomer densities were calculated. One concludes that especially the atomic dipoles have an additional influence on the quadrupole moment. Their absence in the force thus leads to the disappointing results for the electrostatics as observed in Figure 3.14.

	$Q_{\text{charge}_{zz}}^C$	$Q_{\text{dipole}_{zz}}^C$	$Q_{\text{quadrupole}_{zz}}^C$	Q_{zz}^C
B3LYP/aug-cc-pVTZ	-4.181	1.476	-0.299	-3.003
CCSD/aug-cc-pVTZ	-4.344	1.679	-0.291	-2.956

Table 3.6: Atomic multipole contributions to the zz component of the molecular quadrupole moment (in DÅ).

Not only does this multipole analysis gives us insight in where the force field fails, it also gives us the possibility to solve the problem. By rescaling the total MBIS charges so that they exactly reproduce the *ab initio* molecular quadrupole moment, the effects of atomic dipoles and quadrupoles (and thus of the large charge transfer in CO₂) will be incorporated in the force field model. This is accomplished by only altering the core charges of all atoms while keeping the valence charges fixed. If valence charges were altered, other force field contributions would change as well (e.g. exchange-repulsion and induction depend on the valence charges), an unwanted side effect. The charge rescaling operation can thus be summarised as:

$$\begin{aligned} x &= \frac{Q_{zz}^C}{Q_{\text{charge}_{zz}}^C} \\ q' &= xq \\ q'_v &= q_v \\ q'_c &= xq_c + (x - 1)q_v \end{aligned} \tag{3.15}$$

Table 3.7 displays the rescaled MBIS parameters for CO₂. The new charges are about 75% their value before scaling. This decrease in charge is due to the repulsion between the quadrupole moments of the monomers, which are now included in the force field by means of adapted core charges.

Atom	B3LYP/aug-cc-pVTZ				CCSD/aug-cc-pVTZ			
	q _c	q _v	σ _v	q _{tot}	q _c	q _v	σ _v	q _{tot}
C	4.07	-3.37	0.45	0.69	4.02	-3.33	0.46	0.68
O	6.52	-6.87	0.39	-0.35	6.54	-6.89	0.39	-0.34
O	6.52	-6.87	0.39	-0.35	6.54	-6.89	0.39	-0.34

Table 3.7: Rescaled MBIS parameters (in a.u.) for the MEDFF of CO₂ in the B3LYP/aug-cc-pVTZ and CCSD/aug-cc-pVTZ level of theory.

The influence of the charge rescaling on the reproduction of *ab initio* electrostatics is verified in Figure 3.18. The RMSDs are almost halved when compared to Figure 3.14 and the problematic slope that was observed earlier is corrected for completely. This is the case in both levels of theory for the monomer densities.

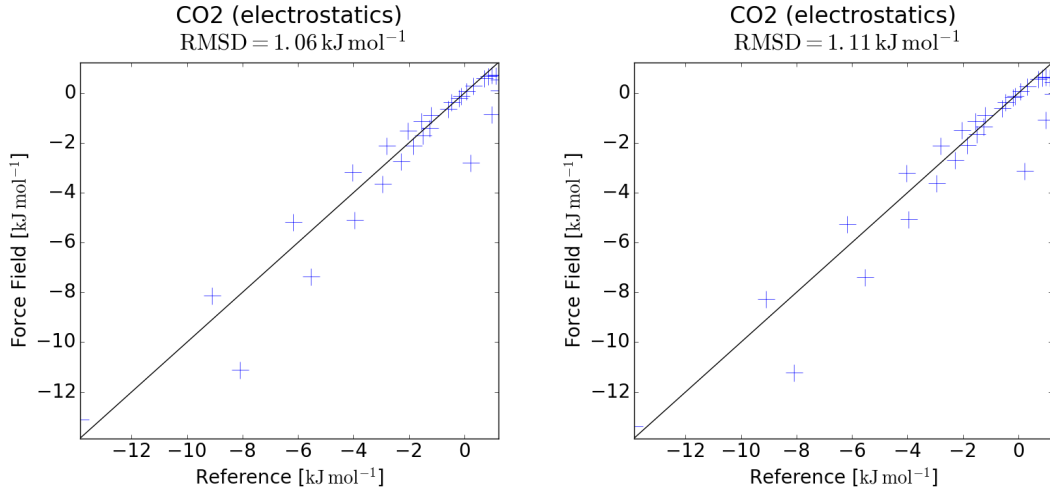


Figure 3.18: Influence of the charge rescaling procedure on the reproduction of the electrostatics contribution to the dimer interaction energy for B3LYP/aug-cc-pVTZ (left) and CCSD/aug-cc-pVTZ (right) monomer densities.

3.2.3 Validation

3.2.3.1 Internal Validation

After rescaling the charges, the interaction parameters should be re-determined. Indeed, in the original fit, other force field contributions will have tried to compensate the discrepancies in the electrostatics part, leading to erroneous results for the interaction parameters. First, a σ_{pr} scan of $\text{RMSD}_{\text{CCSD(T)}}$ and RMSD_U is studied (Figure 3.19). The typical shape that was already found for N₂ and CO₂ (with unscaled charges) is found again. However comparing Figures 3.3 and 3.11 with the scan below, the RMSD_U values are significantly smaller here. Therefore, ideal deviation percentages will be smaller for CO₂ with scaled charges than they were before.

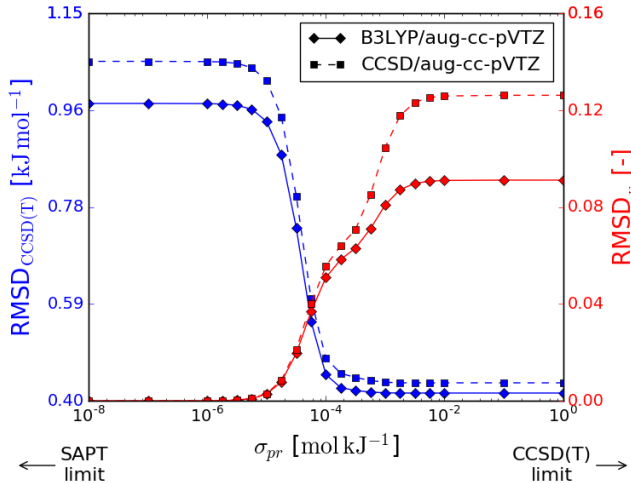


Figure 3.19: Influence of the regularisation strength on $\text{RMSD}_{\text{CCSD(T)}}$ and RMSD_U .

In Table 3.8 the newly fitted interaction parameters for DPs 0%, 10%, 20% and 100% are displayed. Comparing them with Table 3.5, the range is remarkably smaller in the case of rescaled charges. This is in correspondence with the observed curve for RMSD_U in Figure 3.19.

DP	B3LYP/aug-cc-pVTZ				CCSD/aug-cc-pVTZ			
	σ_{pr}	$U_{\text{exch-rep}}$	U_{ind}	U_{s8}	σ_{pr}	$U_{\text{exch-rep}}$	U_{ind}	U_{s8}
0%	∞	7.436	-0.930	1.374	∞	7.190	-0.901	1.155
10%	9.129	7.524	-0.924	1.557	9.436	7.380	-0.898	1.417
20%	6.741	7.445	-0.925	1.565	7.068	7.303	-0.899	1.425
100%	0.000	6.970	-0.934	1.604	0.000	6.781	-0.909	1.462

Table 3.8: Regularisation parameters (in 10^{-5} mol kJ⁻¹) and corresponding interaction parameters (in a.u.) for the MEDFF of CO₂ with scaled charges.

Figure 3.20 shows how the interaction parameters change in function of σ_{pr} . The profiles are more similar to those for N₂ than the ones in Figure 3.12. However, in contrast to Figure 3.3 both $U_{\text{exch-rep}}$ and U_{ind} are higher in the CCSD(T) limit than in the SAPT limit. This implies that the force field will certainly be more attractive in the SAPT limit than in the CCSD(T) limit. Indeed, for increasing deviation percentage the force field will first experience two opposing influences (*i.e.* it becomes more attractive because U_{s8} increases while on the other hand it becomes more repulsive because the sum of $U_{\text{exch-rep}}$ and U_{ind} increases) after which it becomes more attractive than it was in the CCSD(T) because U_{s8} still increases and the sum of $U_{\text{exch-rep}}$ and U_{ind} decreases to a level below the CCSD(T) limit.

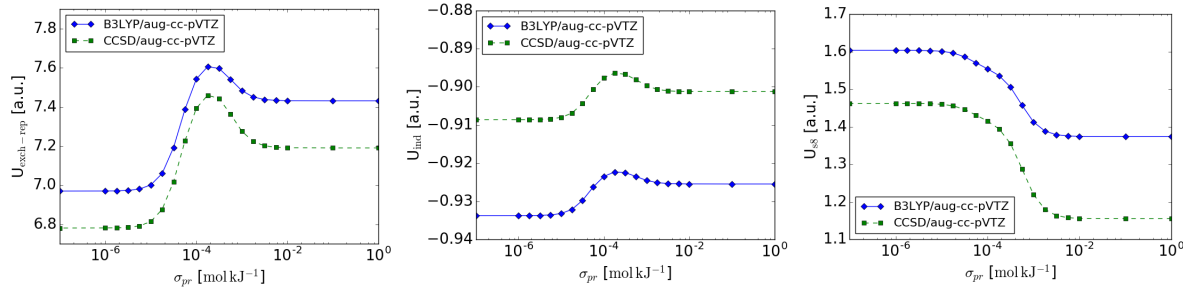


Figure 3.20: Influence of the regularisation strength on the interaction parameters in both levels of theory for the monomer densities.

In Figure 3.21 the reproduction of ab initio CCSD(T) profiles is verified. An impressive improvement is found when comparing with Figure 3.13. The force field overbinds T and X configurations in both levels of theory only slightly. The Z60 configuration, on the other hand, is underbound. Comparing the RMSDs for both levels of theory, B3LYP/aug-cc-pVTZ densities perform slightly better than CCSD/aug-cc-pVTZ densities. The relative errors for the MEDFF for N₂ are also larger than those for CO₂. This raises the question whether charge rescaling method could also have been applied to N₂. However, as Table 3.1 shows, the atoms in N₂ do not have a charge to rescale and the procedure is thus not applicable.

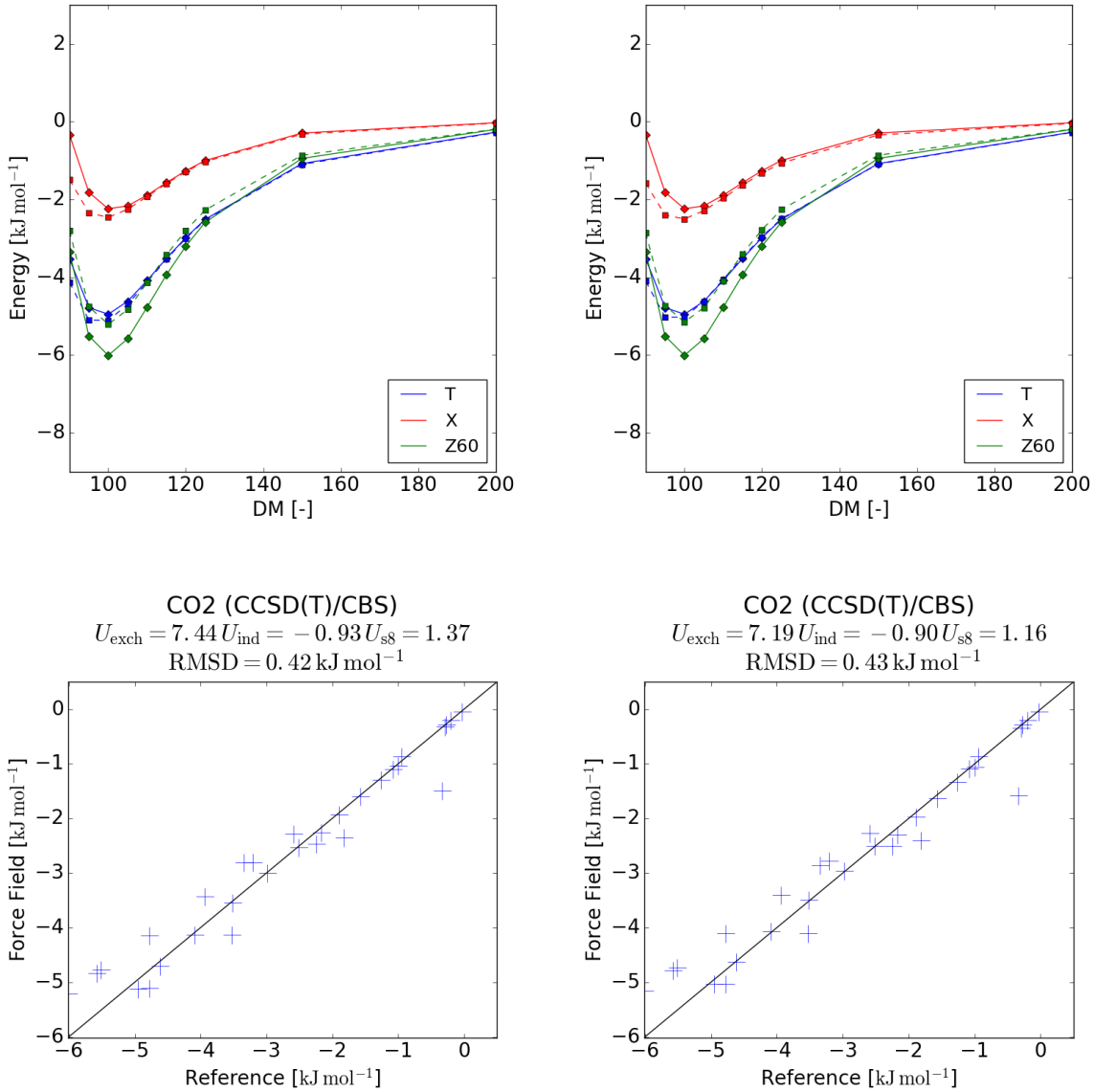


Figure 3.21: Comparison between *ab initio* calculated CCSD(T)/aug-cc-pVTZ dissociation profiles for CO₂ (\diamond) and the MEDFF approximation hereof (\square) with scaled charges, DP = 0% and B3LYP/aug-cc-pVTZ (left) or CCSD/aug-cc-pVTZ (right) monomer densities.

Reproduction of separate force field contributions is examined in Figure 3.22. The improvements in the electrostatics contribution were already discussed before but also the other force field contributions experience substantial corrections because they do not have to compensate erroneous electrostatics. Only the dispersion contribution performs slightly worse with scaled charges.

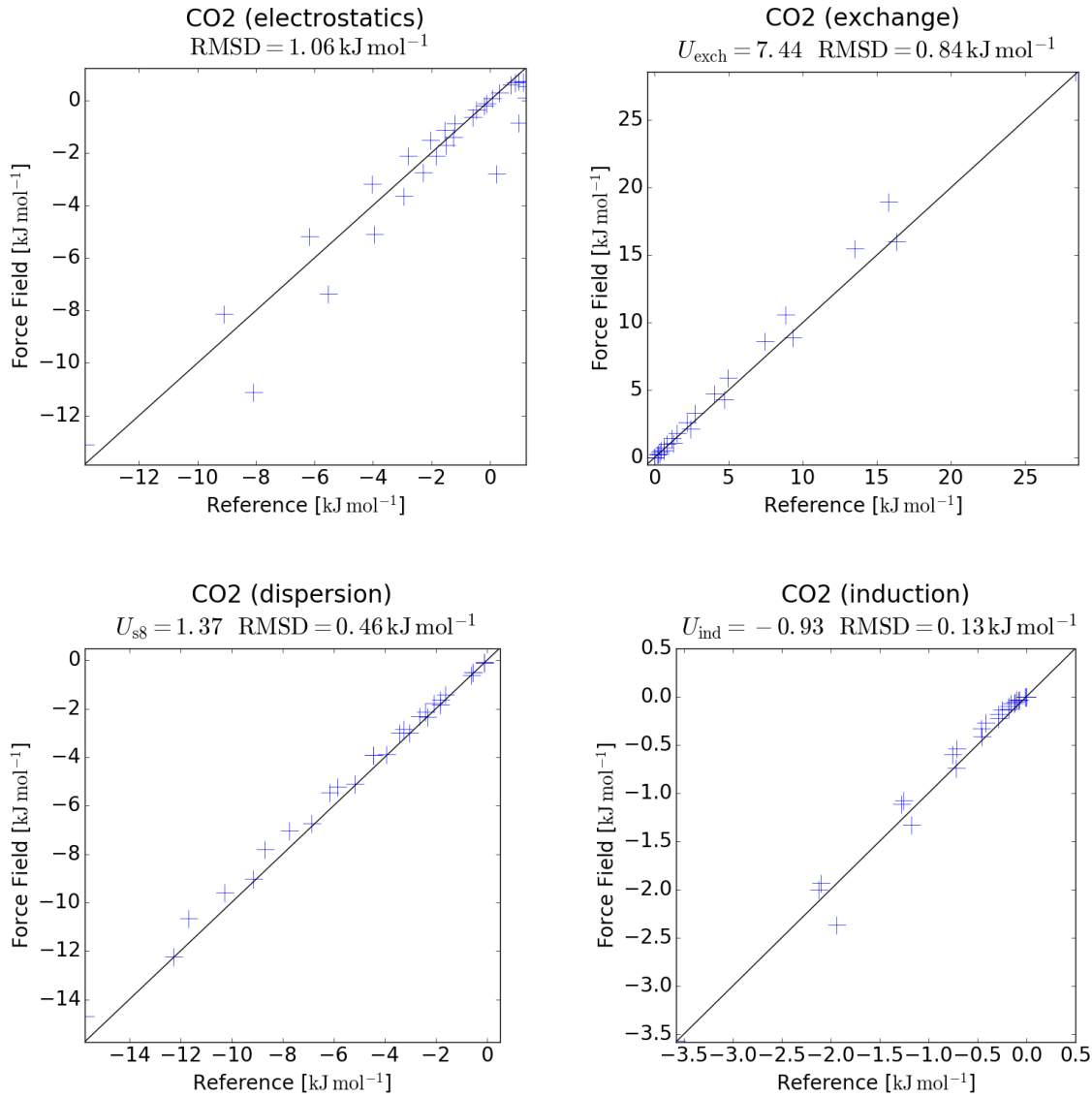


Figure 3.22: Comparison between *ab initio* calculated SAPT interaction energy contributions for CO₂ and the MEDFF approximation hereof. DP = 0% and B3LYP/aug-cc-pVTZ monomer densities were utilised.

In Table 3.9 reference values for the interaction parameters in the limiting cases DP = 0% and DP = 100 % are compared to the corresponding values for CO₂ with rescaled charge parameters. Both exchange-repulsion and induction parameters are comparable to the corresponding reference values. For U_{s8} on the other hand, high deviations are found. These could originate from the fact that CO₂ is not a dispersion dominated complex. Hence, the universal parameters only apply to a lesser extent here.

3.2.3.2 External Validation

Second virial coefficients were simulated for CO₂, using MEDFFs with scaled charges, B3LYP/aug-cc-pVTZ monomer densities and different DPs. For DP = 20% a simulation with unscaled

	B3LYP/aug-cc-pVTZ			CCSD/aug-cc-pVTZ			Reference			
	DP	$U_{\text{exch-rep}}$	U_{ind}	U_{s8}	$U_{\text{exch-rep}}$	U_{ind}	U_{s8}	$U_{\text{exch-rep}}$	U_{ind}	U_{s8}
0%	0%	7.44	-0.93	1.37	7.19	-0.90	1.16	8.27	-0.86	0.48
100%	100%	6.97	-0.93	1.60	6.78	-0.91	1.46	8.13	-0.87	0.57

Table 3.9: Comparison between the interaction parameters (in a.u.) of the MEDFF for CO₂ and the corresponding reference values for the S66x8 database.

charges was added as well. The force field with DP = 0% performs best while higher deviation percentages are overbound. This is in correspondence with what was established in Figure 3.20: the higher the DP, the stronger the interaction. Reference values for the interaction parameters on the other hand, are underbound greatly. Because the repulsive interaction between the molecular quadrupoles is missing in the MEDFF with unscaled charges, complexes are strongly overbound here.

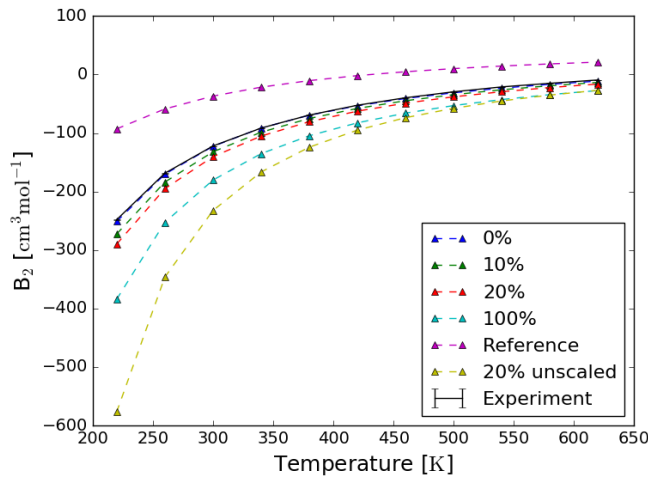


Figure 3.23: Simulations for the second virial coefficient of CO₂ (using MEDFFs with several parameter sets) are compared to experimental values.⁸⁷

Similar trends are observed in the modeling of vapour-liquid coexistence curves (Figure 3.24). Higher deviation percentages tend to overbind CO₂ complexes yielding an overestimation of the density in the liquid phase (and a corresponding underestimation of the density in the gas phase). However, as opposed to second virial coefficient simulations and the analogous simulations for N₂, no parameter set is able to reproduce the VLCC of CO₂ exactly. In all cases, the force fields overestimates the liquid density gravely. A possible explantion for this behaviour could be the fact that three-body interactions are missing in the force field. Indeed, three-body dispersion represents a repulsive contribution to the interaction energy⁴¹ and neglecting this could explain the anomalous results for the VLCC. Simulations were also performed for reference parameters and a MEDFF with unscaled charges but for these parameter sets the reproduction of the VLCC is abominable. As was the case for the second virial coefficients, reference parameters underbind CO₂ fluids gravely, resulting in an underestimation of the liquid density. For the unscaled charges, the inverse is true.

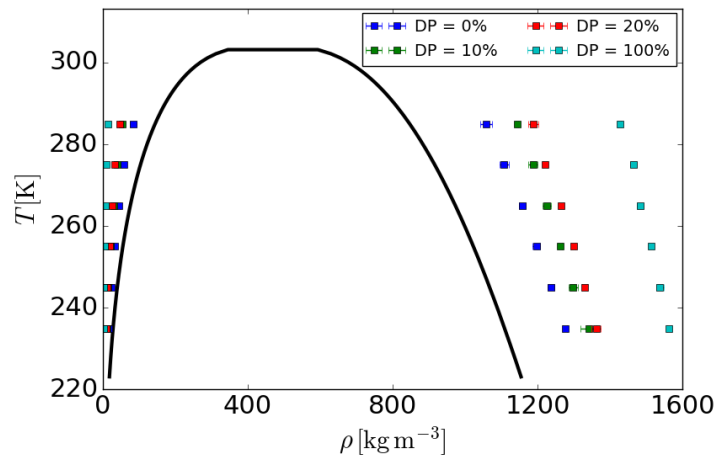


Figure 3.24: Simulations for the vapour-liquid coexistence curve of CO₂ (using MEDFFs with various parameter sets) are compared to experimental values⁸⁸ (black curve).

Chapter 4

Host-Guest Interactions

In order to model the adsorption properties of a nanoporous material, not only guest-guest interactions, but also the interactions between the host and the adsorbates should be considered. When the pressure of the adsorbed gas is low, the adsorption is even completely determined by the latter. In this work the host-guest interactions will once again be modeled by the Monomer Electron Density Force Field. However, the previously used approach to determine interaction parameters is not applicable here. Indeed, SAPT and CCSD(T) methods cannot be applied to combinations of framework lattices and guest molecules. Therefore, two approximative methods will be investigated, respectively based on cluster calculations and adsorption energies.

4.1 ZIF-8

4.1.1 Cluster Model

SAPT and CCSD(T) interaction energies between an adsorbate molecule and its surrounding framework cannot be determined due to the lack of a periodic implementation of these levels of theory but even more due to the incredible computational cost such codes would demand. Therefore, interactions with even smaller parts of the framework, called clusters, are considered. As Figure 4.1 shows, the zinc atoms in ZIF-8 are tetrahedrally surrounded by methyl-imidazole (IZ) linkers. Due to this efficient screening of the metal ions, molecules in the cages of ZIF-8 will mainly experience the effects of the linkers because the zinc atoms are inaccessible. As a result, the proposed cluster model will consider dimers built up by an IZ linker and an adsorbate molecule to derive MEDFF interaction parameters for the host-guest interactions. The determined parameter sets can then be used for interactions with zinc atoms as well since these interactions are small regardless the values of the interaction parameters (e.g. exchange contributions will be negligible because overlap is negligible regardless the value of $U_{\text{exch-rep}}$). While the cluster model is used to derive interaction parameters, MBIS parameters will be taken from DFT calculations performed on the periodic structure for the host and on isolated molecules for the guest. In this way, the electrostatic environment of the framework is reproduced the best.

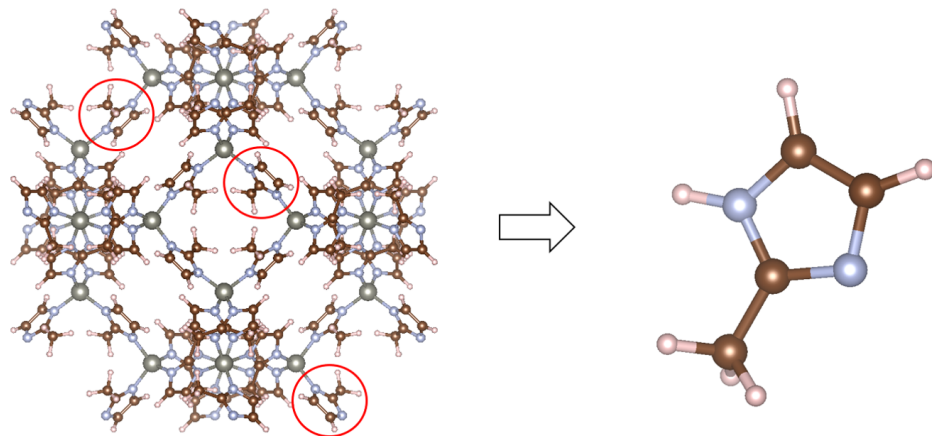


Figure 4.1: Molecular structure of ZIF-8 with highlighted imidazole linkers (left) and the protonated form of the linkers (right).

In ZIF-8, there are twice as many linkers as zinc ions. Because the complete structure is neutral, this implies that the positive charge on zinc atoms is twice as large as the negative charge carried by the linkers. However, the interaction energy in dimers consisting of charged molecules (like IZ) is typically dominated by the electrostatic contribution. Fitting the force field to CCSD(T) interaction energies, other contributions will try to compensate for the (typically larger) deviations in the electrostatic contribution, thus undermining the physical validity of the resulting interaction parameters. Also, spin considerations should be taken into account when charged linkers are utilized. The IZ linkers are therefore terminated by a hydrogen atom on one of the nitrogen atoms, yielding a neutral, closed-shell system (Figure 4.1).

The protonation procedure poses two significant problems. Inspecting Figure 4.1, one notices that adding a hydrogen atom to one of both N atoms, breaks the C_2 symmetry of the charged linker. Chosing which nitrogen atom to protonate is hence equal to chosing between two isomers of the same molecule. These isomers are depicted in Figure 4.2. The presence of isomerism seems to imply that two sets of MBIS parameters should be used for IZ. However, because the IZ isomers are each others mirror image (*i.e.* they are enantiomers), one set of MBIS parameters suffices for both isomers when AIM parameters are correctly assigned to their corresponding atoms. Another potential problem arising from the protonation of the IZ linkers, is the fact that MBIS parameters of the isolated linkers can be altered significantly when compared to their values in the periodic structure. This could change the physics of the interaction between linker and adsorbate molecule, thus jeopardizing the validity of the derived interaction parameters. In Figure 4.2 the MBIS atomic charges in both isomers of the protonated linker (calculated using B3LYP/aug-cc-pVTZ LoT) are compared to the corresponding charges when the MBIS scheme is applied to the electron density of the framework. The charges are particulary different in the neighbourhood of the added atom. However, even there, differences are limited and the proposed monomers can thus be used. Inspecting the charges in both isomers also confirms that one set of MBIS parameters is adequate for both isomers. The framework electron density was determined by applying the periodic projector-augmented-wave (PAW) method,⁸⁹ imple-

mented in the GPAW⁹⁰ program to the fully optimized nuclear structure of the framework. The pseudowave function in the PAW method was represented on a cubic real-space grid with a spacing of about 0.2 Å. For the density functional, the PBE exchange-correlation functional^{91,92} was used. The framework structure was optimized by constructing a local energy profile as a function of volume. Subsequently, the equilibrium volume is obtained by fitting an equation of state to this profile. Finally, a constrained geometry optimization was carried out at this volume in which the positions and cell shape are relaxed. All these calculations were performed with the PBE density functional in combination with D3BJ^{93,94} dispersion corrections via the VASP program.⁹⁵ An energy cut-off of 800 eV was applied and the convergence criterion for the electronic self-consistent field was set to 10^{-8} eV. Furthermore a 1x1x1 Γ-centered grid was used to sample the first Brillouin zone.

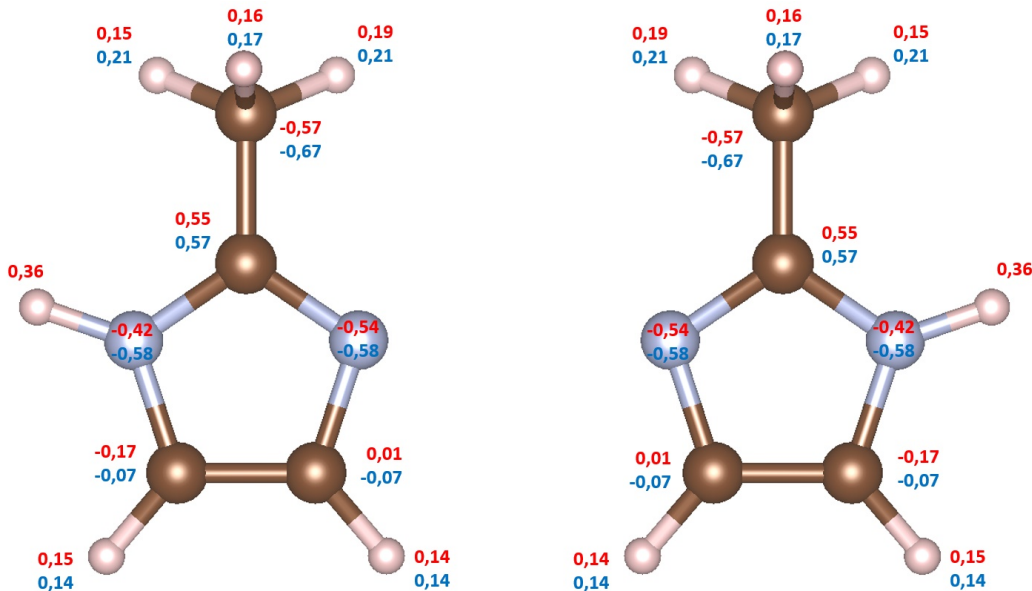


Figure 4.2: The two enantiomers of the protonated imidazole linker, indicating MBIS charges for the isolated molecules (red) and the periodic structure (blue).

For CO₂-CO₂ dimers, it was found that a correction of the MBIS charges is necessary to model the electrostatic interaction properly. Due to the neglect of higher order atomic multipoles, molecular multipoles were modeled incorrectly, preventing the derivation of an effective MEDFF. Higher order atomic multipoles are related to deformed atomic electron densities and thus to highly polar bonds. Since such bonds also occur in IZ linkers, a charge correction procedure should be considered for imidazole linkers as well. For CO₂, the approach proposed by Hadad et al.⁸⁶ was followed. However, this method corrects the atomic charges, local quantities, by means of the molecular multipoles, global quantities. This typically leads to ill-conditioned fits for the charges when molecules with a higher number of atoms are considered. Therefore a local correction method was devised, based on the observation that especially higher order atomic multipoles are important. Herein, all atoms are considered separately and for each atom, distances between this central atom and all the others are calculated. By means of the following cut-off condition, only the nearest atoms are withheld:

$$\text{for central atom A, atom B is rejected} \iff \frac{R_{AB}}{\sigma_{A_v} + \sigma_{B_v}} > c \quad (4.1)$$

When the cut-off, c , is chosen very large, all atoms are included and the Hadad methodology is found again. Here, a cut-off of 5.0 was applied so that the central C atom of the methyl group, for instance, will only experience corrections from its closest neighbours while for the H atom, added during the protonation, both its neighbouring N atom and the C atoms bound to this N atom are considered. For the atoms within the cut-off range, atomic charge corrections are determined by a least-squares fit matching *ab initio* atomic dipole and quadrupole moments of the central atom with those generated by the considered charges. Repeating this procedure with every atom as central atom and summing all the atomic corrections, results in locally determined charge corrections for all atoms. These include the effects of higher order atomic multipoles implicitly and thus manage to reproduce molecular multipoles better as well. As was the case for the charge rescaling procedure for CO₂, all the corrections are performed on core charges. The results for the imidazole linkers are displayed in Appendix A. Except for the atoms in the methyl group, the charge corrections are relatively small. Indeed, due to the large charge transfer from the hydrogen atoms to the central C atom in the methyl group, sizeable atomic dipoles are formed in the hydrogen atoms, causing the large charge corrections. However, it should be noted that the influence on the molecular dipole moment is rather limited because the atomic dipoles largely cancel each other out.

4.1.2 Monomer Electron Density Force Field for IZ-N₂

Since MBIS parameters for both IZ and N₂ were determined in the previous paragraphs and chapters, only the interaction parameters are yet to be determined. This requires SAPT and CCSD(T) interaction energies for complexes consisting of both molecules. Because no accurate data are available concerning the minima of the potential energy surface of these dimers, configurations should be constructed in another way. Random sampling of relative translations and orientations with uniform distributions, has the typical disadvantage of mainly selecting high energy configurations due to their elevated degeneracy. Alternatively, configurations can be extracted from representative adsorption simulations. This way, the minima of the PES are more likely to be sampled, because adsorbates typically occupy low energy adsorption sites. Grand-Canonical Monte Carlo (GCMC) adsorption simulations were hence performed for the considered gases and MOFs. Herein guest-guest interactions were modeled by means of the MEDFFs determined in the previous chapter. Host-guest interactions on the other hand were modeled by a MEDFF where the MBIS parameters of the host originated from periodic PBE-D3BJ calculations and where reference interaction parameters, derived for the dispersion dominated complexes in the S66x8 dataset,⁴⁹ were utilised. Temperature and pressure were respectively set to 298 K and 14 bar. These simulations will also be studied in more detail in the following chapter. Randomly selected snapshots of the simulation were utilised to extract dimers of adsorbates and their nearest linker. For the subsequent protonation, one has to choose between both IZ isomers. Inspecting Figure 4.2 though, one observes that the framework charges are approximately given by the average between the atomic charges in both enantiomers. Therefore dimers with both isomers are added to the dataset. For each adsorbate gas, 50 dimers were

selected from the Monte Carlo simulations, yielding 100 dimers after protonation.

SAPT and CCSD(T) interaction energies were calculated for the selected IZ-N₂ dimers and configurations with a positive interaction energy in the CCSD(T) LoT were excluded from the dataset. For the fitting procedure, Eq. 2.16 was applied again. A σ_{pr} scan was performed both with original and corrected MBIS parameters and the results are displayed in Figure 4.3.

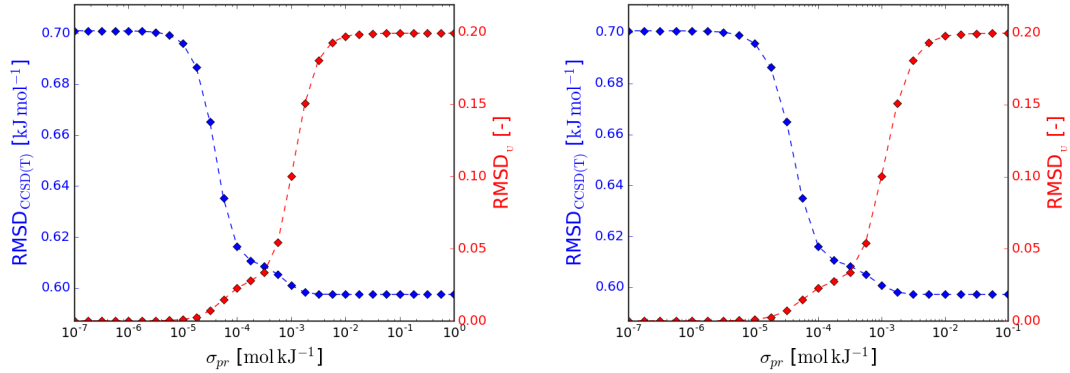


Figure 4.3: Influence of the regularisation strength on $\text{RMSD}_{\text{CCSD(T)}}$ and RMSD_U both for IZ monomers with original (left) and corrected (right) charges.

One notices that both scans look almost exactly the same. This is because the charge correction hardly alters the molecular dipole moment. Indeed, when a molecular dipole is present (*i.e.* when uncharged, polar molecules are considered), this is the leading term in the multipole expansion of the electron density. However, molecular dipoles are typically reproduced to a good degree by uncorrected MBIS charges, reducing the need for charge correction to reproduce interaction energies. In other words, the charge correction typically works best for molecules where highly polar bonds are found and where the leading term in the multipole expansion is the quadrupole. Since IZ is polar it is less significant here. Table 4.1 sums up the important parameter sets for the MEDFF with corrected charges. Inspecting Figure 4.3, DP=10% seems to be a reasonable choice for further use. For the corresponding MEDFF, reproduction of the individual force field contributions as well as the overall performance were evaluated in Appendix B. Comparing RMSDs to typical interaction strengths, one observes that the electrostatics contribution is modeled the worst. Important is that this contribution is modeled equally insufficient with uncorrected charges, implying that corrections up to atomic quadrupoles do not suffice for highly precise modeling of the electrostatic interaction energy. One could hence include even higher order atomic multipoles in the local charge correction method. However, due to the limited number of charges and the increasing number of DoFs in the multipoles, the reproduction of lower order atomic multipoles would suffer under this operation. The risk of sloppy fits would also increase in this way. Including the higher order multipoles explicitly is another option but this makes force field evaluation in e.g. MC simulations significantly slower. Therefore, the model at hand, which is already quite accurate, is used in the following chapters.

DP	σ_{pr}	$U_{\text{exch-rep}}$	U_{ind}	U_{s8}
0%	∞	8.964	-1.140	0.704
10%	37.93	9.652	-1.132	1.008
20%	9.585	9.861	-1.129	1.044
100%	0.000	10.25	-1.124	1.038

Table 4.1: Regularisation parameters (in 10^{-5} mol kJ $^{-1}$) and corresponding interaction parameters (in a.u.) for the MEDFF of IZ-N₂ with corrected charges for IZ.

4.1.3 Monomer Electron Density Force Field for IZ-CO₂

For IZ-CO₂ dimers, the same procedure as for IZ-N₂ is followed. To determine interaction parameters, a σ_{pr} scan is performed for both the original and corrected charges of IZ and the results are displayed in Figure 4.4. CO₂ molecules were in both cases modeled by rescaled AIM parameters.

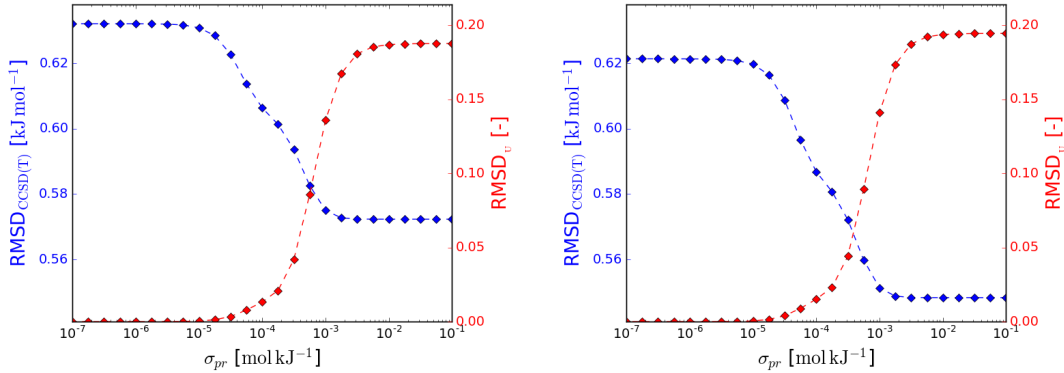


Figure 4.4: Influence of the regularisation strength on RMSD_{CCSD(T)} and RMSD_U both for IZ monomers with original (left) and corrected (right) charges.

Again, the corrected charges perform only slightly better than the original charges, though the improvement is larger than for IZ-N₂ dimers. Interaction parameters for the typical deviation percentages are listed in Table 4.2. Figure 4.4 shows that DP=20% offers a good compromise between accuracy (low RMSD_{CCSD(T)}) and physical validity (low RMSD_U). The corresponding force field will therefore be used in the following chapters. Its performance is evaluated in Appendix B. Comparing RMSDs to typical interaction strengths, induction is observed to perform the worst. A possible explanation for this could be the relatively rudimentary model used for this contribution. Another ascertainment is that the force field is more accurate than the MEDFF for IZ-N₂, mainly because of the better modeling of the electrostatics contribution (due to the charge rescaling for CO₂).

DP	σ_{pr}	$U_{\text{exch-rep}}$	U_{ind}	U_{s8}
0%	∞	7.888	-1.004	0.992
10%	7.781	8.259	-1.000	1.170
20%	5.003	8.468	-0.998	1.269
100%	0.000	9.137	-0.990	1.433

Table 4.2: Regularisation parameters (in 10^{-4} mol kJ $^{-1}$) and corresponding interaction parameters (in a.u.) for the MEDFF of IZ-CO₂ with corrected charges for IZ and CO₂

4.1.4 Adsorption Energies

Since SAPT and CCSD(T) methods are not applicable for a molecule adsorbed in a periodic framework, one has to revert to cluster models as described in the previous section. Another computationally feasible approach consists of determining host-guest interaction parameters based on framework-adsorbate interaction energies, calculated in more manageable level of theory. Therefore, this section considers adsorption energies in periodic structures, calculated by DFT-D methods. These adsorption energies are differences between the energy of a framework with one adsorbate molecule in each unit cell and the energies of the empty framework and the guest molecules separately. Fitting force field adsorption energies to their *ab initio* counterparts, host-guest interaction parameters can be derived while taking into account the complete framework instead of small clusters. The only sacrifice of this methodology is the relative lack of accuracy in DFT calculations, compared to e.g. Coupled-Cluster.

Adsorption energies were calculated for framework-guest complexes, constructed by means of GCMC adsorption simulations at 298 K and 14 bar. From randomly selected Monte Carlo snapshots, adsorbate molecules were extracted and placed in their surrounding unit cell. In this way, 100 configurations were constructed for each adsorbate gas. In the simulations, interactions were modeled by means of MEDFFs, similar to those used for the construction of dimers in the previous section, but now host-guest interactions utilize the optimal parameter set from the cluster model instead of the reference parameters for the S66x8 dataset. This force field model will be called MEDFF-FF (FF from Fit-Fit) because for both guest-guest and host-guest interactions fitted interaction parameters were used. High pressure simulations were performed in order to sample all the adsorption sites favored by the force field.

For the selected configurations, adsorption energies were calculated by the VASP program. The PBE density functional with MBDHI (*i.e.* the MBD^{96–98} scheme combined with iterative Hirschfeld AIM parameters⁹⁹) dispersion corrections was used and to sample the first Brillouin zone, a 3x3x3 Γ -centered grid was utilized. Furthermore an energy cut-off of 700 eV was applied and the convergence criterion for the electronic self-consistent field was set to 10^{-8} eV. Once the *ab initio* adsorption energies are calculated, host-guest interaction parameters can be (re)fitted. For this purpose a cost function similar to Eq. 2.16 is used but now the energies in the first term are adsorption energies instead of dimer interaction energies. For the reference interaction parameters, the host-guest parameter set of the MEDFF-FF was used. The determination of

refitted interaction parameters thus relies on the cluster model as well. Indeed, not only are significant configurations sampled by means of the MEDFF-FF, but the interaction parameters also play a crucial role as reference values for the refit. Even if $\sigma_{pr} = \infty$ (*i.e.* in case of a complete refit), these reference parameters still have an influence on the limit values of the refitted interaction parameters. This is especially important for $U_{\text{exch-rep}}$ and U_{ind} . Indeed, if no reference values were present, then these parameters would not be uniquely determined because changing both of them by the same amount has exactly the same effect on the force field. By introducing the reference values however, a unique determination of all interaction parameters and thus a correct physical interpretation of all force field contributions remains possible.

ZIF-8 - N₂

Since the cost function for the refit is similar to Eq. 2.16, deviation percentages can be defined analogously as before. Indeed, for the adsorption energies of N₂ in ZIF-8, a σ_{pr} scan was performed and is displayed below (Figure 4.5).

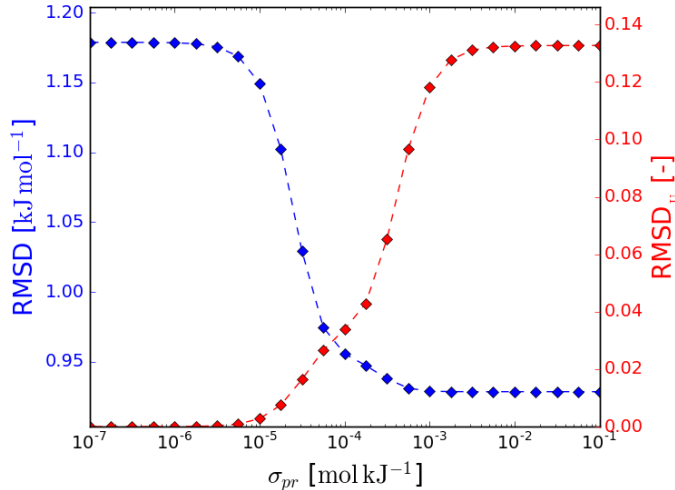


Figure 4.5: Influence of the regularisation strength on RMSD (the root mean squared deviation between *ab initio* and force field adsorption energies) and RMSD_U.

The figure shows that the accuracy of the force field (in terms of a low RMSD w.r.t. *ab initio* adsorption energies) can be improved greatly by refitting the parameters. Refitted interaction parameters were determined for DPs equal to 0%, 50% and 100% and are listed in Table 4.3.

DP	σ_{pr}	$U_{\text{exch-rep}}$	U_{ind}	U_{s8}
0%	∞	10.83	-1.115	1.204
50%	2.700	9.872	-1.129	1.003
100%	0.000	9.652	-1.132	1.008

Table 4.3: Regularisation parameters (in 10^{-5} mol kJ⁻¹) and corresponding interaction parameters (in a.u.) for the MEDFF refitted to adsorption energies.

The reproduction of *ab initio* PBE-MBDHI adsorption energies by the MEDFFs with DP 0% (fully refitted, also called MEDFF-Refit) and 100% (cluster model, MEDFF-FF) was compared in Figure 4.6. The most important difference is that, due to refitting, the force field becomes more repulsive. Indeed, the mean deviation (MD) increases from a negative to a positive value, implying that on average force field energies increase (*i.e.* become less negative). In this way the outliers below the bisector in Figure 4.6 are corrected for, thus improving the reproduction of *ab initio* adsorption energies.

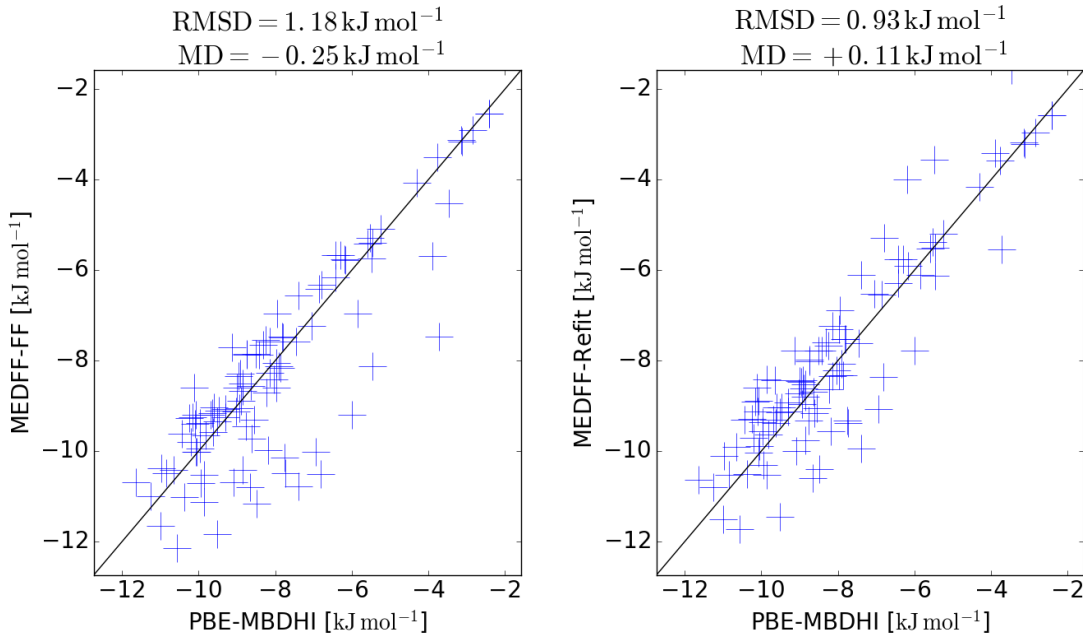


Figure 4.6: Comparison between the reproduction of adsorption energies by the MEDFF-FF (left) and MEDFF-Refit with DP=0% (right).

ZIF-8 - CO₂

Adsorption energies were also determined for CO₂ in ZIF-8. Applying the same fitting procedure as before, the following σ_{pr} scan was calculated (Figure 4.7). Corresponding interactions parameters are listed in Table 4.4.

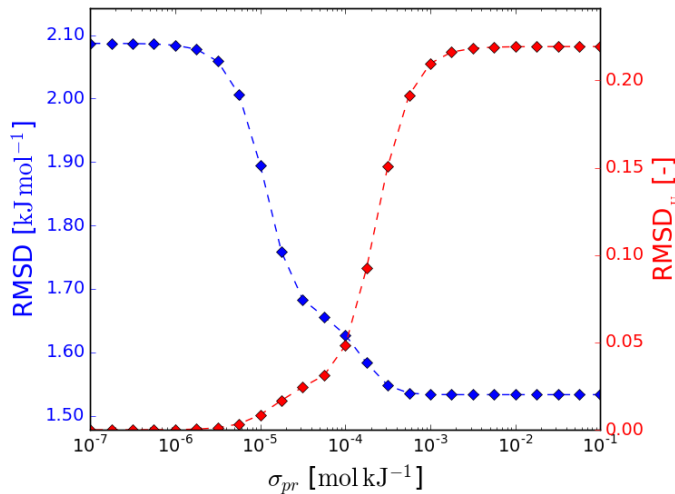


Figure 4.7: Influence of the regularisation strength on RMSD and RMSD_U .

DP	σ_{pr}	$U_{\text{exch-rep}}$	U_{ind}	U_{s8}
0%	∞	9.855	-0.978	1.703
50%	1.483	8.667	-0.995	1.261
100%	0.000	8.468	-0.998	1.269

Table 4.4: Regularisation parameters (in 10^{-5} mol kJ $^{-1}$) and corresponding interaction parameters (in a.u.) for the MEDFF refitted to adsorption energies.

As was the case for the adsorption of N₂ in ZIF-8, the reproduction of *ab initio* adsorption energies was evaluated for MEDFF-FF and MEDFF-Refit in Figure 4.8. Again, the force field becomes more repulsive by refitting the interaction parameters. However, the most attractive configurations remain overbound. Comparing the RMSDs to the typical adsorption energies, the errors are larger for the adsorption of CO₂ in ZIF-8 than for N₂ in ZIF-8, indicating that the MEDFF for CO₂ in ZIF-8 is expected to be less reliable.

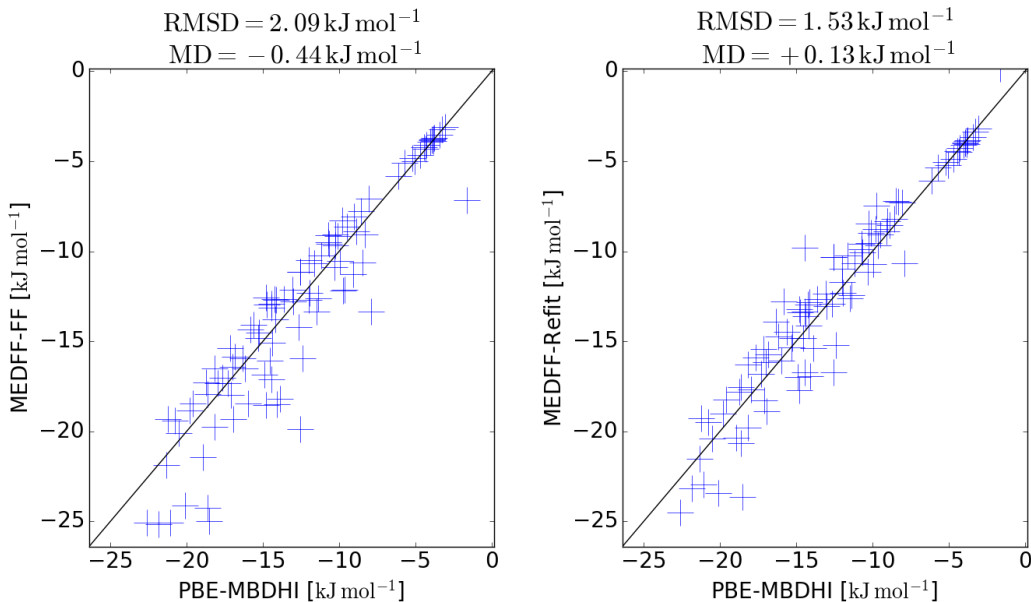


Figure 4.8: Comparison between the reproduction of adsorption energies by the MEDFF-FF (DP=100%) and MEDFF-Refit (DP=0%)

4.2 MIL-53(Al)

4.2.1 Cluster Model

Even though the unit cell of MIL-53(Al) contains less atoms than the unit cell of ZIF-8, one should still consider clusters to make CCSD(T) and SAPT calculations computationally feasible. However, the selection of representative, neutral, closed-shell clusters is not straightforward. Indeed, inspecting the molecular structure of the framework in Figure 4.9, one notices that the metal-oxide chains are screened less efficiently than the zinc atoms in ZIF-8. While one can still use the linker as a viable cluster, a second cluster containing metal-oxides should be considered as well. Indeed, to model the flexible behaviour of this MOF, Vanduyfhuy et al. also selected both metal-oxide and linker clusters.³² Furthermore, it was mentioned before that metal-oxides and particularly the bridging OH groups play a crucial role in the breathing behaviour of the framework upon adsorption.^{57,100} Their influence on the host-guest interaction should thus not be underestimated and therefore the following two clusters were chosen (Figure 4.9).

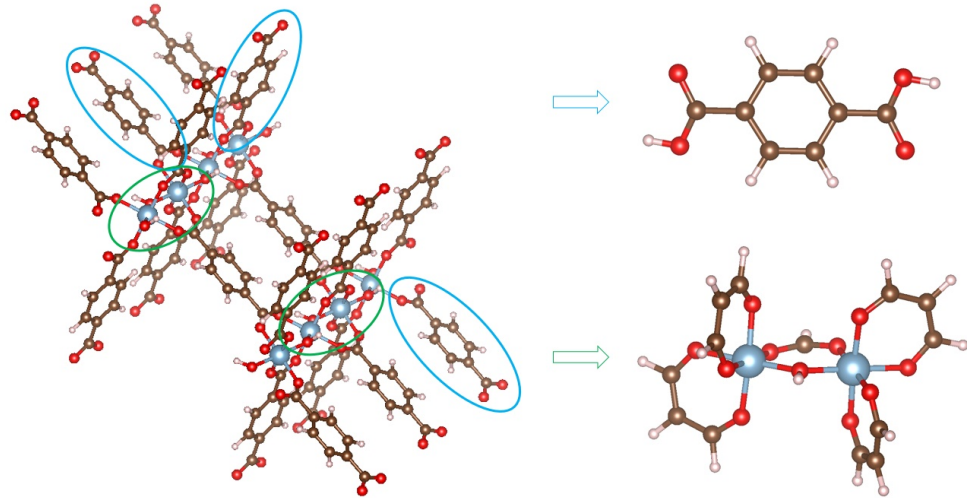


Figure 4.9: Molecular structure of MIL-53(Al) with highlighted BDC and metal-oxide clusters (left) as well as the terminated form of these clusters (right).

The BDC linkers demand two hydrogen atoms to constitute a neutral, closed-shell system. As Figure 4.9 shows, these atoms are added on both sides of the molecule. This choice not only makes the cluster more stable than when both atoms would be added on the same side, it also precludes the linker from having a large dipole moment along its axis, which is also not the case in the framework. Even though the protonated BDC cluster is larger than the IZ linkers for ZIF-8, dimer calculations with BDC linkers are computationally manageable. For the metal-oxide cluster on the other hand, both extra carbon and hydrogen atoms were added to render the structure neutral and closed-shell, making the cluster too large for the application of SAPT and CCSD(T) methods. As a result, host-guest interactions will be modeled by only considering the BDC linkers. This is a far-reaching, though necessary approximation to keep *ab initio* calculations computationally tractable.

Due to the double termination of the BDC linkers, no isomerism is introduced by the protonation process. However, one should still ascertain that the difference between MBIS charges in the framework and the isolated molecule is limited. This is confirmed in Figure 4.10. The largest differences are typically found near the H atoms used for protonation, but even these differences are limited. To determine the charges in the periodic structure, the electron density of the framework was calculated in the PBE LoT by means of the PAW method, implemented in GPAW. Similar settings as for ZIF-8 were used. To optimize the framework structures, VASP calculations were performed, using the PBE-D3BJ density functional. The energy cut-off was now set to 500 eV and the convergence criterion for the electronic self-consistent field was 10^{-5} eV. For the narrow pore structure (unit cell volume of 1050 \AA^3), the first Brillouin zone was sampled by a $2 \times 6 \times 6$ Γ -centered grid, while for the large pore structure (unit cell volume of 1430 \AA^3), a $2 \times 6 \times 2$ grid was used.

The protonated BDC linker also has inversion symmetry around the center of the benzene

ring. As a result the molecule is apolar. Because charge corrections are typically important in apolar molecules, the local charge correction method was applied here as well. Original and corrected MBIS parameters are displayed in Appendix A. The largest corrections are found for the carbon atoms in the benzene ring, bound to hydrogen and nearest to the oxygen atoms without hydrogen. However, even these corrections are relatively small and the charge correction is hence expected to have a limited influence.

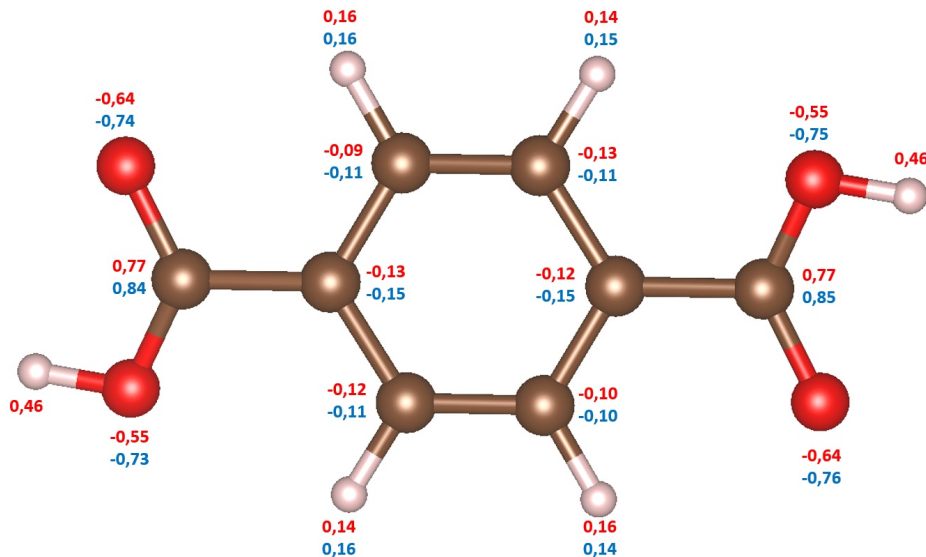


Figure 4.10: The protonated BDC linker with MBIS charges for the isolated molecules (red) and the periodic structure (blue).

4.2.2 Monomer Electron Density Force Field for BDC-N₂

Dimers including BDC linkers were also constructed by extraction from randomly selected snapshots of GCMC adsorption simulations. In this case, the adsorption of N₂ in MIL-53(Al) in its large pore phase was considered. 100 dimers were constructed and those with a positive interaction energy in the CCSD(T) level of theory were excluded from the dataset. A σ_{pr} scan was performed for both original and corrected charges of BDC and is displayed in Figure 4.11.

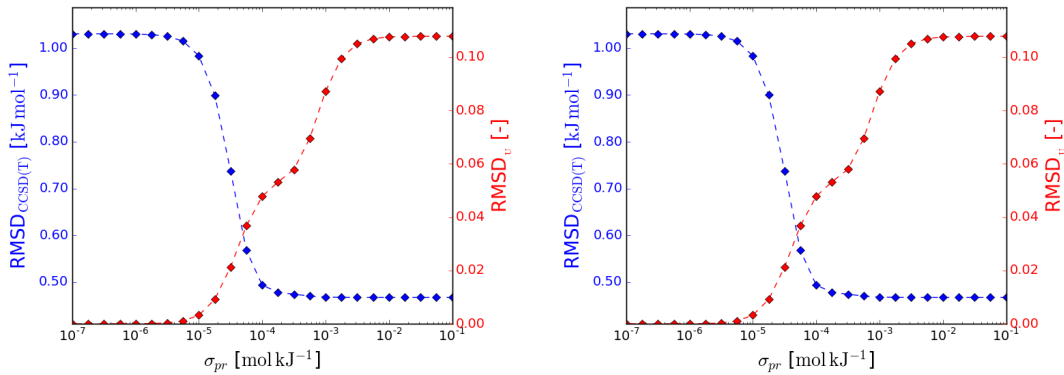


Figure 4.11: Influence of the regularisation strength on $\text{RMSD}_{\text{CCSD}(\text{T})}$ and RMSD_U for BDC monomers with original (left) and corrected (right) charges.

As was the case for IZ-N₂ and IZ-CO₂ complexes, the scans look almost exactly the same for original and corrected charges. Indeed, the influence of the charge correction was expected to be limited due to the small corrections of the MBIS charges. Interaction parameters were determined for the typical deviation percentages in Table 4.5. A DP of 10% was considered reasonable for further use and the corresponding MEDFF is evaluated in Appendix B. Comparing typical interaction energies with RMSDs, one concludes that the dispersion contribution is modeled the best, followed by exchange-repulsion, induction and electrostatics. This is in accordance with the previously derived MEDFFs. The overall performance of the force field is also better than for the MEDFF of IZ-N₂.

DP	σ_{pr}	$U_{\text{exch-rep}}$	U_{ind}	U_{s8}
0%	∞	9.237	-0.764	0.820
10%	8.228	9.423	-0.762	0.977
20%	5.446	9.297	-0.763	0.982
100%	0.000	8.772	-0.767	0.999

Table 4.5: Regularisation parameters (in 10^{-5} mol kJ⁻¹) and corresponding interaction parameters (in a.u.) for the MEDFF of BDC-N₂ with corrected charges for BDC.

4.2.3 Monomer Electron Density Force Field for BDC-CO₂

The fitting procedure was also applied to dimers consisting of protonated BDC linkers and CO₂. A σ_{pr} was performed first and is displayed in Figure 4.12.

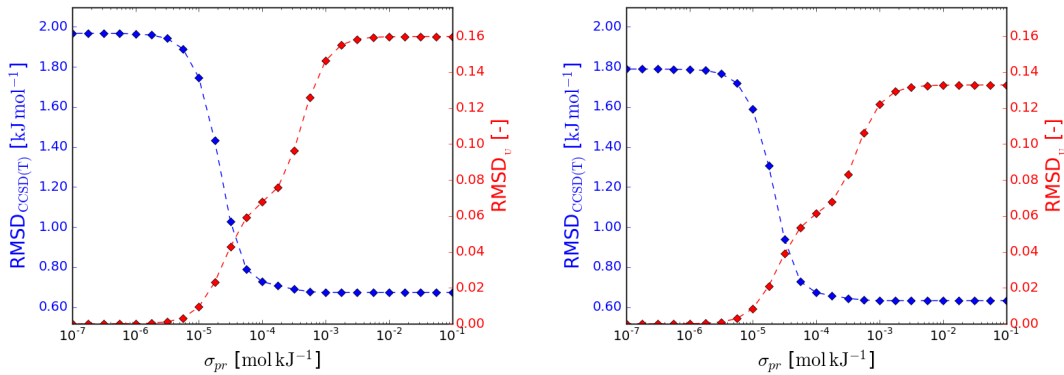


Figure 4.12: Influence of the regularisation strength on $\text{RMSD}_{\text{CCSD}(\text{T})}$ and RMSD_U for BDC monomers with original (left) and corrected (right) charges.

In contrast to the previous host-guest dimers, the charge correction, however limited, improves the fit of the interaction parameters for BDC-CO₂. Indeed, both RMSD_U in the CCSD(T) limit and $\text{RMSD}_{\text{CCSD}(\text{T})}$ in the SAPT limit are lowered significantly. Parameter sets for the typical deviation percentages are listed in Table 4.6. For the MEDFF with DP=10%, *ab initio* interaction energies are compared with their corresponding force field approximation in Appendix B. All contributions as well as the complete interaction energies are reproduced to a good degree.

DP	σ_{pr}	$U_{\text{exch-rep}}$	U_{ind}	U_{s8}
0%	∞	8.230	-0.814	1.050
10%	5.381	8.598	-0.810	1.310
20%	4.044	8.519	-0.811	1.318
100%	0.000	7.934	-0.817	1.358

Table 4.6: Regularisation parameters (in 10^{-5} mol kJ⁻¹) and corresponding interaction parameters (in a.u.) for the MEDFF of BDC-CO₂ with corrected charges for BDC.

4.2.4 Adsorption Energies

Fitting interaction parameters by means of adsorption energies was also performed for MIL-53(Al). Since this framework is observed to breathe upon CO₂ adsorption, CO₂ adsorption energies were calculated in both large pore and narrow pore phases. Configurations were obtained from GCMC adsorption simulations at 298 K and 14 bar wherefore interactions were modeled by means of the optimal MEDFF-FF force fields, determined in the previous section. For each of the selected configurations adsorption energies were calculated in the PBE-MBDHI LoT by the VASP program. All settings were identical to those used for the structure optimization. Reproduction of *ab initio* adsorption energies as well as the refitting of interaction parameters is studied below.

MIL-53(Al) (lp) - N₂

A σ_{pr} scan for the refit of host-guest interaction parameters of N₂ in MIL-53(Al) (in its large pore phase) is displayed in Figure 4.13. By refitting, the RMSD can be reduced substantially. In doing this, RMSD_U increases only to 14% and therefore the same DPs as before are utilized. Corresponding interaction parameters are listed in Table 4.7.

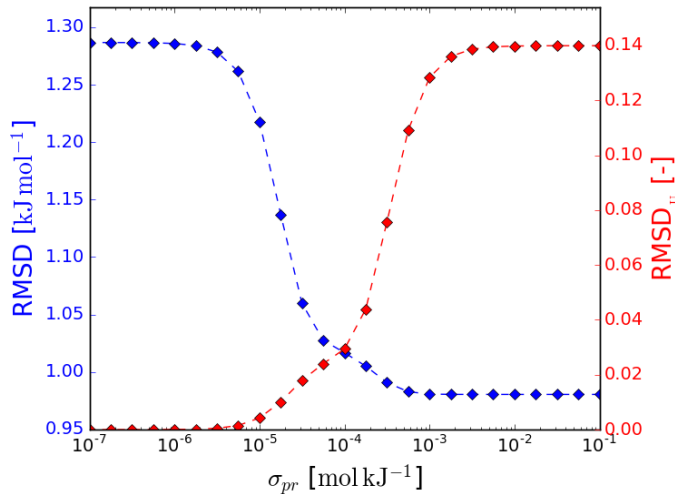


Figure 4.13: Influence of the regularisation strength on RMSD and RMSD_U.

DP	σ_{pr}	$U_{\text{exch-rep}}$	U_{ind}	U_{s8}
0%	∞	9.300	-0.763	0.740
50%	1.839	9.587	-0.761	0.972
100%	0.000	9.423	-0.762	0.977

Table 4.7: Regularisation parameters (in 10^{-5} mol kJ⁻¹) and corresponding interaction parameters (in a.u.) for the refit of the MEDFF describing the interaction between MIL-53(Al) (lp) and N₂.

Comparing adsorption energies for the original and refitted force field, one observes that the force field becomes more repulsive by refitting, thus increasing the level of reproduction. This is in accordance with the results found earlier.

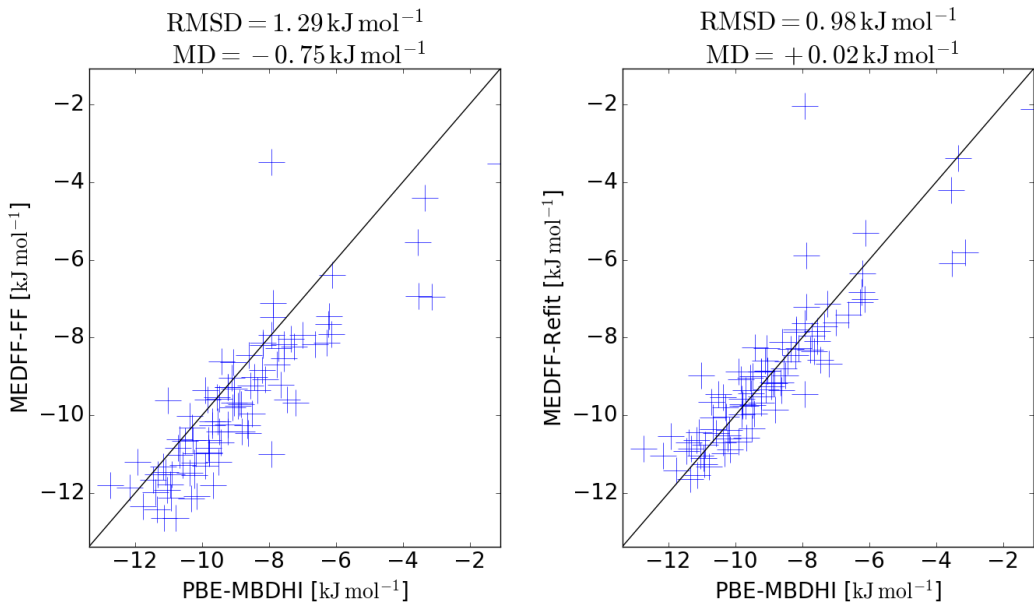


Figure 4.14: Comparison between the reproduction of adsorption energies by the MEDFF-FF (DP=100%) and MEDFF-Refit (DP=0%)

MIL-53(Al) (lp) - CO₂

A σ_{pr} scan for the adsorption energies of CO₂ adsorption in the large pore phase of MIL-53(Al) is displayed in Figure 4.15.

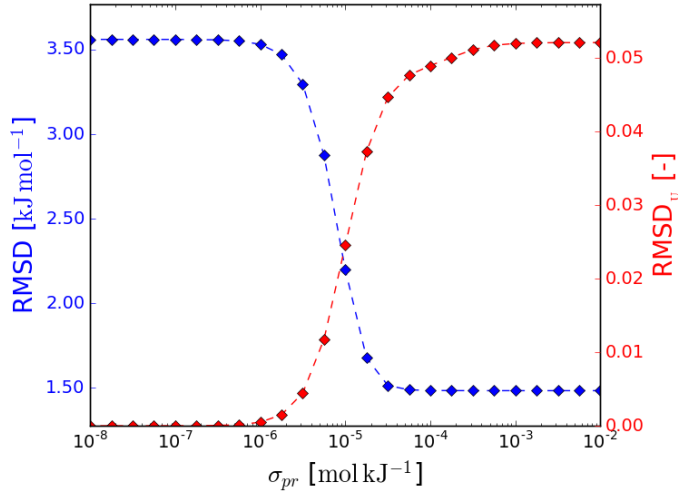


Figure 4.15: Influence of the regularisation strength on RMSD and RMSD_U.

Although RMSDs can be reduced greatly by the refit, they remain larger than for the adsorption of N₂ in MIL-53(Al). RMSD_U values on the other hand are significantly lower, implying that in the refitted force field small changes in interaction parameters have a far-reaching influence on the force field predictions for the adsorption energies. This is also illustrated by Table 4.8

and Figure 4.16 where interaction parameters for typical DPs are listed and original and refitted parameter sets are compared respectively.

DP	σ_{pr}	$U_{\text{exch-rep}}$	U_{ind}	U_{s8}
0%	∞	9.223	-0.805	1.241
50%	7.904	8.866	-0.808	1.298
100%	0.000	8.598	-0.810	1.310

Table 4.8: Regularisation parameters (in $10^{-6} \text{ mol kJ}^{-1}$) and corresponding interaction parameters (in a.u.) for the refit of the MEDFF describing the interaction between MIL-53(Al) (lp) and CO₂.

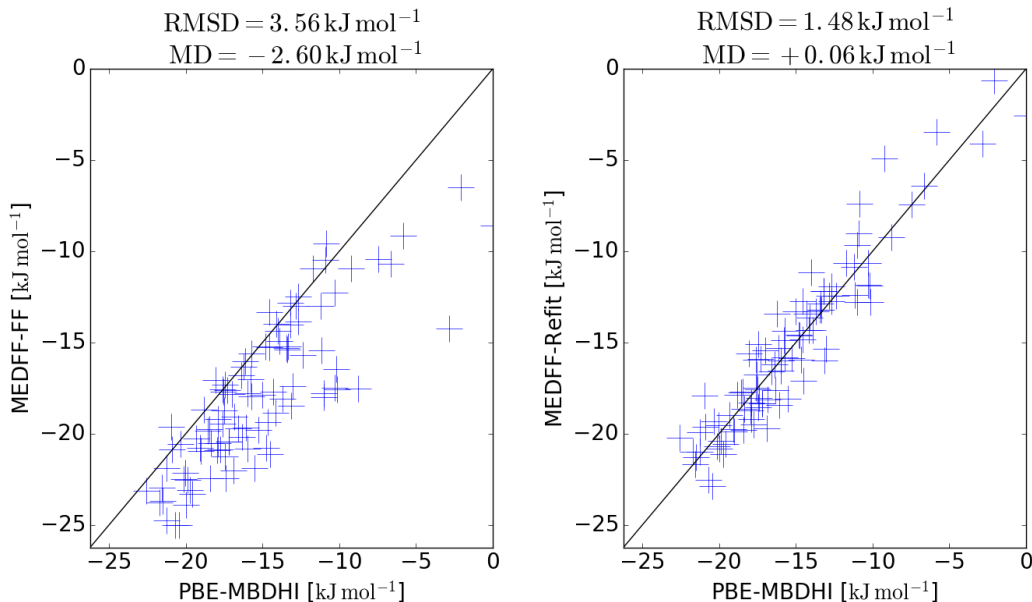


Figure 4.16: Comparison between the reproduction of adsorption energies by the MEDFF-FF (DP=100%) and MEDFF-Refit (DP=0%)

MIL-53(Al) (np) - CO₂

Adsorption energies for CO₂ in MIL-53(Al) were also calculated in the narrow pore phase. A σ_{pr} scan was performed and is displayed in Figure 4.17.

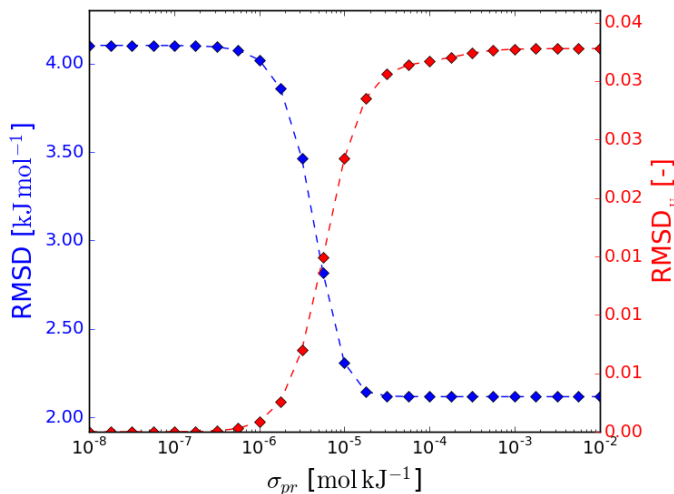


Figure 4.17: Influence of the regularisation strength on RMSD and RMSD_U.

Only slightly altering the interaction parameters (RMSD_U increases only to less than 4%), the RMSD w.r.t. the *ab initio* adsorption energies can be halved. However, errors remain larger than for the adsorption of CO₂ in the large pore phase. Refitted host-guest interaction parameters are displayed in Table 4.8. Between the fully refitted interaction parameters in narrow and large pore phases a RMSD_U of only 3.2% is found. Similar interaction host-guest parameters are thus derived in both phase. Indeed, while interaction parameters can differ for various materials, they should not change when a phase transition is considered. This is confirmed in Tables 4.8 and 4.9.

DP	σ_{pr}	$U_{\text{exch-rep}}$	U_{ind}	U_{s8}
0%	∞	9.084	-0.806	1.307
50%	4.507	8.762	-0.809	1.303
100%	0.000	8.598	-0.810	1.310

Table 4.9: Regularisation parameters (in 10⁻⁶ mol kJ⁻¹) and corresponding interaction parameters (in a.u.) for the refit of the MEDFF describing the interaction between MIL-53(Al) (np) and CO₂.

Figure 4.18 shows that by refitting the interaction parameters, mainly higher adsorption energies are corrected, typically making them more repulsive. Indeed, for the more favorable adsorption sites, errors become even larger than before the refit. A possible explanation for this, could be the fact that in the narrow pore phase the interactions with the bridging OH groups are more important than in the large pore phase. Indeed, CO₂ molecules forming hydrogen-like bonds with the bridging OH groups are responsible for the phase transition.^{57,100} The fact that identical parameters are used for interactions with linkers and metal-oxides, could thus explain why the energy of these favorable adsorption sites is underestimated.

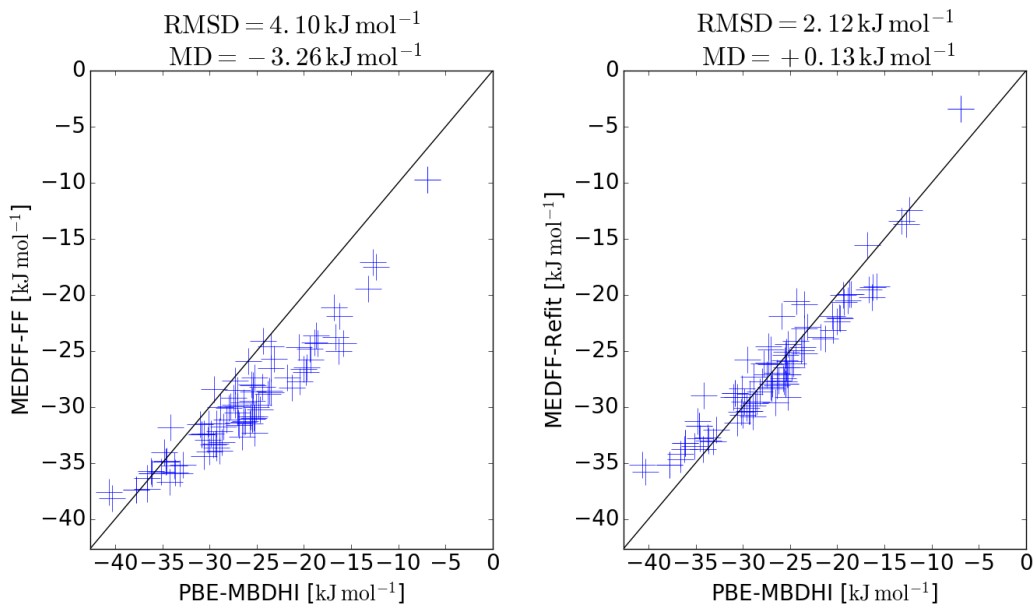


Figure 4.18: Comparison between the reproduction of adsorption energies by the MEDFF-FF (DP=100%) and MEDFF-Refit (DP=0%)

Chapter 5

Adsorption Isotherms

In the previous chapters, multiple parameter sets were proposed for Monomer Electron Density Force Fields describing the mutual interactions between N₂ and CO₂ molecules as well as the interactions between these molecules and the nanoporous materials ZIF-8 and MIL-53(Al). The derived force fields will now be utilized to study the adsorption properties of these MOFs. Particulary important are adsorption isotherms, curves displaying how much of a gas species is adsorbed as a function of pressure at a certain temperature. Making use of various force field models, adsorption isotherms will be simulated and compared to the experiment. Based on adsorption energies, similarities and differences between simulation and experiment will be interpreted.

Adsorption isotherms are simulated the most intuitively in the NPT ensemble. Herein, the system under consideration consists of two subsystems. On the one hand there is a bulk fluid system, containing a large amount of unadsorbed gas molecules, and on the other hand there is the adsorbed fluid system, containing the molecules adsorbed by the framework. The complete system has a fixed particle number, pressure and temperature and composite systems can exchange particles and energy. Volume exchange is not possible because the framework is considered to be rigid. As a result, pressure is equilibrated via volume changes in the bulk fluid phase only. While simulations in the NPT ensemble largely mimic the physical reality, it is computationally cheaper to consider the grand-canonical μ VT ensemble, where instead of completely modeling the bulk gas, equilibrium with this gas is imposed by a fixed chemical potential and temperature. In equilibrium the chemical potential of the adsorbed gas is equal to the one imposed by the bulk gas. Via the equation of state of the bulk gas one can then relate this chemical potential to the pressure, thus allowing to calculate the uptake as a function of the pressure. In this work, the Peng-Robinson¹⁰¹ equation of state was used for this purpose.

Adsorption isotherms were simulated in the grand-canonical ensemble via the Monte Carlo method (GCMC), implemented in the RASPA⁸² program. In each step of the GCMC simulations, particles are attempted to be added, removed, translated, rotated or removed and immediately reinserted elsewhere with equal probabilities. The acceptance of an attempted move depends on the increase or decrease in energy and particle number. Initially, no guest molecules are adsorbed in the framework. Therefore, an equilibration run of 10 000 cycles is

executed in order to approximate thermodynamic equilibrium. The equilibration step is followed by a production run of 50 000 cycles during which the loading of the framework is calculated by means of a running average. A cycle itself consists of $\text{max}(20, N)$ Monte Carlo steps with N being the number of particles adsorbed in the framework. As a result, typically millions of Monte Carlo moves are considered for one adsorption simulation.

The acceptance of an attempted Monte Carlo move depends on the corresponding change in internal energy of the system. Since frameworks and adsorbates were kept rigid, the corresponding self-energies were excluded from this internal energy and as a result, the acceptance of a Monte Carlo step only depends on changes in non-covalent host-guest and guest-guest interaction energies. These energy changes are calculated by means of a force field. Indeed, due to the introduction of a force field, energy changes can be evaluated without *ab initio* calculations, hence speeding up GCMC simulations. Typically force fields are also pairwise-additive, making it possible to evaluate energy changes even more efficiently. In this work, five force fields were utilized for the determination of adsorption isotherms: four variants of the MEDFF and the generic DREIDING²⁰-TraPPE²⁵ force field. The various MEDFF models all use the same set of MBIS AIM parameters and are thus discerned by their interaction parameters:

- MEDFF-RR: In the MEDFF-RR (RR from Reference-Reference) both host-guest and guest-guest interactions utilize the reference interaction parameters, determined for the dispersion-dominated complexes in S66x8 dataset.⁴⁹
- MEDFF-RF: While host-guest interactions are still modeled by the reference interaction parameters, fitted parameters (determined in Chapter 3) are used for the guest-guest interaction. Therefore, this model is called MEDFF-RF (RF from Reference-Fit).
- MEDFF-FF: Both host-guest and guest-guest interaction parameters originate from fits to SAPT and CCSD(T) interaction energies (cfr. Chapters 3 and 4) in the MEDFF-FF (FF from Fit-Fit) model.
- MEDFF-Refit: Host-guest interaction parameters can be refitted by means of adsorption energies (cfr. Chapter 4), giving rise to the MEDFF-Refit model. Guest-guest interaction parameters are still modeled by fitted parameters.

The generic force field on the other hand, models host-guest interactions by means of the DREIDING force field while for guest-guest interactions the TraPPE force field is used. In the DREIDING model, charges need to be attributed to the interacting atoms. Herefore, the MBIS charges, used for the MEDFFs, are utilised again.

5.1 ZIF-8

5.1.1 N₂

For the adsorption in ZIF-8, the simulation volume was built up by 2x2x2 unit cells. In this way, the linear system length in each direction is at least twice as large as the van der Waals cut-off, which was chosen to be 14.0 Å. Regarding N₂ adsorption, the set of MBIS parameters consists

of unscaled charges originating from B3LYP/aug-cc-pVTZ calculations for N₂ and uncorrected charges originating from PBE-D3BJ calculations for the framework. Charge rescaling is not usable for N₂ since there are no charges to rescale. For the framework on the other hand, the influence of charge correction is expected to be negligible since its influence on IZ-N₂ and IZ-CO₂ interaction energies was negligible as well. The interaction parameters in the different MEDFF models are displayed in Table 5.1. As mentioned before, only the sum of $U_{\text{exch-rep}}$ and U_{ind} , also denoted by U_{olp} , has an influence on the force field. Therefore these parameters were displayed as well.

Force Field	host-guest				guest-guest			
	$U_{\text{exch-rep}}$	U_{ind}	U_{s8}	U_{olp}	$U_{\text{exch-rep}}$	U_{ind}	U_{s8}	U_{olp}
MEDFF-RR	8.43	-0.86	0.57	7.57	8.43	-0.86	0.57	7.57
MEDFF-RF	8.43	-0.86	0.57	7.57	9.00	-0.47	0.82	8.53
MEDFF-FF	9.65	-1.13	1.01	8.52	9.00	-0.47	0.82	8.53
MEDFF-Refit	10.83	-1.12	1.20	9.71	9.00	-0.47	0.82	8.53

Table 5.1: Interaction parameters (in a.u.) for the various MEDFF models describing N₂ adsorption in ZIF-8.

In Figure 5.1 the reproduction of experimental adsorption isotherms⁶⁰ is evaluated for T=298 K. Isotherms for other temperatures (308 K and 328 K) are qualitatively very similar and are therefore shown in Appendix C. All simulations are found to overestimate the adsorption. Inspecting the MEDFF-RR and MEDFF-RF isotherms, one observes that altering the guest-guest interaction parameters only has a limited influence on the adsorption isotherms due to the relatively low number of adsorbed molecules. The overestimation of the adsorption isotherms thus seems to originate from the host-guest interactions. Indeed, in Chapter 4, for instance, it was mentioned that by refitting the MEDFF-FF, it became more repulsive. This is confirmed by the adsorption isotherms; while the MEDFF-FF overestimates the adsorption greatly, deviations are less striking for the MEDFF-Refit. However, overbinding of the host-guest interaction is not the only explanation for the deviating simulations. Experimental samples typically consist of powders and thus a significant lowering of the adsorption isotherms can be expected due to surface effects originating from the finite grain size. Also crystallographic defects and impurities make that simulated bulk adsorption isotherms will always differ from the experiment. A third reason for the observed deviations could be framework flexibility. Even though ZIF-8 undergoes no global phase transition, local (normal mode) vibrations and small changes in the unit cell volume upon adsorption can have a notable influence on the gas uptake. Considering only rigid frameworks with a fixed unit cell volume thus also results in deviations.

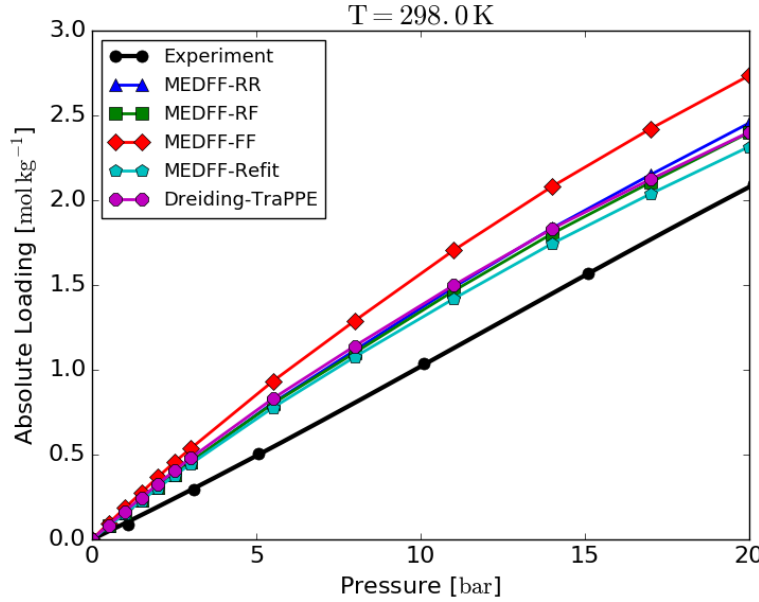


Figure 5.1: Comparison between simulated and experimental⁶⁰ adsorption isotherms for the adsorption of N₂ in ZIF-8 at 298.0 K. Adsorption isotherms for other temperatures can be found in Appendix C.

It was mentioned before that for low pressures, adsorption is dominated by host-guest interactions. Indeed, adsorbates are sparse and hence barely experience each others presence. The quality of the host-guest part of the force field can therefore be evaluated separately by inspecting low pressure adsorption isotherms. Since the isotherms are typically linear in this pressure range, especially the slope, determined by the so-called Henry coefficient, is determinative. Low pressure adsorption isotherms at 298.0 K were hence compared with experimental data taken from McEwen et al.¹⁰² in Figure 5.2. The fit to the data of Zhang et al.,⁶⁰ displayed in Figure 5.1, was also extrapolated to low pressures, corresponding relatively well with the other data. Regarding the simulations, MEDFF-Refit performs the best, closely followed by MEDFF-RF and MEDFF-FF (having an identical model for the host-guest interaction). Figure 5.2 also shows that the predictions for the uptake are in worse agreement with the experiment for the generic force field than for the MEDFF-RR or MEDFF-RF. However at higher pressures all these force fields perform approximately equally well.

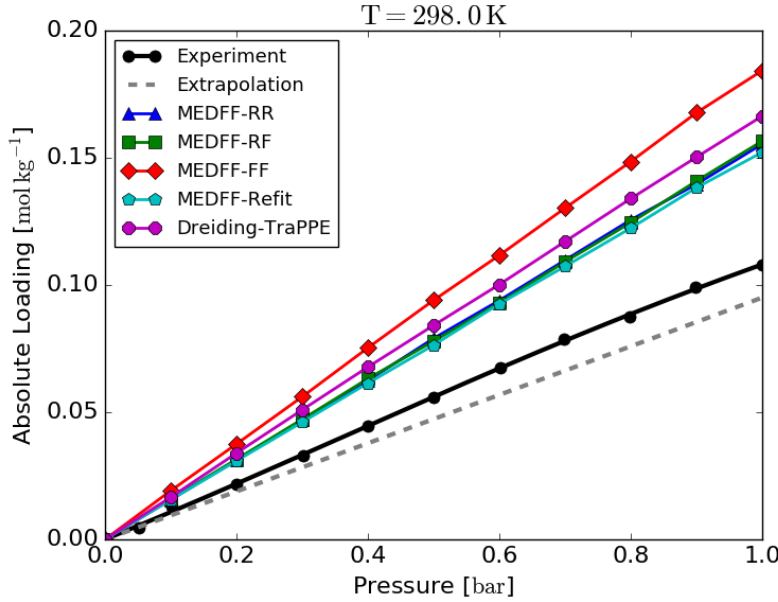


Figure 5.2: Comparison between simulated and experimental^{60, 102} adsorption isotherms for the adsorption of N₂ in ZIF-8 at 298.0 K and low pressures.

Figure 5.3 attempts to offer an explanation for the observed adsorption profiles by comparing PBE-MBDHI adsorption energies to their force field approximations for the various models under consideration. The MEDFF-RF model was not included because MEDFF-RR and MEDFF-RF have an identical parameter set for host-guest interactions and thus yield the same adsorption energies. The figure shows that for each refinement of the MEDFF, the reproduction of adsorption energies improves, *i.e.* RMSDs decrease. However, this progressive improvement is not observed for the adsorption isotherms. Indeed, while MEDFF-Refit performs better than MEDFF-RR, MEDFF-FF performs worse. There is thus no direct link between satisfactory reproduction of adsorption energies (in terms of low RMSDs) and a satisfactory reproduction of adsorption isotherms. A possible explanation for this, is the large influence of the most favourable adsorption sites. Indeed, adsorption sites with the lowest adsorption energy are filled first, thus having the largest influence on the adsorption isotherm, especially at lower pressures. If the most favourable adsorption sites are overbound, this could hence result in a significant overestimation of the uptake. The adsorption energy of the most strongly bound adsorbates is indeed overestimated more by the MEDFF-FF than by the other models. Comparing the MEDFFs to the generic force field, one observes that the DREIDING-TraPPE force field is capable of modeling the lowest interaction energies to a good degree, while for higher energies, it becomes too repulsive. For the MEDFFs on the other hand, deviations from the bisector are more homogeneously distributed. An important remark in this context is that even if the reproduction of the *ab initio* energies would be exact, the experimental isotherms would still not be reproduced exactly. On the one hand this is due to the aforementioned experimental imperfections but on the other hand also the accuracy of the *ab initio* energies forms a problem. Indeed, while DFT methods are applicable to large systems, an important sacrifice lies in the relative lack of accuracy when compared to e.g. Coupled-Cluster methods. Also, significant dif-

ferences are observed between the various dispersion correction schemes found in the literature. For instance, an RMSD of 1.81 kJ mol^{-1} was found between the *ab initio* adsorption energies, calculated in the PBE-MBDHI and PBE-D3BJ LoT.

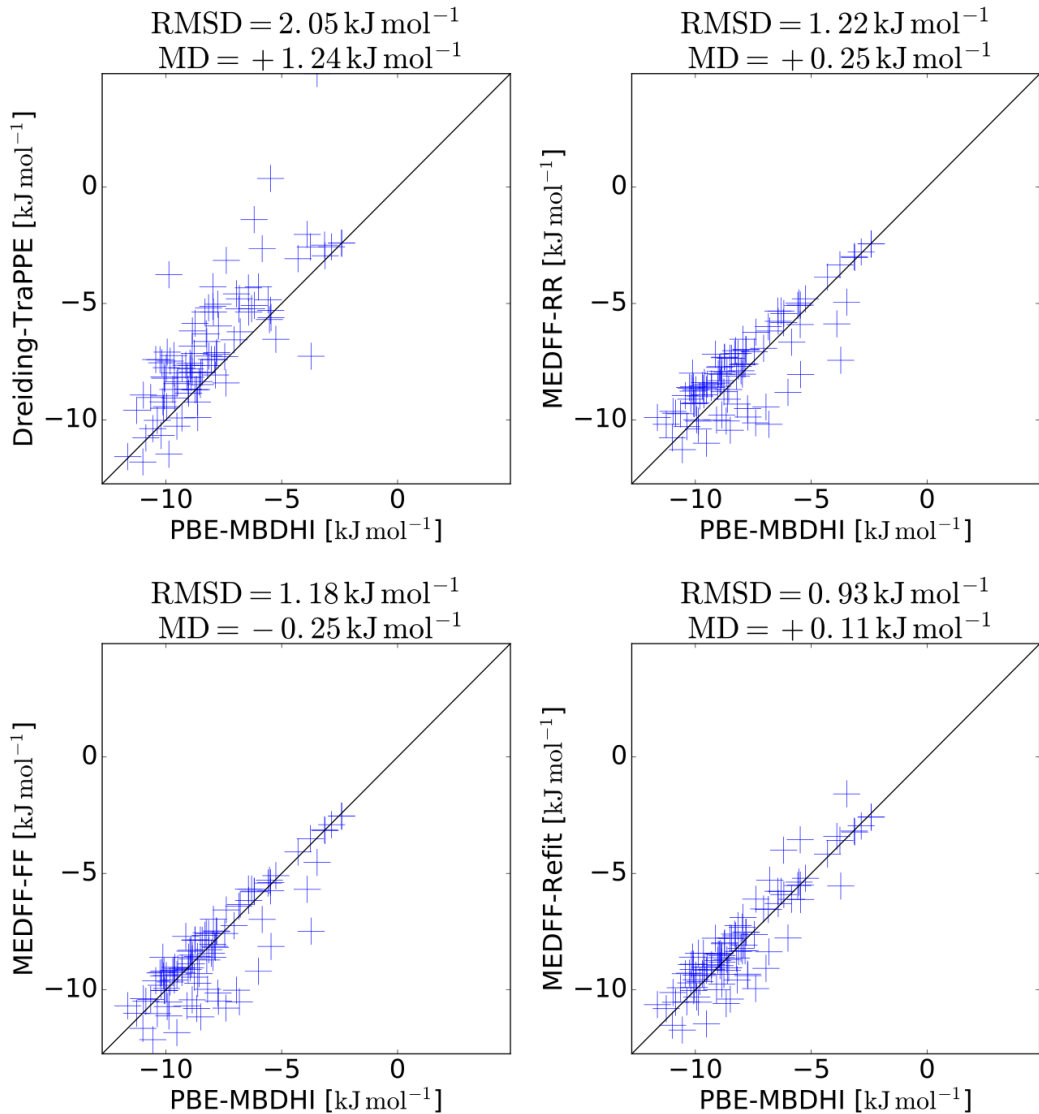


Figure 5.3: Comparison between the reproduction of *ab initio* adsorption energies by the various force field models.

5.1.2 CO₂

For the adsorption of CO₂ in ZIF-8, the framework atoms are attributed the same MBIS parameters as before. CO₂ molecules, on the other hand, are modeled by means of the rescaled charges from Table 3.7. The interaction parameters used in the various MEDFFs are listed in Table 5.2.

Force Field	host-guest				guest-guest			
	$U_{\text{exch-rep}}$	U_{ind}	U_{s8}	U_{olp}	$U_{\text{exch-rep}}$	U_{ind}	U_{s8}	U_{olp}
MEDFF-RR	8.43	-0.86	0.57	7.57	8.43	-0.86	0.57	7.57
MEDFF-RF	8.43	-0.86	0.57	7.57	7.44	-0.93	1.37	6.51
MEDFF-FF	8.45	-1.00	1.27	7.45	7.44	-0.93	1.37	6.51
MEDFF-Refit	9.86	-0.98	1.70	8.88	7.44	-0.93	1.37	6.51

Table 5.2: Interaction parameters (in a.u.) for the various MEDFF models describing CO₂ adsorption in ZIF-8.

Simulated adsorption isotherms are compared to the experiment⁶⁰ in Figure 5.4 and Appendix C. For the two most rudimentary MEDFF models (MEDFF-RR and MEDFF-RF) adsorption is underestimated at low pressures, implying that reference interaction parameters are too repulsive for the host-guest interaction. Indeed, while experimental imperfections are expected to reduce the adsorption, the simulated adsorption isotherm is located even lower for these force fields. Increasing the pressure, the uptake predicted by the MEDFF-RF increases, overestimating the experimental adsorption. The other MEDFF models, as well as the generic force field, overestimate the adsorption for all pressures.

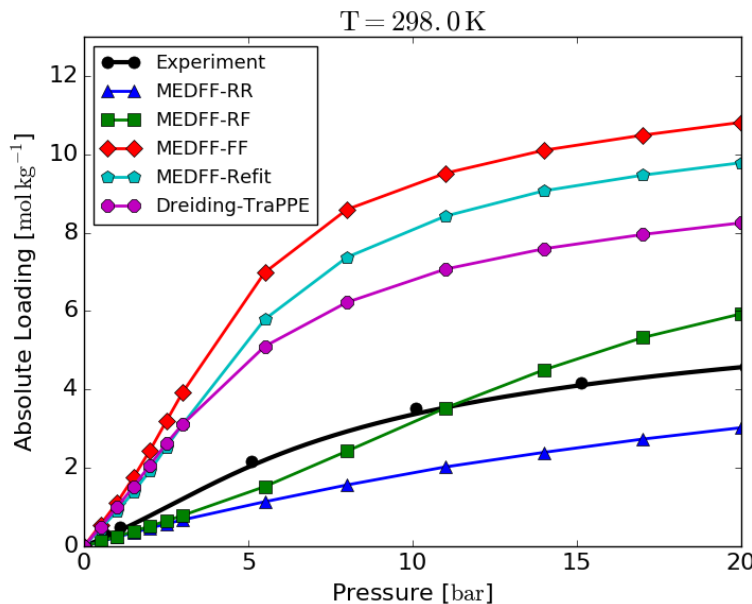


Figure 5.4: Comparison between simulated and experimental⁶⁰ adsorption isotherms for the adsorption of CO₂ in ZIF-8 at 298.0 K. Adsorption isotherms for other temperatures can be found in Appendix C.

In Figure 5.5 simulated and experimental adsorption energies are compared at low pressures. As was the case for N₂ adsorption in ZIF-8, the data reported by McEwen et al.¹⁰² were used for this pressure range. However, here, a significant difference was observed between the data of McEwen et al.¹⁰² and Zhang et al.⁶⁰ This confirms that the preparation method of the sample and the imperfections related thereto have a far-reaching influence on the adsorption properties of

the nanoporous material. Nevertheless, both experiments indicate that the reference interaction parameters are indeed too repulsive for the host-guest interaction. Fitted interaction parameters on the other hand overestimate the uptake and the best reproduction of the experimental Henry coefficient is found for the MEDFF-Refit.

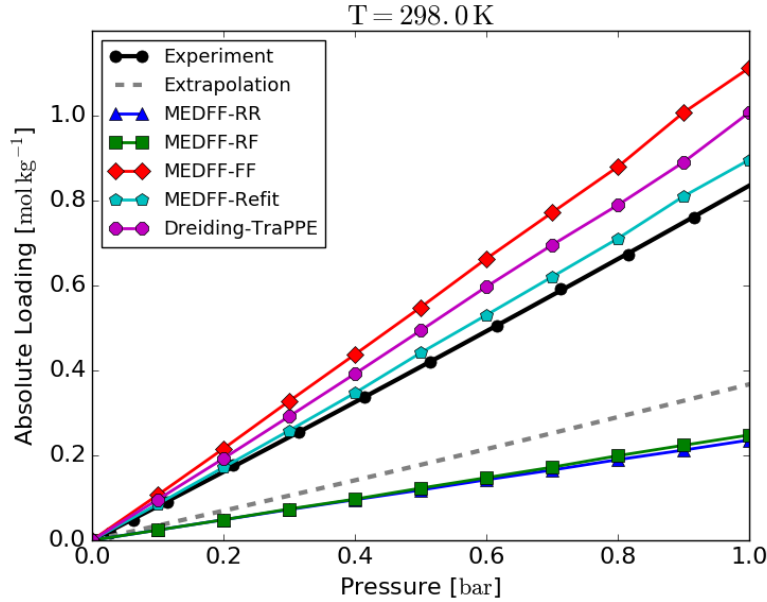


Figure 5.5: Comparison between simulated and experimental^{60, 102} adsorption isotherms for the adsorption of CO₂ in ZIF-8 at 298.0 K and low pressures.

The hypotheses proposed in the previous paragraphs are supported by comparing *ab initio* and force field adsorption energies in Figure 5.6. Indeed, the MEDFF-RR models almost all configurations too repulsive, thus explaining why adsorption is underestimated. For the other force fields, the lowest adsorption energies are only slightly underestimated. However, even these small deviations could cause the large overestimation of the adsorption isotherms, confirming that adsorption isotherms are highly sensitive to adsorption energies, especially those of the most favourable adsorption sites.

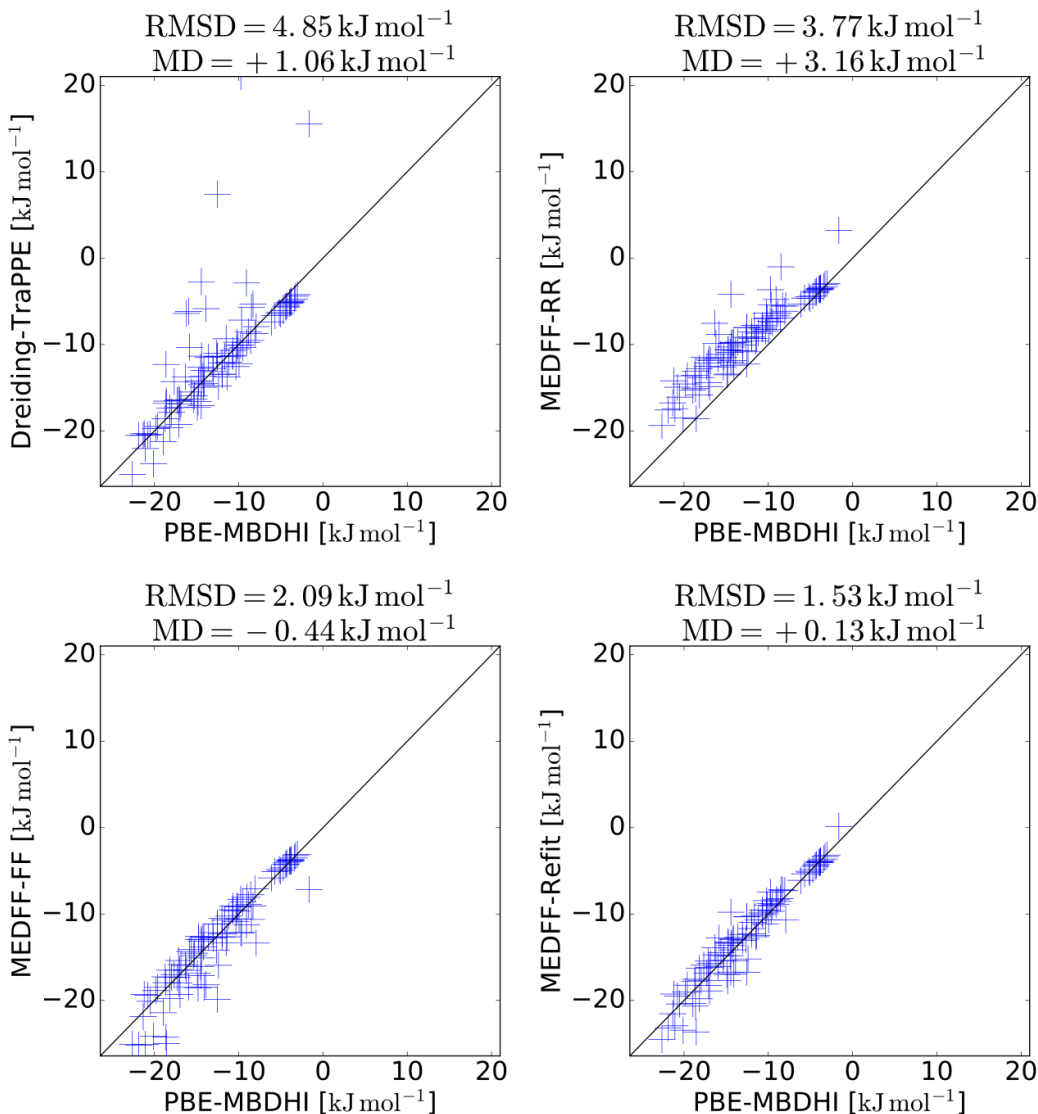


Figure 5.6: Comparison between the reproduction of *ab initio* adsorption energies by the various force field models.

5.2 MIL-53(Al)

Modeling gas adsorption in MIL-53(Al) is even more complicated than in ZIF-8 due to the breathing behaviour of the former. In the introductory chapter it was mentioned that when the temperature is not too high and CO₂ or H₂O gases are adsorbed, the framework initially is in the large pore phase for low gas pressures after which it is pulled together by the adsorbates, forming a narrow pore structure. Finally, when the pressure in the adsorbed gas is even higher, the material transforms back to its large pore phase.^{50,57} Since the methods discussed in this work only consider rigid frameworks, these transitions will not be reproduced by the GCMC simulations. However, adsorption isotherms can be simulated in the large and narrow pore phases separately and can hence be used to approximate the experimental isotherms. Adsorption of CO₂ at lower temperatures is therefore studied for both the narrow and large pore phase.

For higher temperatures and for the adsorption of N₂, no breathing is observed and thus only adsorption in the large pore phase is considered.

Regarding GCMC simulations, the typical settings are similar to those for the adsorption in ZIF-8. Each simulation consists of an equilibration run of 10 000 cycles, a production run of 50 000 cycles, chemical potentials are modeled via the Peng-Robinson equation of state and the cut-off for van der Waals interactions was set to 14.0 Å. System volumes are therefore built up by 5x2x3 unit cells for the large pore structure and by 2x4x5 unit cells for the narrow pore structure. Furthermore, the same five force field models are considered and compared to the experimental isotherms recorded by Mandal et al.⁵⁰

5.2.1 N₂

For the simulation of N₂ adsorption in MIL-53(Al), the calculation of MBIS parameters was based on electron densities determined in the PBE-D3BJ LoT for the framework and B3LYP/aug-cc-pVTZ LoT for the adsorbates. No charges corrections were applied. The various sets of interaction parameters are listed in Table 5.3.

Force Field	host-guest				guest-guest			
	$U_{\text{exch-rep}}$	U_{ind}	U_{s8}	U_{olp}	$U_{\text{exch-rep}}$	U_{ind}	U_{s8}	U_{olp}
MEDFF-RR	8.43	-0.86	0.57	7.57	8.43	-0.86	0.57	7.57
MEDFF-RF	8.43	-0.86	0.57	7.57	9.0	-0.47	0.82	8.53
MEDFF-FF	9.42	-0.76	0.98	8.66	9.00	-0.47	0.82	8.53
MEDFF-Refit	9.30	-0.76	0.74	8.54	9.00	-0.47	0.82	8.53

Table 5.3: Interaction parameters (in a.u.) for the various MEDFF models describing N₂ adsorption in MIL-53(Al).

Simulated and experimental adsorption isotherms for the adsorption of N₂ in MIL-53(Al) are displayed in Figure 5.7 and Appendix C. MEDFF-RR, MEDFF-RF and MEDFF-FF all give comparable results, implying on the one hand that fitting host-guest interaction parameters has a limited influence on the model and on the other hand that guest-guest interactions only play a secondary role. Indeed, although significant differences were observed for the simulation of N₂ VLCCs by MEDFFs with reference and fitted interaction parameters, there is only a small difference between MEDFF-RR and MEDFF-RF, even for higher pressures. As was the case for N₂ adsorption in ZIF-8, this is due to the relatively small uptake of N₂ by the framework at the considered pressures, which means that adsorbate densities are much lower compared to the VLCC simulations. By refitting the host-guest interaction parameters, the force field becomes significantly more repulsive, resulting in an adsorption isotherm that coincides almost exactly with the experimental curve. The DREIDING-TraPPE force field on the other hand overestimates the adsorption greatly for all pressures indicating that especially the host-guest interaction, modeled by the DREIDING force field is too attractive. Similar results were found for the adsorption in ZIF-8. In the work of Garcia-Perez et al.¹⁰³ on the other hand, it was found that the DREIDING force field underestimated the adsorption in NH₂-MIL-53(Al). However,

in these simulations Mulliken charges were used instead of MBIS charges. This could explain the observed differences.

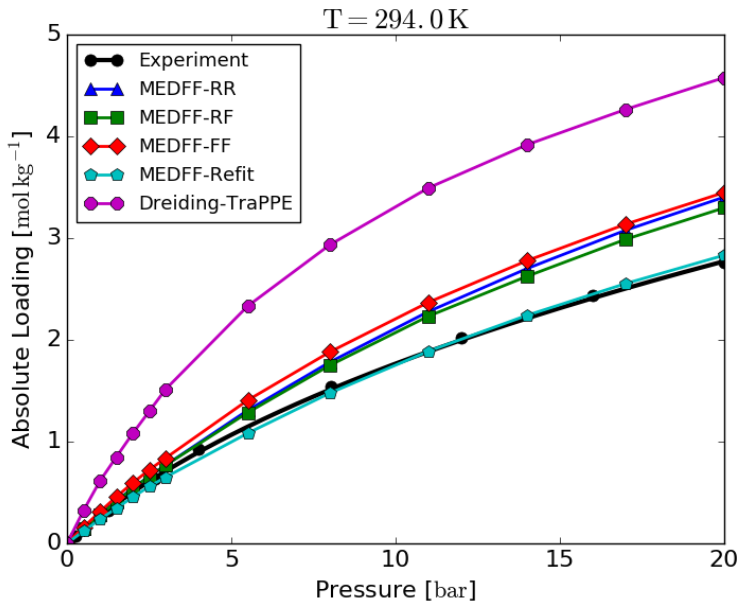


Figure 5.7: Comparison between simulated and experimental⁵⁰ adsorption isotherms for the adsorption of N₂ in MIL-53(Al) at 294.0 K. Adsorption isotherms for other temperatures can be found in Appendix C.

In the absence of accurate experimental data for the adsorption isotherms at low pressures, simulations were compared to an extrapolation of the fit proposed by Mandal et al.⁵⁰ in Figure 5.8. While this fit considers pressures up to 25 bar, some low pressure data points are included as well and therefore the fit can also be used in the low pressure range. As in Figure 5.7, the generic force field overestimates the adsorption substantially while the MEDFF models perform significantly better.

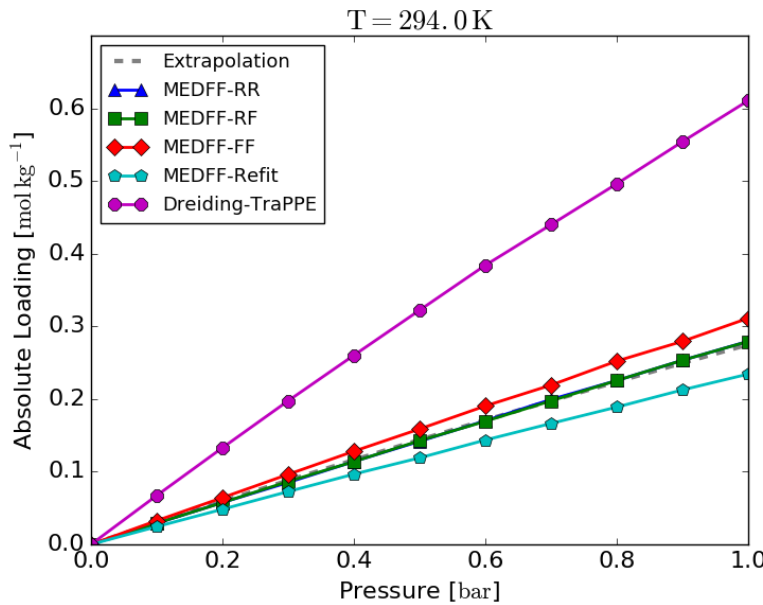


Figure 5.8: Comparison between simulated and experimental⁵⁰ adsorption isotherms for the adsorption of N₂ in MIL-53(Al) at 294.0 K and low pressures.

Figure 5.9 confirms that the DREIDING force field is way too attractive. Indeed, almost all adsorption energies are more attractive than the reference values. For the MEDFF models the correspondence is better and, as was observed for the adsorption isotherms, fitting host-guest interaction parameters only has a limited influence. A more substantial improvement (in terms of the RMSD) is found when the host-guest parameters are refitted to the *ab initio* adsorption energies.

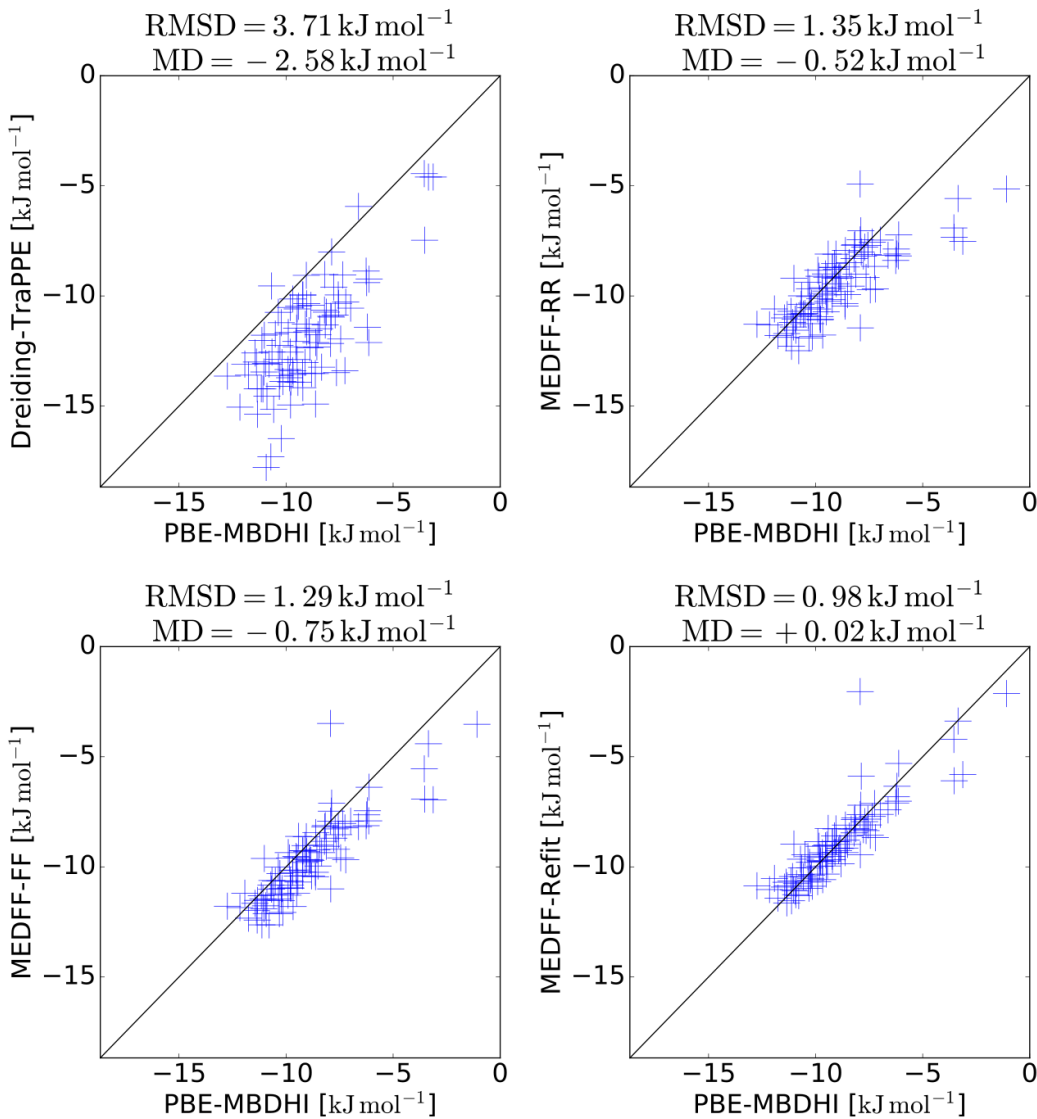


Figure 5.9: Comparison between the reproduction of *ab initio* adsorption energies by the various force field models.

5.2.2 CO₂

The MEDFF models, used to determine adsorption isotherms for CO₂ in MIL-53(Al), were parametrized with identical MBIS parameters for the framework as for the case of N₂ adsorption in MIL-53(Al). For CO₂ molecules the rescaled charges (Table 3.7) were utilised again. Because isotherms are simulated in both the large and narrow pore phases, twice as much interaction parameter sets are considered. These are displayed in Table 5.4. As was mentioned in the previous chapter, MEDFF-Refit interaction parameters differ only slightly in both phases. For the other force fields, parameters are identical by construction.

	Force Field	host-guest				guest-guest			
		$U_{\text{exch-rep}}$	U_{ind}	U_{s8}	U_{olp}	$U_{\text{exch-rep}}$	U_{ind}	U_{s8}	U_{olp}
lp	MEDFF-RR	8.43	-0.86	0.57	7.57	8.43	-0.86	0.57	7.57
	MEDFF-RF	8.43	-0.86	0.57	7.57	7.44	-0.93	1.37	6.51
	MEDFF-FF	8.60	-0.81	1.31	7.79	7.44	-0.93	1.37	6.51
	MEDFF-Refit	9.22	-0.81	1.24	8.41	7.44	-0.93	1.37	6.51
np	MEDFF-RR	8.43	-0.86	0.57	7.57	8.43	-0.86	0.57	7.57
	MEDFF-RF	8.43	-0.86	0.57	7.57	7.44	-0.93	1.37	6.51
	MEDFF-FF	8.60	-0.81	1.31	7.79	7.44	-0.93	1.37	6.51
	MEDFF-Refit	9.08	-0.81	1.31	8.27	7.44	-0.93	1.37	6.51

Table 5.4: Interaction parameters (in a.u.) for the various MEDFF models describing CO₂ adsorption in MIL-53(Al).

Figure 1.3 showed that at 350 K, no breathing is observed. Therefore, this simple case was studied first in Figure 5.10. As was the case for CO₂ adsorption in ZIF-8, both the MEDFF-RR and MEDFF-RF underestimate the adsorption, indicating that the reference parameter set is too repulsive for the host-guest interactions. By fitting host-guest interaction parameters on the other hand, adsorption is overestimated. For the refitted force field, reproduction of the experiment is almost exact. This is in accordance to the results for N₂ adsorption in MIL-53(Al) (lp). The results for the generic force field are also comparable since the uptake is greatly overestimated.

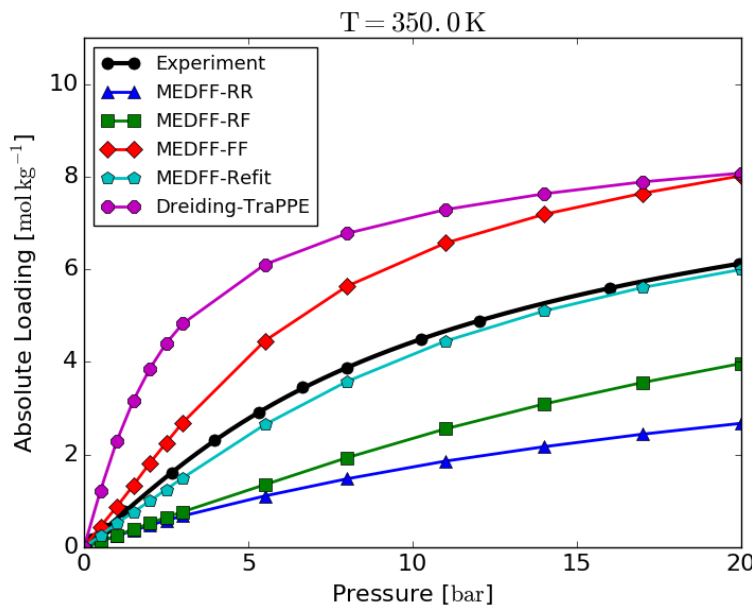


Figure 5.10: Comparison between simulated and experimental⁵⁰ adsorption isotherms for the adsorption of CO₂ in MIL-53(Al) at 350.0 K.

In Figure 5.11 adsorption isotherms are compared for lower pressures. The figure confirms that, modeling host-guest interactions with the reference parameter set, Henry coefficients are

underestimated. As for N₂, MEDFF-Refit underestimates the adsorption at lower pressures while the reproduction at higher pressures is better.

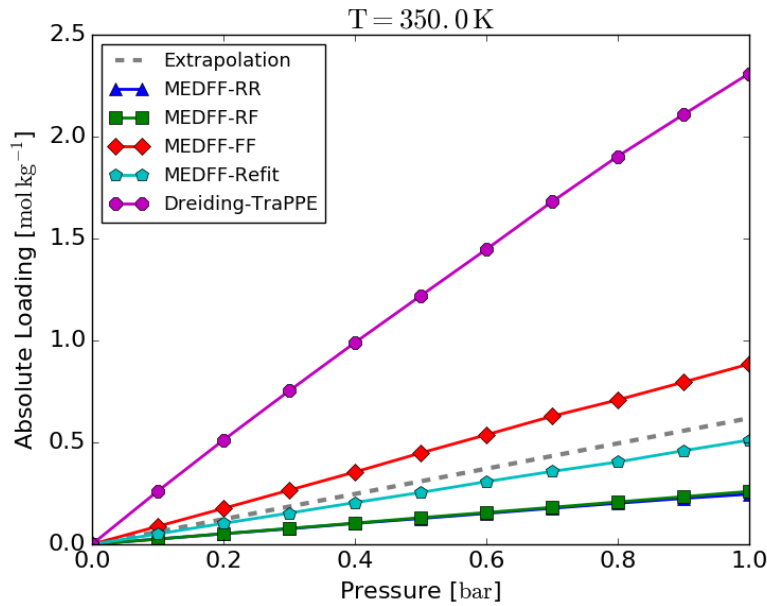


Figure 5.11: Comparison between simulated and experimental⁵⁰ adsorption isotherms for the adsorption of CO₂ in MIL-53(Al) at 350.0 K and low pressures.

Both the generic force field and MEDFF-FF underestimate the adsorption energies of almost all the considered complexes (hence the large negative MDs) (Figure 5.12). This could explain why the uptake is overestimated by these force fields. For the MEDFF-RR model on the other hand almost all adsorption energies are modeled too repulsive.

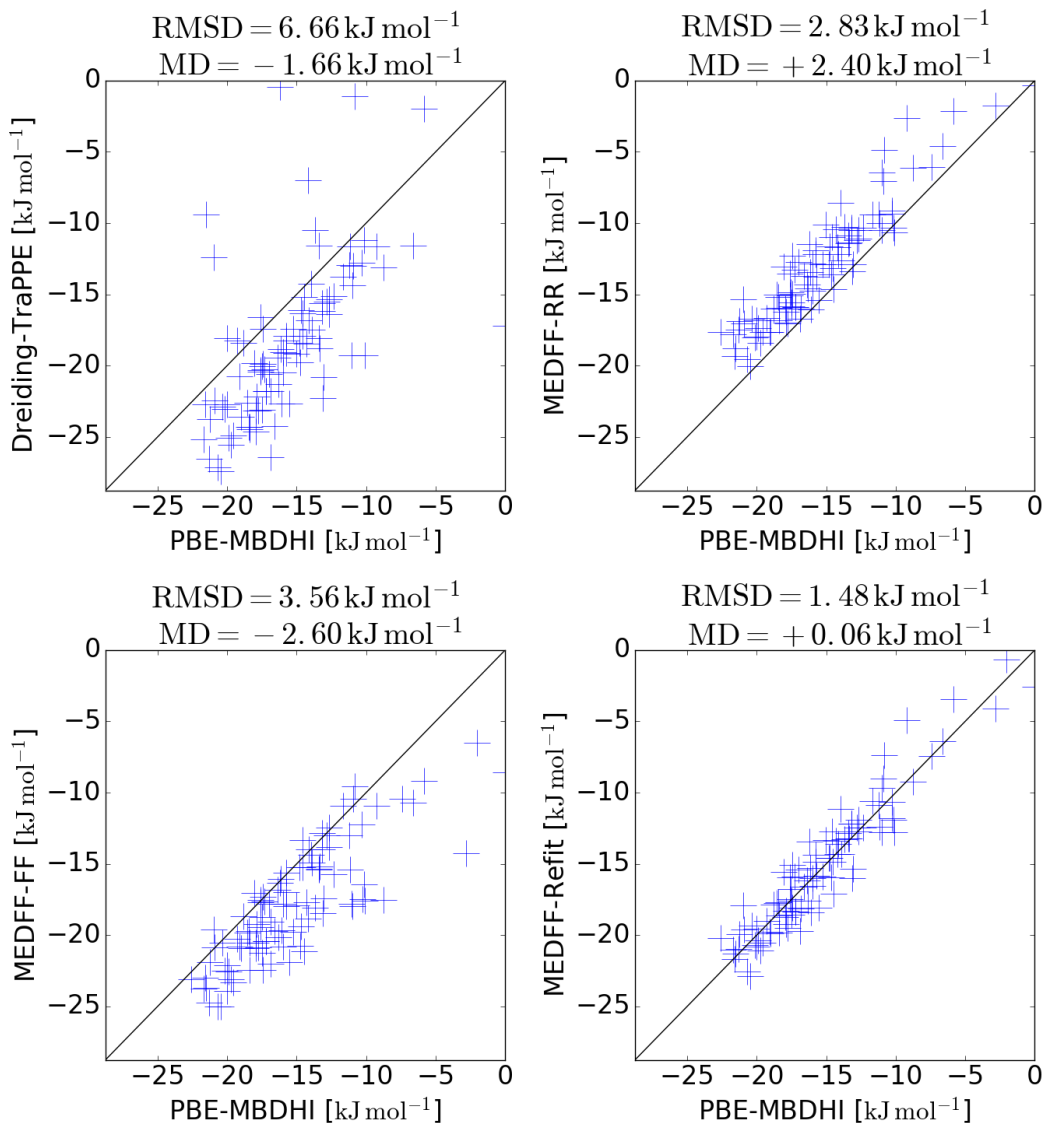


Figure 5.12: Comparison between the reproduction of *ab initio* adsorption energies by the various force field models.

The experimental adsorption isotherms of CO₂ in MIL-53(Al) at 294.0 K and 314.0 K display breathing behaviour. Therefore, adsorption simulations in both phases are compared to the experiment in Figure 5.13 and Appendix C. In the large pore pressure range, the same conclusions and remarks apply as for the case where no breathing was observed. Also in the narrow pore phase, isotherms have a similar relative position, *i.e.* MEDFF-RR and MEDFF-RF predict the lowest uptake followed by MEDFF-Refit, MEDFF-FF and DREIDING-TraPPE. However, while for the large pore phase adsorption is overestimated by the MEDFF-FF and DREIDING-TraPPE, all force fields model the uptake in the narrow pore too low.

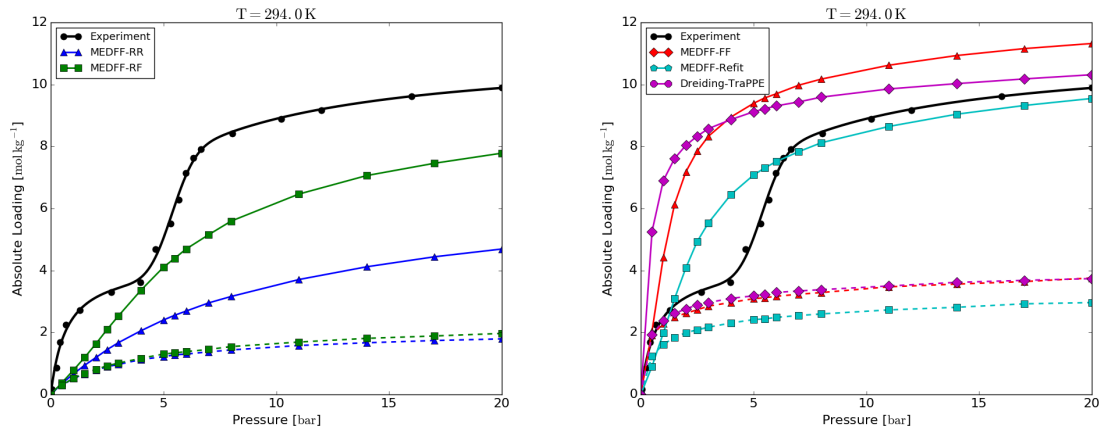


Figure 5.13: Comparison between simulated and experimental⁵⁰ adsorption isotherms for the adsorption of CO₂ in MIL-53(Al) at 294.0 K. Full lines are used for the large pore structure, dashed lines for the narrow pore structure.

Reproduction of adsorption energies in the narrow pore phase was evaluated in Figure 5.14 in order to offer an explanation for the large deviations in the corresponding adsorption isotherms. A first conclusion is that the generic force field models adsorption energies remarkably inaccurate. A possible explanation for this could be the fact that the DREIDING force field is a united-atom force field. Indeed, the approximation to treat hydrogen atoms bonded to carbon as a unit with the carbon atom, is no longer justified when adsorbates get too close to the framework and this is typically the case for adsorption in the narrow pore phase. The MEDFF-RR on the other hand, models almost all configurations too repulsive explaining why this force field yields the lowest adsorption. While the correspondence (in terms of RMSDs) is improved by fitting and refitting host-guest interaction parameters, the most favorable adsorption sites remain underbound. This could explain why all force fields underestimate the narrow pore adsorption isotherms. The deviations for these favourable adsorption sites could be caused by the fact that the same host-guest parameter set is used for the interactions with linkers and metal-oxides. Indeed, it was mentioned before that (hydrogen bonds with) the metal-oxide chains play a crucial role in the phase transition of MIL-53(Al)^{57,100} and thus have a large influence on the adsorption in the narrow pore phase. The lack of an adapted parameter set could hence explain the inaccurate model for the most favorable adsorption energies in this phase.

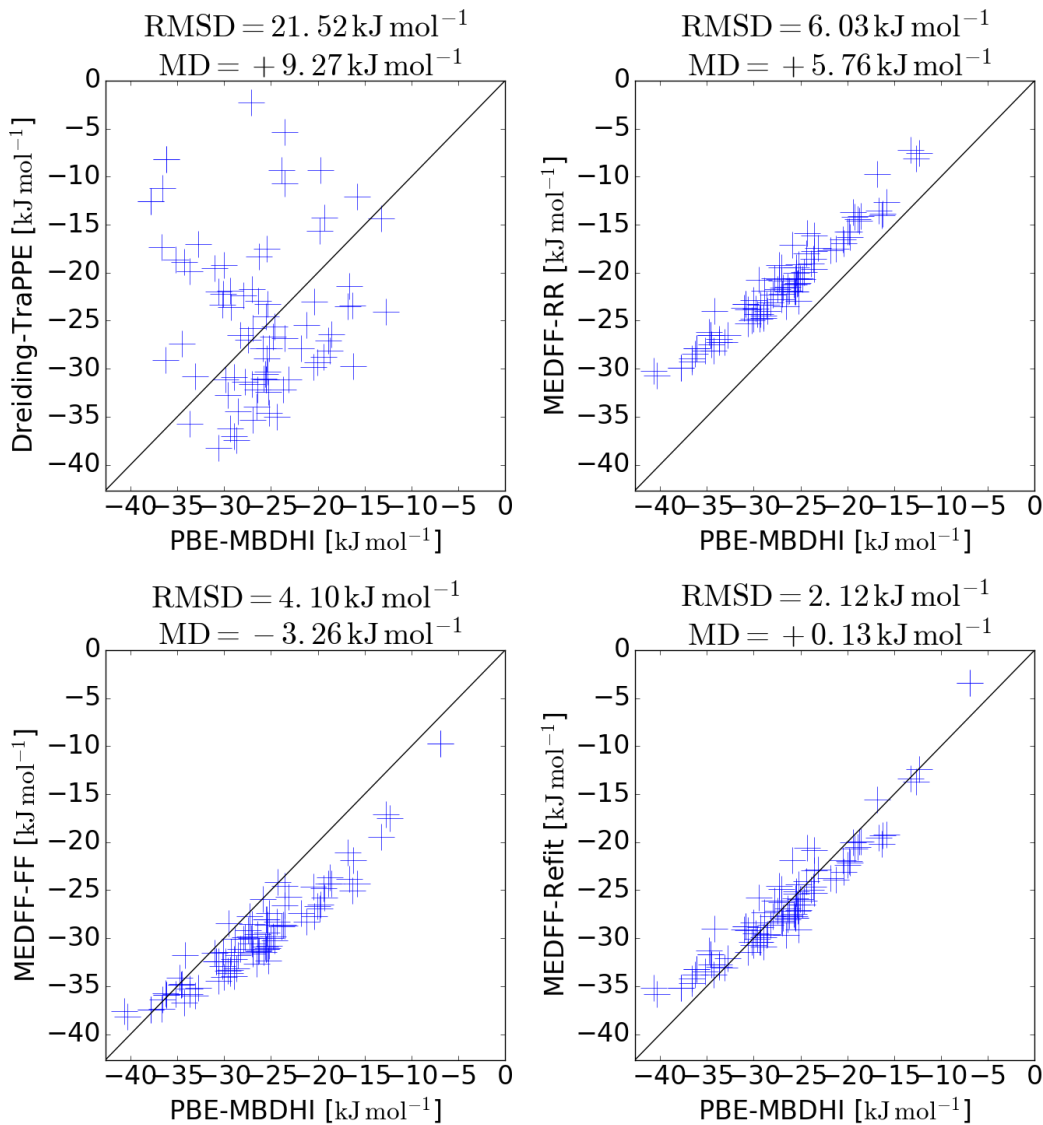


Figure 5.14: Comparison between the reproduction of *ab initio* adsorption energies by the various force field models.

Mandal et al.⁵⁰ successfully fitted a dual-site Langmuir-type model to the experimental Type IV adsorption isotherms. Herein, the transitional behaviour between both phases was modeled by a cumulative normal distribution function. This transition function can also be used to transform the narrow pore and large pore adsorption isotherms into isotherms with a gradual transition. Making use of the experimentally determined parameters, this was done for the adsorption isotherms at 294.0 K in Figure 5.15 and for the adsorption isotherms at 314.0 K in Appendix C. In this way comparison between simulation and experiment is facilitated. However, it should be noted that to obtain these adsorption isotherms empirical input is required and the resulting models are hence no longer purely *ab initio* derived. Naturally, similar remarks and conclusions as for Figure 5.13 apply here.

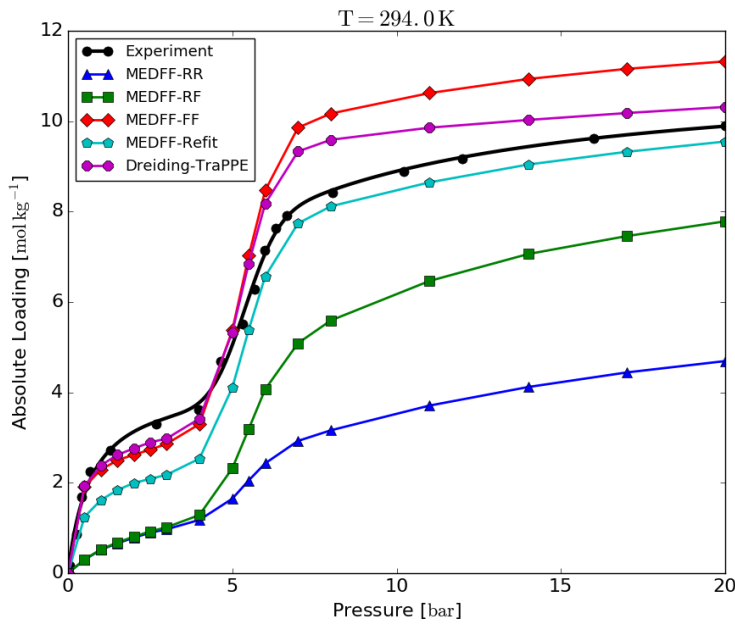


Figure 5.15: Comparison between simulated and experimental adsorption isotherms for the adsorption of CO₂ in MIL-53(Al) at 294.0 K. The transition between the large pore and narrow pore phase was regulated by the transition function proposed by Mandal et al.⁵⁰

Chapter 6

Conclusion and Outlook

In this work, a systematic force field methodology was devised to describe gas adsorption in a rigid, nanoporous host. For this purpose, non-covalent and pairwise additive Monomer Electron Density Force Fields (MEDFFs) were derived for both the host-guest interactions between the nanoporous framework and the adsorbate molecules and the mutual guest-guest interactions between the adsorbates. The MEDFF was originally developed to describe dispersion-dominated interactions between isolated molecules. In this work, we showed that the methodology can also be applied to other fluids like N₂ and CO₂ where dispersion is less dominant. The force fields were parametrized by MBIS parameters, originating from monomer electron density calculations, and by three case-specific interaction parameters, obtained by fitting the force field to *ab initio* SAPT and CCSD(T) dimer interaction energies. Various parameter sets were obtained and the corresponding force fields were validated both internally and externally. Internal validation proceeded via comparison between *ab initio* calculated dimer interaction energies and their corresponding force field approximations. While for N₂ a satisfactory reproduction was observed, significant differences were found for the electrostatic interaction in CO₂ dimers. These discrepancies were found to originate from an insufficiently accurate model for the monomer electron density. Indeed, on the one hand atomic and molecular multipoles are not reproduced by a superposition of spherically symmetric, Slater-type, atomic charge contributions, as used in the MEDFF, while on the other hand the typical exponential tails of the Slater functions are not capable to fully capture the penetration effect of the electron density. The former problem was solved to a large extent by altering the MBIS parameters so that the lowest-order *ab initio* molecular multipoles were reproduced. In this way the description of the electrostatic interaction in CO₂ was improved greatly. Regarding the internal validation, it was also found that B3LYP/aug-cc-pVTZ electron densities perform better than CCSD/aug-cc-pVTZ. The MEDFF models for N₂ and CO₂ were also validated externally by comparison with experimental second virial coefficients and vapor-liquid coexistence curves (VLCCs). Second virial coefficients have a direct link with interaction energies in dimers consisting of two molecules (*i.e.* many-body effects have no influence) and are thus expected to be reproduced accurately. This was indeed the case for both N₂ and CO₂. VLCCs on the other hand were studied because adsorbates can condense upon adsorption in a nanoporous host. In order to correctly model this behaviour, it is necessary to reproduce VLCCs describing vapor-liquid equilibria. For CO₂ the MEDFF model was slightly too attractive while for N₂ the correspondence was substantially better. Since the overbinding

of CO₂ was not observed for the second virial coefficients, a possible explanation for the unsatisfactory VLCC simulations could be the lack of many-body effects in the force field model. Indeed, other force fields (e.g. TraPPE) succeed in reproducing VLCC simulations. However, these models consist of effective pair potentials, incorporating many-body effects implicitly in pairwise terms. As a result these force fields typically fail to reproduce second virial coefficient accurately. Indeed, second virial coefficients only depend on dimer interaction energies and are therefore reproduced better by true pair potentials (like the MEDFF) than by effective pair potentials. Constructing a pairwise-additive force field model that simultaneously reproduces second virial coefficients (and thus dimer interaction energies) and VLCCs (and thus many-body effects), is therefore a Sisyphean task.

While mutual interactions between guest molecules only become important for adsorption at higher pressures, the host-guest interactions play a crucial role for all pressures. However, deriving a MEDFF for these host-guest interactions is not straightforward because SAPT and CCSD(T) energies cannot be determined for a combination of an isolated molecule and an infinite framework of atoms. In Chapter 4, this problem was solved by considering a cluster approach. Select groups of atoms, especially important for the interaction between the guest molecules and the host framework, were extracted from the lattice and terminated to yield neutral, closed-shell systems. A MEDFF was then derived for dimers, each consisting of a cluster and an adsorbate molecule. For the adsorption in ZIF-8, the considered cluster was a protonated methyl-imidazole (IZ) linker, while for the adsorption in MIL-53(Al) a BDC linker with two extra hydrogen atoms was utilised. Only considering IZ linkers is an acceptable approximation for ZIF-8 due to the tetrahedral surrounding of the zinc atoms by IZ linkers, making the zinc atoms inaccessible to guest molecules. This is not the case for MIL-53(Al) where a metal-oxide cluster should be considered in addition to the BDC linker because it was found that the bridging hydroxyl group has an important influence on the gas adsorption and breathing behaviour of this flexible framework. However, neutral closed-shell metal-oxide clusters typically require a lot of atoms, becoming too large for SAPT and CCSD(T) calculations. Therefore only the BDC linkers were considered. Accurate MEDFFs were successfully derived for all the linker-adsorbate dimers and as for N₂ and CO₂ dimers, the electrostatics contribution was modeled the worst. Therefore the charge correction scheme, developed for CO₂, was extended and applied to the linkers as well. However, the influence of the corrections was relatively limited due to the uncorrected penetration effect and the fact that molecular dipoles are already reproduced quite accurately by the MBIS charges.

In addition to the cluster model approach, a second fitting procedure was devised to determine host-guest interaction parameters, based on adsorption energies in periodic structures. These are the differences between the energy of a framework with one adsorbate molecule in each unit cell and the energies of the empty framework and the guest molecules separately. Where adsorbates are located during adsorption in a nanoporous host is completely determined by these adsorption energies at low pressures. A good reproduction of *ab initio* adsorption energies is thus vital for describing adsorption at the atomic level and for reproducing experimental isotherms for the right reasons. Especially the lowest adsorption energies should be reproduced since the corresponding adsorption sites are filled first and are thus the most important for adsorption

at lower pressures. Refitting host-guest interaction parameters by means of adsorption energies was performed for all combinations of adsorbates and frameworks. For the adsorption of CO₂ in MIL-53(Al) both the large pore and narrow pore phase were considered because of the experimentally observed breathing behaviour of the framework upon CO₂ adsorption. Interaction parameters, fitted in the cluster model, were taken as a reference and in all cases the refit resulted in a significant reduction in the RMSD between *ab initio* and force fields adsorption energies.

In Chapter 5, the MEDFF models developed in the previous chapters were used to simulate adsorption isotherms by means of Monte Carlo simulations in the grand-canonical ensemble. Results were compared to simulations with the generic DREIDING-TraPPE force field and to experimental data. Even though fitting and especially refitting of the interaction parameters improved the model, reproduction was not particularly outstanding. Also the generic force field was not able to reproduce experimental data. A first explanation for the observed deviations is the imperfect nature of the samples used in experimental setups. Surface effects, lattice imperfections and impurities all play an important role, typically reducing the uptake. Also the influence of the most favourable adsorption sites should not be underestimated. Small differences in the potential energies surface, especially close to the minima, can result in large differences in the uptake. Indeed, while the MEDFF-Refit model typically succeeds in reducing the RMSDs on *ab initio* adsorption energies, this force field is not capable to systematically reproduce experimental adsorption isotherms. In other words, satisfactory reproduction of adsorption energies (in terms of a low RMSD) is no sufficient condition for satisfactory reproduction of adsorption isotherms. A possible solution, taking into account the importance of the most favourable adsorption sites, could be a weighted fit where the lowest adsorption energies have an increased weight. Even though this could improve the reproduction of the lowest *ab initio* adsorption energies, the accuracy of these *ab initio* methods also forms a problem. Indeed, *ab initio* adsorption energies can only be calculated by means of dispersion-corrected DFT methods due to high number of atoms involved. However, the relative differences between the various dispersion correction schemes as well as the intrinsic lack of accuracy in DFT methods makes that even *ab initio* adsorption energies should be treated carefully. Indeed, even if it were computationally feasible to perform GCMC simulations where energy differences were calculated by means of *ab initio* DFT methods, reproduction of experimental adsorption isotherms would still not be guaranteed. Finally, also effects originating from framework flexibility should be considered. Indeed, in addition to the global phase transitions discussed before, local (normal mode) vibrations and effects like gate-opening can have an important influence on the adsorption. Significant deviations could thus be caused by the fact that framework flexibility is completely neglected in the considered model. Also the exact shape and volume of the rigid unit cell used to perform adsorption simulations in, have a far-reaching influence on the gas uptake.

In conclusion, one could say that the main goal of this work, extending the MEDFF methodology to describe gas adsorption in nanoporous materials, was achieved successfully. Via cluster models and adsorption energies, the model was also tuned to be more representative in these applications. Systematic reproduction of experimental adsorption isotherms on the other hand

was not achieved. However it was found that the level of accuracy, required to reach this goal, is almost unattainable by force fields. This also places previously performed reparametrizations of force fields, especially for adsorption, in perspective. Indeed, while adapted parameter sets may be capable to reproduce experimental adsorption isotherms exactly, these are rather lucky shots than models that accurately capture the details of adsorption process.

Appendix A

MBIS Parameters for IZ and BDC Clusters

Atom	original parameters				corrected parameters				corrections
	q_{tot}	q_c	q_v	σ_v	q_{tot}	q_c	q_v	σ_v	
H	0.15	1.00	-0.85	0.38	0.16	1.01	-0.85	0.38	0.01
H	0.14	1.00	-0.86	0.38	0.10	0.96	-0.86	0.38	-0.04
C	-0.17	4.33	-4.50	0.52	-0.22	4.28	-4.50	0.52	-0.05
C	0.01	4.34	-4.33	0.51	0.14	4.47	-4.33	0.51	0.13
N	-0.42	5.37	-5.79	0.44	-0.55	5.24	-5.79	0.44	-0.13
N	-0.54	5.35	-5.89	0.46	-0.63	5.26	-5.89	0.46	-0.09
H	0.36	1.00	-0.64	0.35	0.42	1.06	-0.64	0.35	0.06
C	0.55	4.35	-3.80	0.47	0.59	4.40	-3.80	0.47	0.04
C	-0.57	4.35	-4.92	0.52	-0.12	4.80	-4.92	0.52	0.45
H	0.15	1.00	-0.85	0.38	0.01	0.86	-0.85	0.38	-0.14
H	0.16	1.00	-0.84	0.38	0.03	0.87	-0.84	0.38	-0.13
H	0.19	1.00	-0.81	0.37	0.06	0.87	-0.81	0.37	-0.13

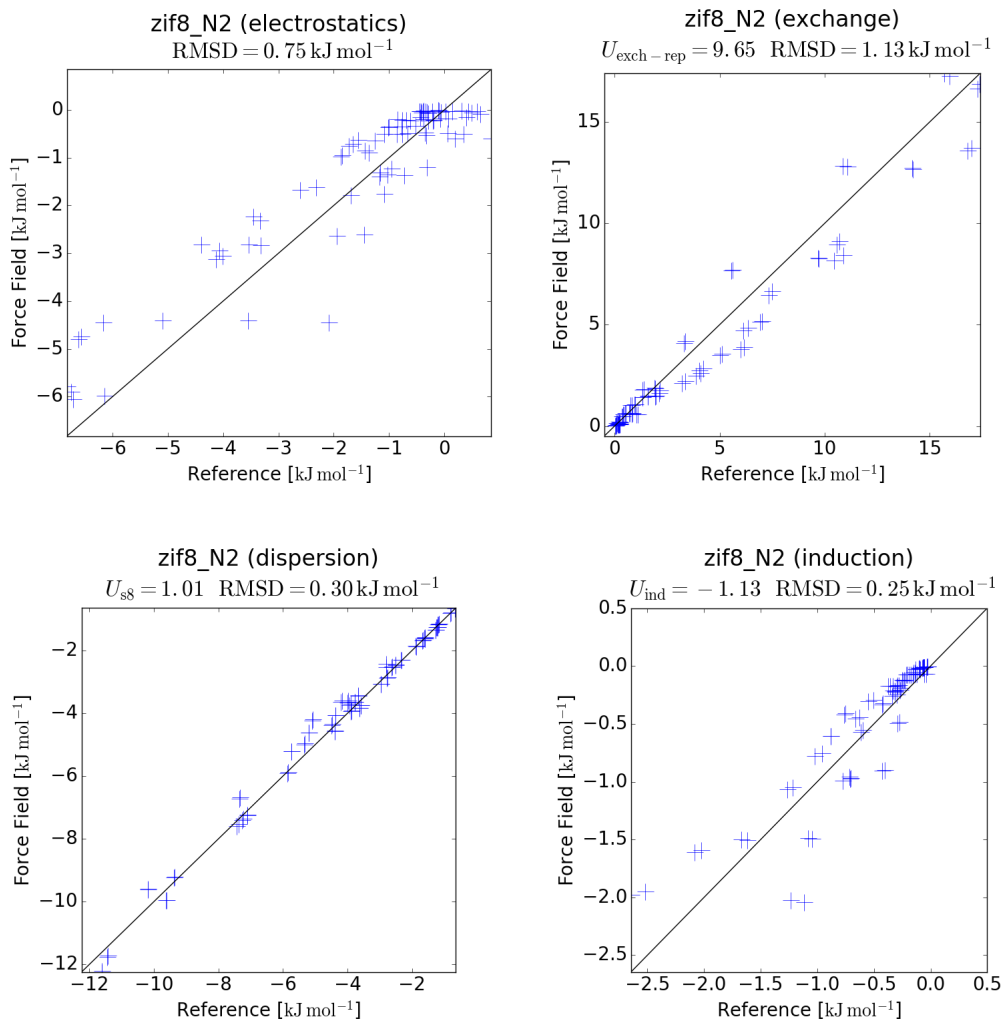
Table A.1: MBIS parameters of IZ (in a.u.) in the B3LYP/aug-cc-pVTZ level of theory. Atoms are ordered from bottom to top according to Figure 4.2.

Atom	original parameters				corrected parameters				corrections
	q_{tot}	q_c	q_v	σ_v	q_{tot}	q_c	q_v	σ_v	
H	0.46	1.00	-0.54	0.35	0.43	0.97	-0.54	0.35	-0.03
O	-0.64	6.35	-6.99	0.41	-0.62	6.38	-6.99	0.41	0.02
O	-0.55	6.39	-6.94	0.39	-0.51	6.43	-6.94	0.39	0.04
C	0.77	4.34	-3.56	0.47	0.74	4.30	-3.56	0.47	-0.03
C	-0.13	4.36	-4.49	0.50	-0.17	4.32	-4.49	0.50	-0.04
H	0.16	1.00	-0.84	0.38	0.12	0.96	-0.84	0.38	-0.04
H	0.14	1.00	-0.86	0.38	0.13	0.99	-0.86	0.38	-0.01
C	-0.09	4.35	-4.44	0.50	0.01	4.46	-4.44	0.50	0.10
C	-0.12	4.35	-4.47	0.51	-0.12	4.35	-4.47	0.51	0.00
C	-0.13	4.35	-4.48	0.51	-0.15	4.33	-4.48	0.51	-0.02
C	-0.10	4.35	-4.45	0.50	-0.02	4.43	-4.45	0.50	0.08
H	0.14	1.00	-0.86	0.38	0.13	0.97	-0.86	0.38	-0.01
H	0.16	1.00	-0.84	0.38	0.13	0.99	-0.84	0.38	-0.03
C	-0.12	4.36	-4.48	0.50	-0.14	4.34	-4.48	0.50	-0.02
C	0.77	4.33	-3.57	0.47	0.72	4.29	-3.57	0.47	-0.05
O	-0.55	6.39	-6.94	0.39	-0.51	6.43	-6.94	0.39	0.04
O	-0.64	6.35	-6.99	0.41	-0.61	6.38	-6.99	0.41	0.03
H	0.46	1.00	-0.54	0.35	0.43	0.97	-0.54	0.35	-0.03

Table A.2: MBIS parameters of BDC (in a.u.) in the B3LYP/aug-cc-pVTZ level of theory. Atoms are ordered from left to right according to the Figure 4.10.

Appendix B

MEDFF Performance for Clusters



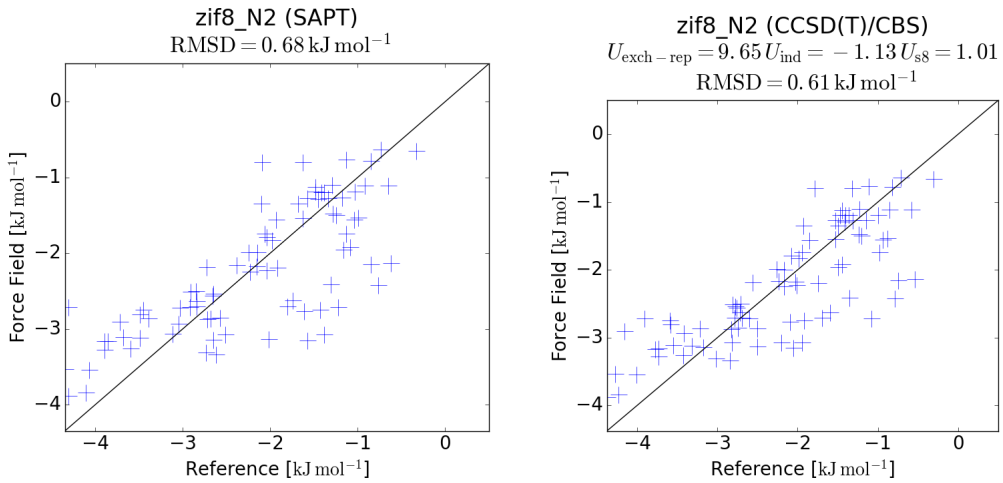


Figure B.1: Evaluation of the performance of the MEDFF for IZ-N₂ with DP = 10% and corrected charges.

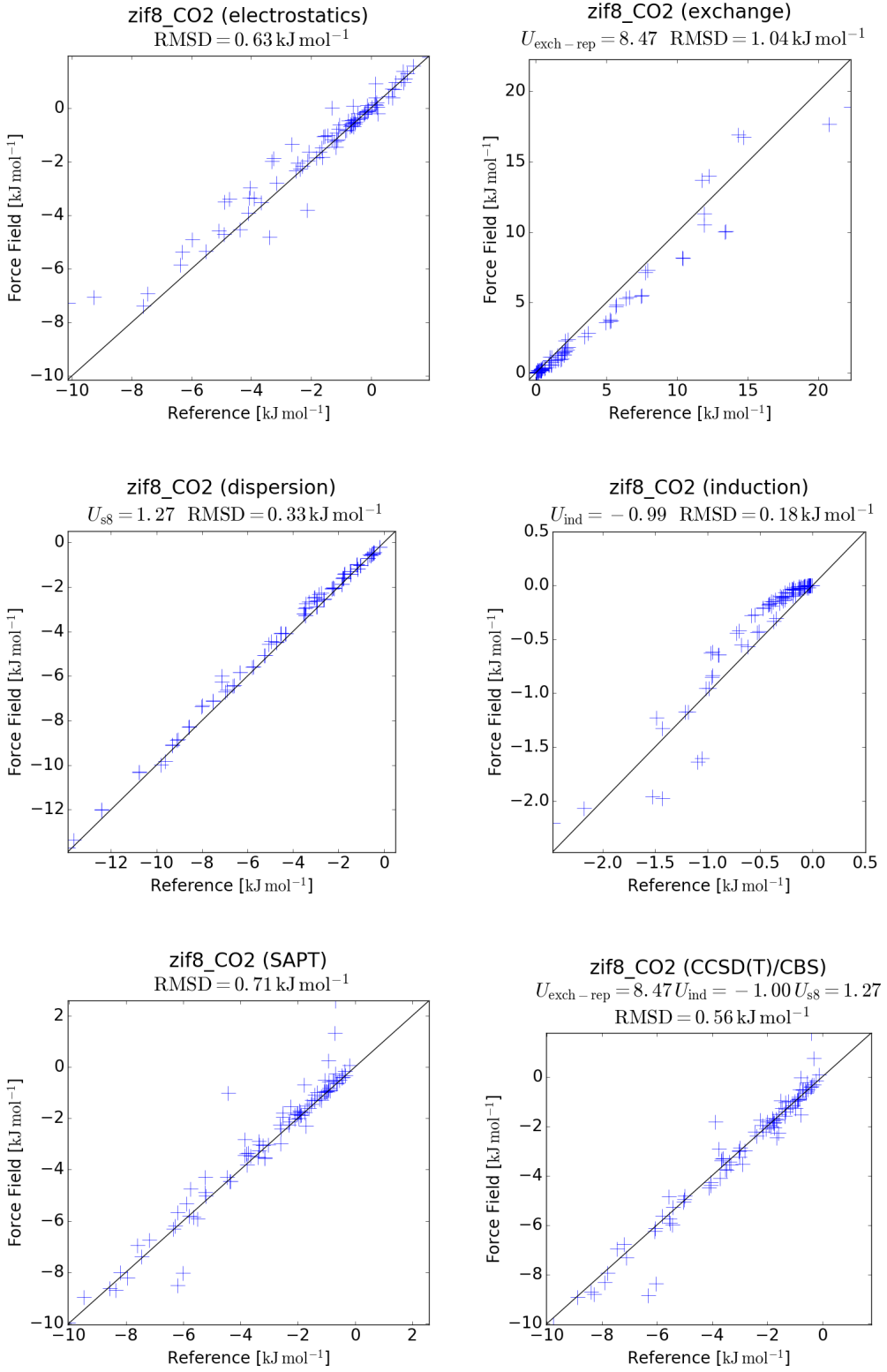


Figure B.2: Evaluation of the performance of the MEDFF for IZ-CO₂ with DP = 20% and corrected charges.

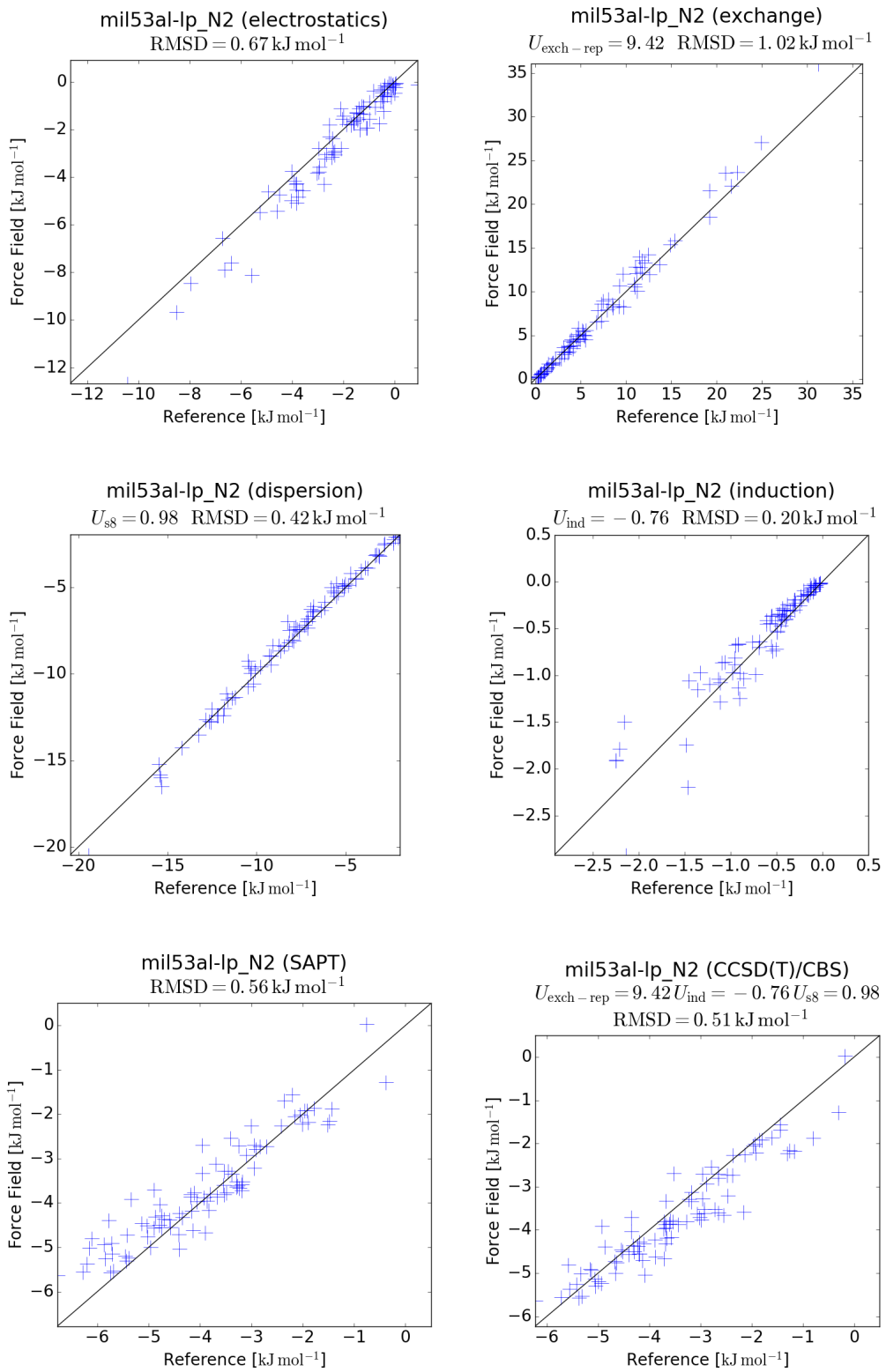


Figure B.3: Evaluation of the performance of the MEDFF for BDC-N₂ with DP = 10% and corrected charges.

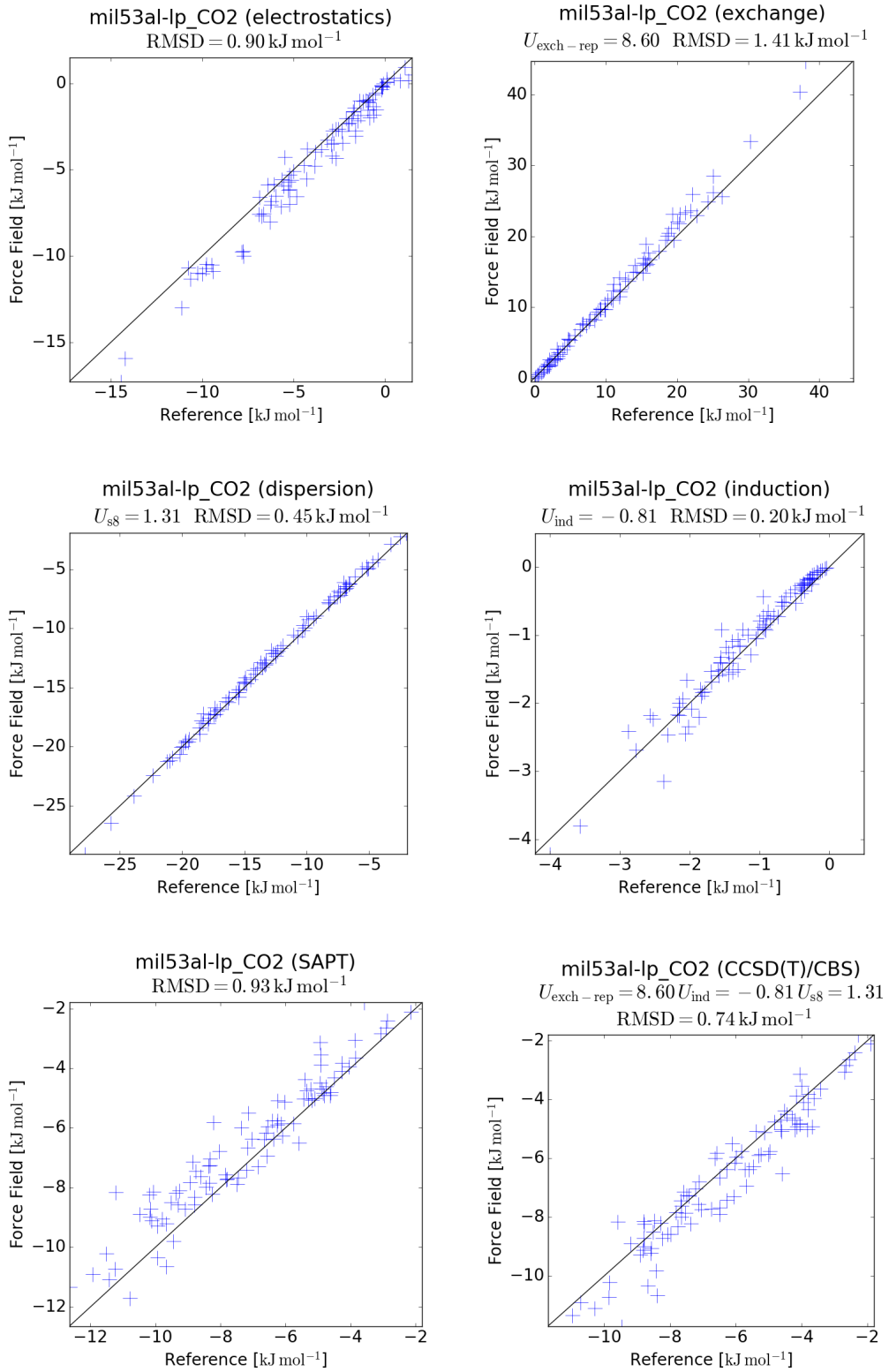


Figure B.4: Evaluation of the performance of the MEDFF for BDC-CO₂ with DP = 10% and corrected charges.

Appendix C

Supplementary Adsorption Isotherms

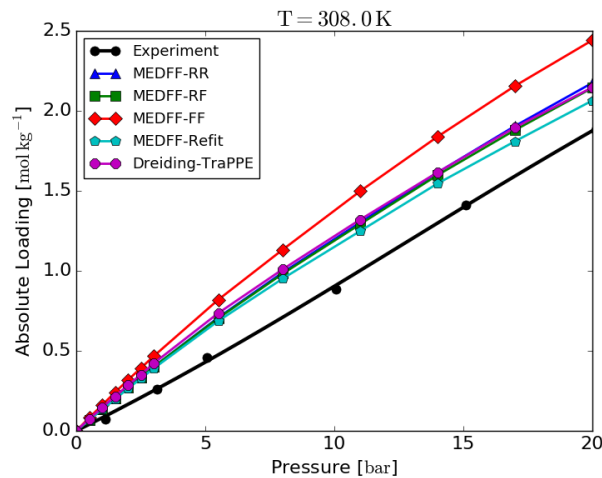


Figure C.1: Adsorption isotherms for the adsorption of N₂ in ZIF-8 at 308.0 K.

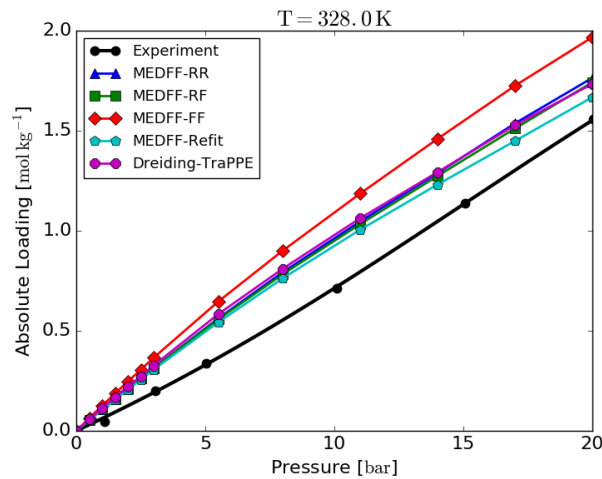


Figure C.2: Adsorption isotherms for the adsorption of N₂ in ZIF-8 at 328.0 K.

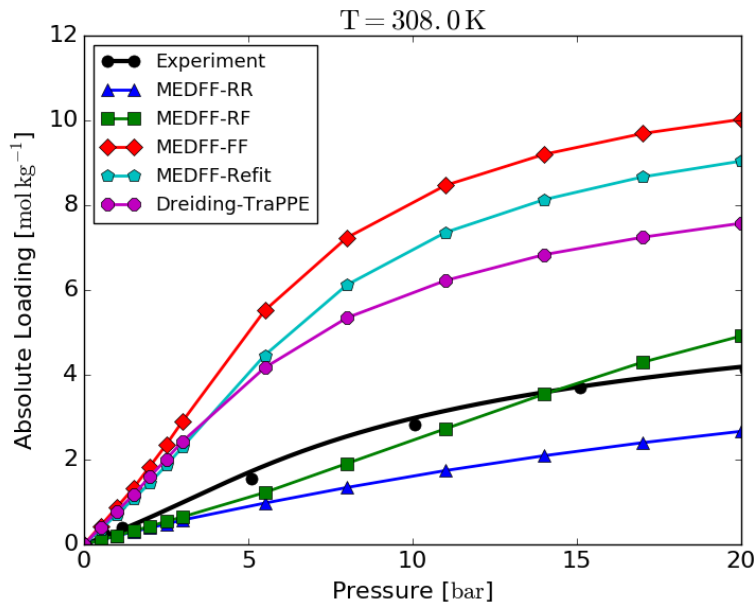


Figure C.3: Adsorption isotherms for the adsorption of CO₂ in ZIF-8 at 308.0 K.

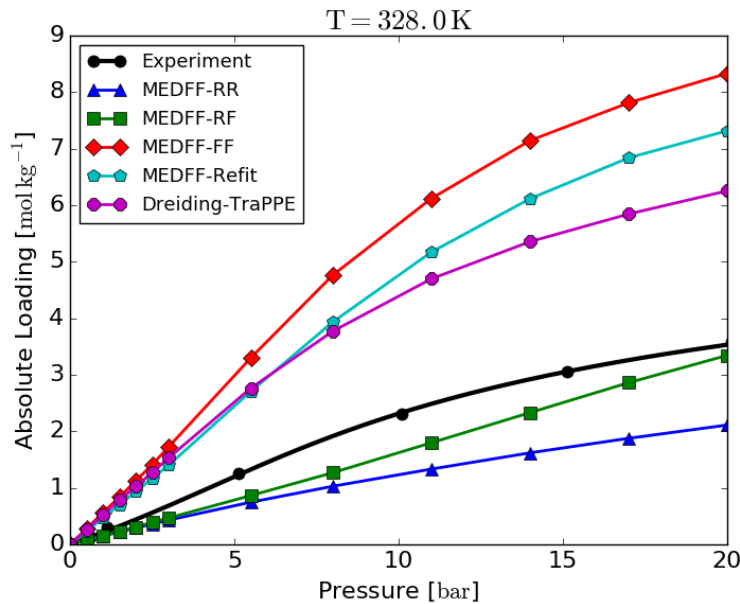


Figure C.4: Adsorption isotherms for the adsorption of CO₂ in ZIF-8 at 328.0 K.

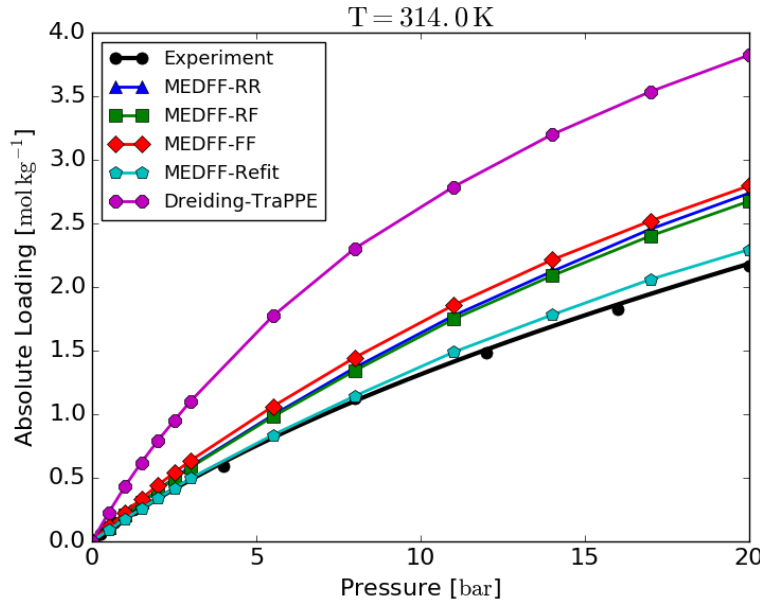


Figure C.5: Adsorption isotherms for the adsorption of N_2 in MIL-53(Al) at 314.0 K.

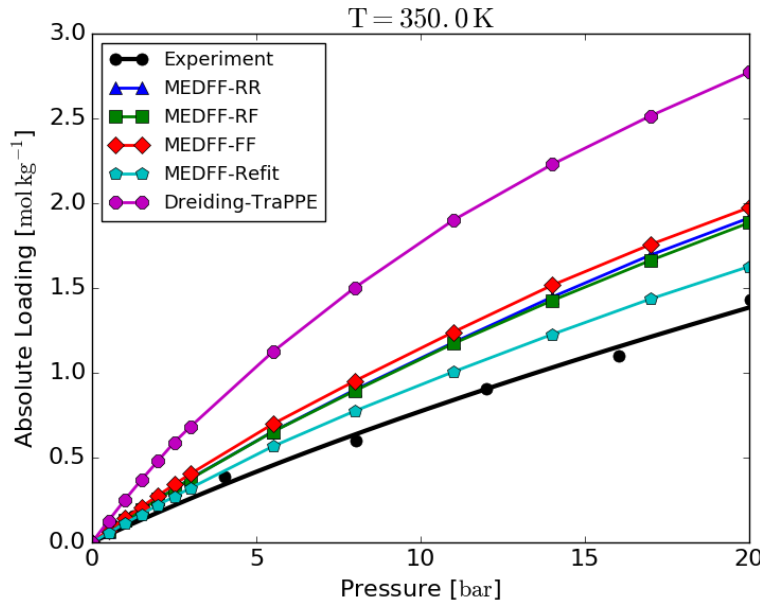


Figure C.6: Adsorption isotherms for the adsorption of N_2 in MIL-53(Al) at 350.0 K.

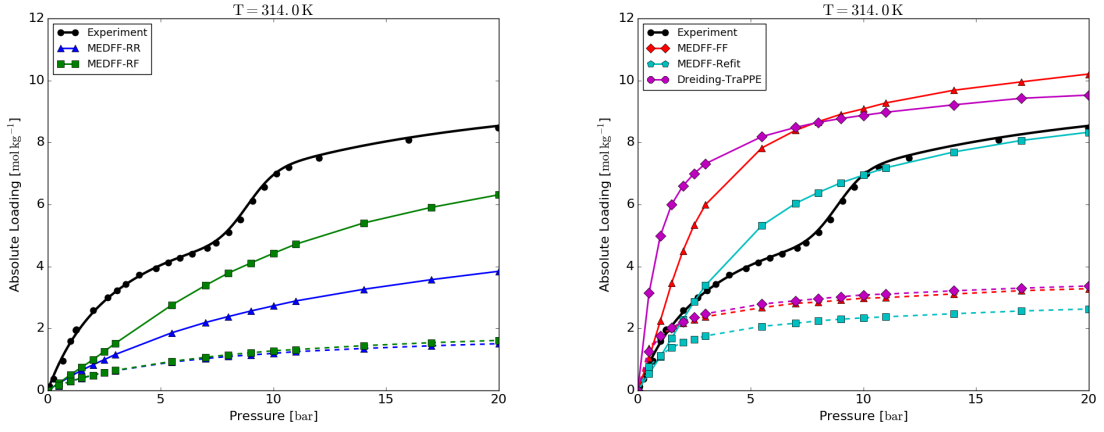


Figure C.7: Adsorption isotherms for the adsorption of CO_2 in MIL-53(Al) at 314.0 K. Full lines are used for the large pore structure, dashed lines for the narrow pore structure.

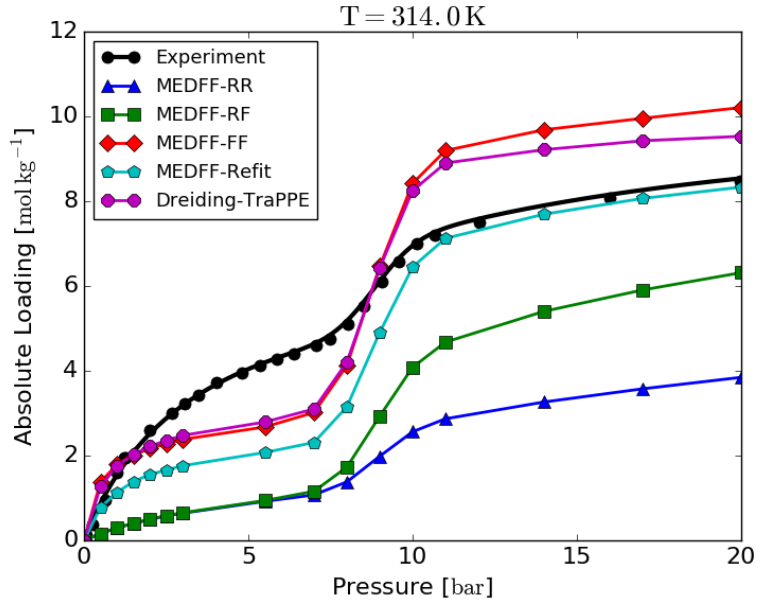


Figure C.8: Adsorption isotherms for the adsorption of CO_2 in MIL-53(Al) at 314.0 K. The transition between the large pore and narrow pore phase was regulated by the transition function proposed by Mandal et al.⁵⁰

Bibliography

- [1] Mark E. Davis. Ordered Porous Materials for Emerging Applications. *Nature*, 417(6891):813–821, June 2002.
- [2] Susumu Kitagawa, Ryo Kitaura, and Shin-ichiro Noro. Functional Porous Coordination Polymers. *Angewandte Chemie International Edition*, 43(18):2334–2375, 2004.
- [3] Stuart L. James. Metal-Organic Frameworks. *Chem. Soc. Rev.*, 32:276–288, 2003.
- [4] Gerard Ferey. Hybrid Porous Solids: Past, Present, Future. *Chem. Soc. Rev.*, 37:191–214, 2008.
- [5] Adrien P. Cote, Annabelle I. Benin, Nathan W. Ockwig, Michael O’Keeffe, Adam J. Matzger, and Omar M. Yaghi. Porous, Crystalline, Covalent Organic Frameworks. *Science*, 310(5751):1166–1170, 2005.
- [6] Xiao Feng, Xuesong Ding, and Donglin Jiang. Covalent Organic Frameworks. *Chem. Soc. Rev.*, 41:6010–6022, 2012.
- [7] Hani M. El-Kaderi, Joseph R. Hunt, Jose L. Mendoza-Cortes, Adrien P. Cote, Robert E. Taylor, Michael O’Keeffe, and Omar M. Yaghi. Designed Synthesis of 3D Covalent Organic Frameworks. *Science*, 316(5822):268–272, 2007.
- [8] Kyo Sung Park, Zheng Ni, Adrien P. Cote, Jae Yong Choi, Rudan Huang, Fernando J. Uribe-Romo, Hee K. Chae, Michael O’Keeffe, and Omar M. Yaghi. Exceptional Chemical and Thermal Stability of Zeolitic Imidazolate Frameworks. *Proceedings of the National Academy of Sciences*, 103(27):10186–10191, 2006.
- [9] Nathaniel L. Rosi, Juergen Eckert, Mohamed Eddaoudi, David T. Vodak, Jaheon Kim, Michael O’Keeffe, and Omar M. Yaghi. Hydrogen Storage in Microporous Metal-Organic Frameworks. *Science*, 300(5622):1127–1129, 2003.
- [10] Kaneko Katsumi. Determination of Pore Size and Pore Size Distribution. *Journal of Membrane Science*, 96(1):59–89, 1994.
- [11] Kenji Sumida, David L. Rogow, Jarad A. Mason, Thomas M. McDonald, Eric D. Bloch, Zoey R. Herm, Tae-Hyun Bae, and Jeffrey R. Long. Carbon Dioxide Capture in MetalOrganic Frameworks. *Chemical Reviews*, 112(2):724–781, 2012.
- [12] Jian-Rong Li, Ryan J. Kuppler, and Hong-Cai Zhou. Selective Gas Adsorption and Separation in Metal-Organic Frameworks. *Chem. Soc. Rev.*, 38:1477–1504, 2009.

- [13] Hiroyasu Furukawa and Omar M. Yaghi. Storage of Hydrogen, Methane, and Carbon Dioxide in Highly Porous Covalent Organic Frameworks for Clean Energy Applications. *Journal of the American Chemical Society*, 131(25):8875–8883, 2009. PMID: 19496589.
- [14] Rahul Banerjee, Anh Phan, Bo Wang, Carolyn Knobler, Hiroyasu Furukawa, Michael O’Keeffe, and Omar M. Yaghi. High-throughput Synthesis of Zeolitic Imidazolate Frameworks and Application to CO₂ Capture. *Science*, 319(5865):939–943, 2008.
- [15] Thierry Loiseau, Christian Serre, Clarisse Huguenard, Gerhard Fink, Francis Taulelle, Marc Henry, Thierry Bataille, and Grard Frey. A Rationale for the Large Breathing of the Porous Aluminum Terephthalate (MIL-53) upon Hydration. *Chemistry A European Journal*, 10(6):1373–1382, 2004.
- [16] Christopher E. Wilmer, Michael Leaf, Chang Yeon Lee, Omar K. Farha, Brad G. Hauser, Joseph T. Hupp, and Randall Q. Snurr. Large-Scale Screening of Hypothetical Metal-Organic Frameworks. *Nature Chemistry*, 4(2):83–89, 2012.
- [17] Allison N. Dickey, A. Ozgur Yazaydin, Richard R. Willis, and Randall Q. Snurr. Screening CO₂/N₂ Selectivity in Metal-Organic Frameworks using Monte Carlo Simulations and Ideal Adsorbed Solution Theory. *The Canadian Journal of Chemical Engineering*, 90(4):825–832, 2012.
- [18] Yongchul G. Chung, Jeffrey Camp, Maciej Haranczyk, Benjamin J. Sikora, Wojciech Bury, Vaiva Krungleviciute, Taner Yildirim, Omar K. Farha, David S. Sholl, and Randall Q. Snurr. Computation-Ready, Experimental MetalOrganic Frameworks: A Tool To Enable High-Throughput Screening of Nanoporous Crystals. *Chemistry of Materials*, 26(21):6185–6192, 2014.
- [19] A. K. Rappe, C. J. Casewit, K. S. Colwell, W. A. Goddard, and W. M. Skiff. UFF, a Full Periodic Table Force Field for Molecular Mechanics and Molecular Dynamics Simulations. *Journal of the American Chemical Society*, 114(25):10024–10035, 1992.
- [20] Stephen L. Mayo, Barry D. Olafson, and William A. Goddard. DREIDING: a Generic Force Field for Molecular Simulations. *The Journal of Physical Chemistry*, 94(26):8897–8909, 1990.
- [21] Chris Oostenbrink, Alessandra Villa, Alan E. Mark, and Wilfred F. Van Gunsteren. A Biomolecular Force Field Based on the Free Enthalpy of Hydration and Solvation: The GROMOS Force Field Parameter Sets 53A5 and 53A6. *Journal of Computational Chemistry*, 25(13):1656–1676, 2004.
- [22] William L. Jorgensen, David S. Maxwell, and Julian Tirado-Rives. Development and Testing of the OPLS All-Atom Force Field on Conformational Energetics and Properties of Organic Liquids. *Journal of the American Chemical Society*, 118(45):11225–11236, 1996.
- [23] Wendy D. Cornell, Piotr Cieplak, Christopher I. Bayly, Ian R. Gould, Kenneth M. Merz, David M. Ferguson, David C. Spellmeyer, Thomas Fox, James W. Caldwell, and Peter A. Kollman. A Second Generation Force Field for the Simulation of Proteins, Nucleic Acids,

- and Organic Molecules. *Journal of the American Chemical Society*, 117(19):5179–5197, 1995.
- [24] Junmei Wang, Romain M. Wolf, James W. Caldwell, Peter A. Kollman, and David A. Case. Development and Testing of a General Amber Force Field. *Journal of Computational Chemistry*, 25(9):1157–1174, 2004.
- [25] Marcus G. Martin and J. Ilja Siepmann. Transferable Potentials for Phase Equilibria. 1. United-Atom Description of n-Alkanes. *The Journal of Physical Chemistry B*, 102(14):2569–2577, 1998.
- [26] Helder M. Marques, Orde Q. Munro, Neil E. Grimmer, Demitrius C. Levendis, Fabrizio Marsicano, Gary Pattrick, and Theona Markoulides. A Force Field for Molecular Mechanics Studies of Iron Porphyrins. *J. Chem. Soc., Faraday Trans.*, 91:1741–1749, 1995.
- [27] Xiao Yuan. Li, Roman S. Czernuszewicz, James R. Kincaid, Y. Oliver. Su, and Thomas G. Spiro. Consistent Porphyrin Force Field. 1. Normal-Mode Analysis for Nickel Porphine and Nickel Tetraphenylporphine from Resonance Raman and Infrared Spectra and Isotope Shifts. *The Journal of Physical Chemistry*, 94(1):31–47, 1990.
- [28] Matthew A. Addicoat, Nina Vankova, Ismot Farjana Akter, and Thomas Heine. Extension of the Universal Force Field to MetalOrganic Frameworks. *Journal of Chemical Theory and Computation*, 10(2):880–891, 2014.
- [29] Sareeya Bureekaew, Saeed Amirjalayer, Maxim Tafipolsky, Christian Spickermann, Tapta Kanchan Roy, and Rochus Schmid. MOF-FF - A Flexible First-Principles Derived Force Field for Metal-Organic Frameworks. *Physica Status Solidi*, 250(6):1128–1141, 2013.
- [30] Norman L. Allinger, Young H. Yuh, and Jenn Huei Lii. Molecular Mechanics. The MM3 Force Field for Hydrocarbons. 1. *Journal of the American Chemical Society*, 111(23):8551–8566, 1989.
- [31] Louis Vanduyfhuys, Steven Vandenbrande, Toon Verstraelen, Rochus Schmid, Michel Waroquier, and Veronique Van Speybroeck. QuickFF: A Program for a Quick and Easy Derivation of Force Fields for Metal-Organic Frameworks from Ab Initio Input. *Journal of Computational Chemistry*, 36(13):1015–1027, May 2015.
- [32] L. Vanduyfhuys, T. Verstraelen, M. Vandichel, M. Waroquier, and V. Van Speybroeck. Ab Initio Parametrized Force Field for the Flexible MetalOrganic Framework MIL-53(Al). *Journal of Chemical Theory and Computation*, 8(9):3217–3231, 2012.
- [33] Maxim Tafipolsky, Saeed Amirjalayer, and Rochus Schmid. Ab Initio Parametrized MM3 Force Field for the Metal-Organic Framework mof-5. *Journal of Computational Chemistry*, 28(7):1169–1176, 2007.
- [34] E. Garcia-Perez, J. B. Parra, C. O. Ania, A. Garcia-Sanchez, J. M. van Baten, R. Krishna, D. Dubbeldam, and S. Calero. A Computational Study of CO₂, N₂, and CH₄ Adsorption in Zeolites. *Adsorption*, 13(5):469–476, 2007.

- [35] Almudena Garcia-Sanchez, Conchi O. Ania, Jose B. Parra, David Dubbeldam, Thijs J. H. Vlugt, Rajamani Krishna, and Sofia Calero. Transferable Force Field for Carbon Dioxide Adsorption in Zeolites. *The Journal of Physical Chemistry C*, 113(20):8814–8820, 2009.
- [36] G. Maurin, P. L. Llewellyn, and R. G. Bell. Adsorption Mechanism of Carbon Dioxide in Faujasites: Grand Canonical Monte Carlo Simulations and Microcalorimetry Measurements. *The Journal of Physical Chemistry B*, 109(33):16084–16091, 2005.
- [37] Hanjun Fang, Preeti Kamakoti, Ji Zang, Stephen Cundy, Charanjit Paur, Peter I. Ravikovich, and David S. Sholl. Prediction of CO₂ Adsorption Properties in Zeolites Using Force Fields Derived from Periodic Dispersion-Corrected DFT Calculations. *The Journal of Physical Chemistry C*, 116(19):10692–10701, 2012.
- [38] Michael Fischer and Robert G. Bell. Influence of Zeolite Topology on CO₂/N₂ Separation Behavior: Force Field Simulations Using a DFT Derived Charge Model. *The Journal of Physical Chemistry C*, 116(50):26449–26463, 2012.
- [39] Nohad Gresh, G. Andrs Cisneros, Thomas A. Darden, and Jean-Philip Piquemal. Anisotropic, Polarizable Molecular Mechanics Studies of Inter- and Intramolecular Interactions and Ligand-Macromolecule Complexes. A Bottom-Up Strategy. *Journal of Chemical Theory and Computation*, 3(6):1960–1986, 2007.
- [40] Mark S. Gordon, Mark A. Freitag, Pradipta Bandyopadhyay, Jan H. Jensen, Visvaldas Kairys, and Walter J. Stevens. The Effective Fragment Potential Method: A QM-Based MM Approach to Modeling Environmental Effects in Chemistry. *The Journal of Physical Chemistry A*, 105(2):293–307, 2001.
- [41] J. R. Schmidt, Kuang Yu, and Jesse G. McDaniel. Transferable Next-Generation Force Fields from Simple Liquids to Complex Materials. *Accounts of Chemical Research*, 48(3):548–556, 2015.
- [42] Bogumil Jeziorski, Robert Moszynski, and Krzysztof Szalewicz. Perturbation Theory Approach to Intermolecular Potential Energy Surfaces of van der Waals Complexes. *Chemical Reviews*, 94(7):1887–1930, November 1994.
- [43] Anthony Stone. *The Theory of Intermolecular Forces*. Oxford University Press, Oxford, 2013. DOI: 10.1093/acprof:oso/9780199672394.001.0001.
- [44] Mark K. Transtrum, Kevin S. Brown, Bryan C. Daniels, Christopher R. Myers, and James P. Sethna. Perspective: Sloppiness and Emergent Theories in Physics, Biology, and Beyond. *The Journal of Chemical Physics*, 143(1), July 2015.
- [45] A.J. Stone and A.J. Misquitta. Atom-Atom Potentials from Ab Initio Calculations. *International Reviews in Physical Chemistry*, 26(1):193–222, 2007.
- [46] Ad van der Avoird, Paul E. S. Wormer, and Robert Moszynski. From Intermolecular Potentials to the Spectra of van der Waals Molecules, and Vice Versa. *Chemical Reviews*, 94(7):1931–1974, 1994.

- [47] Jan Hermann, Dario Alfe, and Alexandre Tkatchenko. Nanoscale π - π Stacked Molecules are bound by Collective Charge Fluctuations. *Nature Communications*, 8, 2017.
- [48] Stefan Grimme. A General Quantum Mechanically Derived Force Field (QMDFF) for Molecules and Condensed Phase Simulations. *Journal of Chemical Theory and Computation*, 10(10):4497–4514, 2014.
- [49] Steven Vandenbrande, Michel Waroquier, Veronique Van Speybroeck, and Toon Verstraeten. The Monomer Electron Density Force Field (MEDFF): A Physically Inspired Model for Non-Covalent Interactions. *Journal of Chemical Theory and Computation (JCTC)*, 13(1):161–179, 2017.
- [50] Prashant Mishra, Hari Prasad Uppara, Bishnupada Mandal, and Sasidhar Gumma. Adsorption and Separation of Carbon Dioxide using MIL-53(Al) Metal-Organic Framework. *Industrial & Engineering Chemistry Research*, 53(51):19747–19753, 2014.
- [51] Thierry Loiseau, Christian Serre, Clarisse Huguenard, Gerhard Fink, Francis Taulelle, Marc Henry, Thierry Bataille, and Gerard Ferey. A Rationale for the Large Breathing of the Porous Aluminum Terephthalate (MIL-53) Upon Hydration. *Chemistry - A European Journal*, 10(6):1373–1382, 2004.
- [52] Kenji Sumida, David L. Rogow, Jarad A. Mason, Thomas M. McDonald, Eric D. Bloch, Zoey R. Herm, Tae-Hyun Bae, and Jeffrey R. Long. Carbon Dioxide Capture in Metal-Organic Frameworks. *Chemical Reviews*, 112(2):724–781, 2012.
- [53] Yun Liu, Jae-Hyuk Her, Anne Dailly, Anibal J. Ramirez-Cuesta, Dan A. Neumann, and Craig M. Brown. Reversible Structural Transition in MIL-53 with Large Temperature Hysteresis. *Journal of the American Chemical Society*, 130(35):11813–11818, 2008.
- [54] Pascal G. Yot, Zoubeyr Boudene, Jasmine Macia, Dominique Granier, Louis Vanduyfhuys, Toon Verstraeten, Veronique Van Speybroeck, Thomas Devic, Christian Serre, Gerard Ferey, Norbert Stock, and Guillaume Maurin. Metal-Organic Frameworks as Potential Shock Absorbers: the Case of the Highly Flexible MIL-53(al). *Chem. Commun.*, 50:9462–9464, 2014.
- [55] Aurelie U. Ortiz, Anne Boutin, Alain H. Fuchs, and Francois-Xavier Coudert. Anisotropic Elastic Properties of Flexible Metal-Organic Frameworks: How Soft are Soft Porous Crystals? *Phys. Rev. Lett.*, 109:195502, 2012.
- [56] Isabelle Beurroies, Mohammed Boulhout, Philip L. Llewellyn, Bogdan Kuchta, Gerard Ferey, Christian Serre, and Renaud Denoyel. Using Pressure to Provoke the Structural Transition of Metal-Organic Frameworks. *Angewandte Chemie International Edition*, 49(41):7526–7529, 2010.
- [57] Sandrine Bourrelly, Philip L. Llewellyn, Christian Serre, Franck Millange, Thierry Loiseau, and Gerard Ferey. Different Adsorption Behaviors of Methane and Carbon Dioxide in the Isotypic Nanoporous Metal Terephthalates MIL-53 and MIL-47. *Journal of the American Chemical Society*, 127(39):13519–13521, 2005.

- [58] K. Sing. Reporting Physisorption Data for Gas/Solid Systems with Special Reference to the Determination of Surface Area and Porosity. *Pure and Applied Chemistry*, 57(4):603–619, 1984.
- [59] D. Fairen-Jimenez, S. A. Moggach, M. T. Wharmby, P. A. Wright, S. Parsons, and T. Duren. Opening the Gate: Framework Flexibility in ZIF-8 Explored by Experiments and Simulations. *Journal of the American Chemical Society*, 133(23):8900–8902, 2011.
- [60] Zhijuan Zhang, Shikai Xian, Qibin Xia, Haihui Wang, Zhong Li, and Jing Li. Enhancement of CO₂ Adsorption and CO₂/N₂ Selectivity on ZIF-8 via Postsynthetic Modification. *American Institute of Chemical Engineers Journal*, 59(6):2195–2206, June 2013.
- [61] Stephen A. Moggach, Thomas D. Bennett, and Anthony K. Cheetham. The Effect of Pressure on ZIF-8: Increasing Pore Size with Pressure and the Formation of a High-Pressure Phase at 1.47 GPa. *Angewandte Chemie International Edition*, 48(38):7087–7089, 2009.
- [62] Shunsuke Tanaka, Kosuke Fujita, Yoshikazu Miyake, Manabu Miyamoto, Yasuhisa Hasegawa, Takashi Makino, Stijn Van der Perre, Julien Cousin Saint Remi, Tom Van Assche, Gino V. Baron, and Joeri F. M. Denayer. Adsorption and Diffusion Phenomena in Crystal Size Engineered ZIF-8 MOF. *The Journal of Physical Chemistry C*, 119(51):28430–28439, 2015.
- [63] Toon Verstraelen, Steven Vandenbrande, Farnaz Heidar-Zadeh, Louis Vanduyfhuys, Veronique Van Speybroeck, Michel Waroquier, and Paul W. Ayers. Minimal Basis Iterative Stockholder: Atoms in Molecules for Force-Field Development. *Journal of Chemical Theory and Computation*, 12:3894–3912, August 2016.
- [64] Yung Sik Kim, Seong Keun Kim, and Won Don Lee. Dependence of the Closed-shell Repulsive Interaction on the Overlap of the Electron Densities. *Chemical Physics Letters*, 80(3):574–575, June 1981.
- [65] K. T. Tang and J. Peter Toennies. An Improved Simple Model for the van der Waals Potential based on Universal Damping Functions for the Dispersion Coefficients. *The Journal of Chemical Physics*, 80(8):3726–3741, April 1984.
- [66] Alexandre Tkatchenko and Matthias Scheffler. Accurate Molecular Van Der Waals Interactions from Ground-State Electron Density and Free-Atom Reference Data. *Physical Review Letters*, 102(7):073005, February 2009.
- [67] George Starkschall and Roy G. Gordon. Calculation of Coefficients in the Power Series Expansion of the Long-Range Dispersion Force between Atoms. *The Journal of Chemical Physics*, 56(6):2801–2806, March 1972.
- [68] Jiri Cizek. On the Correlation Problem in Atomic and Molecular Systems. Calculation of Wavefunction Components in Ursell-Type Expansion Using Quantum-Field Theoretical Methods. *The Journal of Chemical Physics*, 45(11):4256–4266, 1966.

- [69] Axel D. Becke. Density-Functional Thermochemistry. III. The Role of Exact Exchange. *The Journal of Chemical Physics*, 98(7):5648–5652, 1993.
- [70] Chengteh Lee, Weitao Yang, and Robert G. Parr. Development of the Colle-Salvetti Correlation-Energy Formula into a Functional of the Electron Density. *Phys. Rev. B*, 37(2):785–789, 1988.
- [71] Rick A. Kendall, Thom H. Dunning Jr., and Robert J. Harrison. Electron Affinities of the First-Row Atoms Revisited. Systematic Basis Sets and Wave Functions. *The Journal of Chemical Physics*, 96(9):6796–6806, 1992.
- [72] M. Frisch, G. Trucks, H. Schlegel, M. Scuseria, G. and Robb, J. Cheeseman, G. Scalmani, V. Barone, B. Mennucci, G. Petersson, H. Nakatsuji, M. Caricato, X. Li, H. Hratchian, A. Izmaylov, J. Bloino, G. Zheng, J. Sonnenberg, M. Hada, M. Ehara, K. Toyota, R. Fukuda, J. Hasegawa, M. Ishida, T. Nakajima, Y. Honda, O. Kitao, H. Nakai, T. Vreven, J. Montgomery, J. Peralta, F. Ogliaro, M. Bearpark, J. Heyd, E. Brothers, K. Kudin, R. Staroverov, V. and Kobayashi, J. Normand, K. Raghavachari, A. Rendell, J. Burant, S. Iyengar, J. Tomasi, M. Cossi, N. Rega, J. Millam, M. Klene, J. Knox, J. Cross, V. Bakken, C. Adamo, J. Jaramillo, R. Gomperts, R. Stratmann, O. Yazyev, A. Austin, R. Cammi, C. Pomelli, J. Ochterski, R. Martin, K. Morokuma, V. Zakrzewski, G. Voth, P. Salvador, J. Dannenberg, S. Dapprich, A. Daniels, O. Farkas, J. Foresman, J. Ortiz, J. Cioslowski, and D. Fox. Gaussian 09, revision a.02. *Chemistry of Materials*.
- [73] Toon Verstraelen, Paweł Tecmer, Farnaz Heidar-Zadeh, Katharina Boguslawski, Matthew Chan, Yilin Zhao, Taewon D. Kim, Steven Vandenbrande, Derrick Yang, Cristina E. Gonzalez-Espinoza, Stijn Fias, Peter A. Limacher, Diego Berrocal, Ali Malek, and Paul W. Ayers. Horton 2.0.1, 2015.
- [74] K.P. Huber and G. Herzberg. *Molecular Spectra and Molecular Structure: IV. Constants Of Diatomic Molecules*. Number 4 in Molecular Spectra and Molecular Structure. Van Nostrand, Toronto, 1966.
- [75] Justin M. Turney, Andrew C. Simmonett, Robert M. Parrish, Edward G. Hohenstein, Francesco A. Evangelista, Justin T. Fermann, Benjamin J. Mintz, Lori A. Burns, Jeremiah J. Wilke, Micah L. Abrams, Nicholas J. Russ, Matthew L. Leininger, Curtis L. Janssen, Edward T. Seidl, Wesley D. Allen, Henry F. Schaefer, Rollin A. King, Edward F. Valeev, C. David Sherrill, and T. Daniel Crawford. Psi4: An Open-Source Ab Initio Electronic Structure Program. *Wiley Interdisciplinary Reviews: Computational Molecular Science*, 2(4):556–565, 2012.
- [76] Jan Rezac, Kevin E. Riley, and Pavel Hobza. S66: A Well-Balanced Database of Benchmark Interaction Energies Relevant to Biomolecular Structures. *Journal of Chemical Theory and Computation*, 7(8):2427–2438, 2011.
- [77] Mohamad H. Karimi Jafari, Ali Maghari, and Shant Shahbazian. An Improved Ab Initio Potential Energy Surface for N₂-N₂. *Chemical Physics*, 314:249–262, 2005.

- [78] Leonardo Pacifici, Marco Verdicchio, and Antonio Lagana. Multi Reference versus Coupled Cluster ab Initio Calculations for the N₂+N₂ Reaction Channels. In *Computational Science and Its Applications*, pages 31–46. Springer Berlin Heidelberg, Berlin, Heidelberg, 2013. DOI: 10.1007/978-3-642-39637-3_3.
- [79] Pavel Hobza. Calculations on Noncovalent Interactions and Databases of Benchmark Interaction Energies. *Accounts of Chemical Research*, 45(4):663–672, April 2012.
- [80] D. McQuarrie. *Statistical Mechanics*. University Science Books, 2000.
- [81] P. Nowak, R. Kleinrahm, and W. Wagner. Measurement and Correlation of the (p,ρ,T) Relation of Nitrogen. I. The Homogeneous Gas and Liquid Regions in the Temperature Range from 66 K to 340 K at Pressures up to 12 MPa. *The Journal of Chemical Thermodynamics*, 29(10):1137–1156, 1997.
- [82] David Dubbeldam, Sofa Calero, Donald E. Ellis, and Randall Q. Snurr. RASPA: Molecular Simulation Software for Adsorption and Diffusion in Flexible Nanoporous Materials. *Molecular Simulation*, 42(2):81–101, 2015.
- [83] T.R. Stobridge. The Thermodynamic Properties of Nitrogen from 64 K to 300 K between 0.1 and 200 Atmospheres. Technical report, National Institute of Standards and Technology, Colorado, January 1962.
- [84] G. Herzberg. *Molecular Spectra and Molecular Structure: III. Electronic Spectra and Electronic Structure of Polyatomic Molecules*. Number 3 in Molecular Spectra and Molecular Structure. Van Nostrand, Toronto, 1966.
- [85] Yulia N. Kalugina, Yosra Ajili, Andrei A. Vigasin, Nejm Eddine Jaidane, and Majdi Hochlaf. Explicit Correlation Treatment of the Potential Energy Surface of CO₂ Dimer. *The Journal of Chemical Physics*, 140(23):234310, June 2014.
- [86] Rebecca Hadad and Roi Baer. Minimally-corrected Partial Atomic Charges for Non-Covalent Electrostatic Interactions. *Molecular Physics*, December 2016.
- [87] Hossein Eslami, Farkhondeh Mozaffari, and Ali Boushehri. Calculation of the Second Virial Coefficient of Nonspherical Molecules: Revisited. *International Journal of Thermal Sciences*, 40(11):999–1010, 2001.
- [88] Roland Span and Wolfgang Wagner. A New Equation of State for Carbon Dioxide Covering the Fluid Region from the TriplePoint Temperature to 1100 K at Pressures up to 800 MPa. *Journal of Physical and Chemical Reference Data*, 25(6):1509–1596, 1996.
- [89] P. E. Blöchl. Projector-Augmented-Wave Method. *Phys. Rev. B*, 50(24):17953–17979, 1994.
- [90] J. Enkovaara, C. Rostgaard, J. J. Mortensen, J. Chen, M. Dulak, L. Ferrighi, J. Gavnholt, C. Glinsvad, V. Haikola, H. A. Hansen, H. H. Kristoffersen, M. Kuusima, A. H. Larsen,

- L. Lehtovaara, M. Ljungberg, O. Lopez-Acevedo, P. G. Moses, J. Ojanen, T. Olsen, V. Petzold, N. A. Romero, J. Stausholm-Moller, M. Strange, G. A. Tritsaris, M. Vanin, M. Walter, B. Hammer, H. Hakkinen, G. K. H. Madsen, R. M. Nieminen, J. K. Norskov, M. Puska, T. T. Rantala, J. Schiotz, K. S. Thygesen, and K. W. Jacobsen. Electronic Structure Calculations with GPAW: a Real-Space Implementation of the Projector-Augmented-Wave Method. *Journal of Physics: Condensed Matter*, 22(25):253202, 2010.
- [91] John P. Perdew, Kieron Burke, and Matthias Ernzerhof. Generalized Gradient Approximation Made Simple. *Phys. Rev. Lett.*, 77(18):3865–3868, 1996.
- [92] John P. Perdew, Kieron Burke, and Matthias Ernzerhof. Generalized Gradient Approximation Made Simple. *Phys. Rev. Lett.*, 78(7):1396–1396, 1997.
- [93] Stefan Grimme, Jens Antony, Stephan Ehrlich, and Helge Krieg. A Consistent and Accurate Ab Initio Parametrization of Density Functional Dispersion Correction (DFT-D) for the 94 Elements H-Pu. *The Journal of Chemical Physics*, 132(15):154104, 2010.
- [94] Stefan Grimme, Stephan Ehrlich, and Lars Goerigk. Effect of the Damping Function in Dispersion Corrected Density Functional Theory. *Journal of Computational Chemistry*, 32(7):1456–1465, 2011.
- [95] G. Kresse and J. Furthmuller. Efficiency of Ab Initio Total Energy Calculations for Metals and semiconductors using a Plane-Wave Basis Set. *Computational Materials Science*, 6(1):15–50, 1996.
- [96] Alexandre Tkatchenko, Robert A. DiStasio, Roberto Car, and Matthias Scheffler. Accurate and Efficient Method for Many-Body van der Waals Interactions. *Phys. Rev. Lett.*, 108(23):236402–236406, 2012.
- [97] Alberto Ambrosetti, Anthony M. Reilly, Robert A. DiStasio Jr., and Alexandre Tkatchenko. Long-Range Correlation Energy Calculated from Coupled Atomic Response Functions. *The Journal of Chemical Physics*, 140(18):18A508, 2014.
- [98] Robert A DiStasio Jr, Vivekanand V Gobre, and Alexandre Tkatchenko. Many-Body van der Waals Interactions in Molecules and Condensed Matter. *Journal of Physics: Condensed Matter*, 26(21):213202, 2014.
- [99] Patrick Bultinck, Christian Van Alsenoy, Paul W. Ayers, and Ramon Carbo-Dorca. Critical Analysis and Extension of the Hirshfeld Atoms in Molecules. *The Journal of Chemical Physics*, 126(14):144111, 2007.
- [100] Mihail Mihaylov, Kristina Chakarova, Stanislava Andonova, Nikola Drenchev, Elena Ivanova, Anahid Sabetghadam, Beatriz Seoane, Jorge Gascon, Freek Kapteijn, and Konstantin Hadjiivanov. Adsorption Forms of CO₂ on MIL-53(Al) and NH₂-MIL-53(Al) As Revealed by FTIR Spectroscopy. *The Journal of Physical Chemistry C*, 120(41):23584–23595, 2016.
- [101] Ding-Yu Peng and Donald B. Robinson. A New Two-Constant Equation of State. *Industrial & Engineering Chemistry Fundamentals*, 15(1):59–64, 1976.

- [102] Joe McEwen, Jim-Dario Hayman, and A. Ozgur Yazaydin. A Comparative Study of CO₂, CH₄ and N₂ Adsorption in ZIF-8, Zeolite-13X and BPL Activated Carbon. *Chemical Physics*, 412:72–76, 2013.
- [103] E. Garcia-Perez, P. Serra-Crespo, S. Hamad, F. Kapteijn, and J. Gascon. Molecular Simulation of Gas Adsorption and Diffusion in a Breathing MOF Using a Rigid Force Field. *Phys. Chem. Chem. Phys.*, 16(30):16060–16066, 2014.